

# Entry, Descent and Landing Systems Analysis Study: Phase 1 Report

*Alicia M. Dwyer Cianciolo, Jody L. Davis, David R. Komar, Michelle M. Munk, Jamshid A. Samareh,  
Julie A. Williams-Byrd, and Thomas A. Zang  
NASA Langley Research Center, Hampton, Virginia*

*Richard W. Powell and Jeremy D. Shidner  
Analytical Mechanics Associates, Inc., Hampton, Virginia*

*Douglas O. Stanley and Alan W. Wilhite  
Georgia Institute of Technology, Atlanta, Georgia*

*David J. Kinney and M. Kathleen McGuire  
NASA Ames Research Center, Moffett Field, California*

*James O. Arnold  
University of California, Santa Cruz, California*

*Austin R. Howard  
ELORET Corporation, Sunnyvale, California*

*Ronald R. Sostaric, Joseph W. Studak, and Carlie H. Zumwalt  
NASA Johnson Space Center, Houston, Texas*

*Eduardo G. Llama  
GBTech, Inc., Houston, Texas*

*Jordi Casoliva, Mark C. Ivanov, Ian Clark, and Anita Sengupta  
NASA Jet Propulsion Laboratory, Pasadena, California*

## NASA STI Program . . . in Profile

Since its founding, NASA has been dedicated to the advancement of aeronautics and space science. The NASA scientific and technical information (STI) program plays a key part in helping NASA maintain this important role.

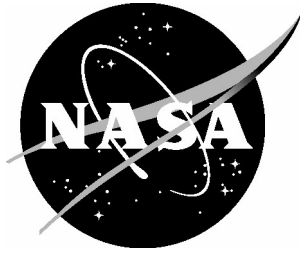
The NASA STI program operates under the auspices of the Agency Chief Information Officer. It collects, organizes, provides for archiving, and disseminates NASA's STI. The NASA STI program provides access to the NASA Aeronautics and Space Database and its public interface, the NASA Technical Report Server, thus providing one of the largest collections of aeronautical and space science STI in the world. Results are published in both non-NASA channels and by NASA in the NASA STI Report Series, which includes the following report types:

- **TECHNICAL PUBLICATION.** Reports of completed research or a major significant phase of research that present the results of NASA programs and include extensive data or theoretical analysis. Includes compilations of significant scientific and technical data and information deemed to be of continuing reference value. NASA counterpart of peer-reviewed formal professional papers, but having less stringent limitations on manuscript length and extent of graphic presentations.
- **TECHNICAL MEMORANDUM.** Scientific and technical findings that are preliminary or of specialized interest, e.g., quick release reports, working papers, and bibliographies that contain minimal annotation. Does not contain extensive analysis.
- **CONTRACTOR REPORT.** Scientific and technical findings by NASA-sponsored contractors and grantees.
- **CONFERENCE PUBLICATION.** Collected papers from scientific and technical conferences, symposia, seminars, or other meetings sponsored or co-sponsored by NASA.
- **SPECIAL PUBLICATION.** Scientific, technical, or historical information from NASA programs, projects, and missions, often concerned with subjects having substantial public interest.
- **TECHNICAL TRANSLATION.** English-language translations of foreign scientific and technical material pertinent to NASA's mission.

Specialized services also include creating custom thesauri, building customized databases, and organizing and publishing research results.

For more information about the NASA STI program, see the following:

- Access the NASA STI program home page at <http://www.sti.nasa.gov>
- E-mail your question via the Internet to [help@sti.nasa.gov](mailto:help@sti.nasa.gov)
- Fax your question to the NASA STI Help Desk at 443-757-5803
- Phone the NASA STI Help Desk at 443-757-5802
- Write to:  
NASA STI Help Desk  
NASA Center for AeroSpace Information  
7115 Standard Drive  
Hanover, MD 21076-1320



# Entry, Descent and Landing Systems Analysis Study: Phase 1 Report

*Alicia M. Dwyer Cianciolo, Jody L. Davis, David R. Komar, Michelle M. Munk, Jamshid A. Samareh,  
Julie A. Williams-Byrd, and Thomas A. Zang  
NASA Langley Research Center, Hampton, Virginia*

*Richard W. Powell and Jeremy D. Shidner  
Analytical Mechanics Associates, Inc., Hampton, Virginia*

*Douglas O. Stanley and Alan W. Wilhite  
Georgia Institute of Technology, Atlanta, Georgia*

*David J. Kinney and M. Kathleen McGuire  
NASA Ames Research Center, Moffett Field, California*

*James O. Arnold  
University of California, Santa Cruz, California*

*Austin R. Howard  
ELORET Corporation, Sunnyvale, California*

*Ronald R. Sostaric, Joseph W. Studak, and Carlie H. Zumwalt  
NASA Johnson Space Center, Houston, Texas*

*Eduardo G. Llama  
GBTech, Inc., Houston, Texas*

*Jordi Casoliva, Mark C. Ivanov, Ian Clark, and Anita Sengupta  
NASA Jet Propulsion Laboratory, Pasadena, California*

National Aeronautics and  
Space Administration

Langley Research Center  
Hampton, Virginia 23681-2199

Trade names and trademarks are used in this report for identification only. Their usage does not constitute an official endorsement, either expressed or implied, by the National Aeronautics and Space Administration.

Available from:

NASA Center for AeroSpace Information  
7115 Standard Drive  
Hanover, MD 21076-1320  
443-757-5802

# Table of Contents

Table of Contents .....	i
List of Figures .....	iii
List of Tables.....	v
Acronyms .....	vi
Acknowledgements .....	xi
EDL-SA Team.....	xii
Abstract .....	xiii
1 Background.....	1
2 Exploration Class Architectures and Technologies.....	3
3 Exploration Class Component Model.....	5
3.1 Mass Models .....	5
3.1.1 Rigid Mid-L/D Aeroshell .....	5
3.1.2 Hypersonic Inflatable Aerodynamic Decelerator (HIAD) .....	7
3.1.3 Supersonic Inflatable Aerodynamic Decelerator (SIAD).....	9
3.1.4 Supersonic/Subsonic Retro-Propulsion (SRP) .....	9
3.2 Aerodynamic and Aerothermal Modeling.....	13
3.2.1 Tool Set.....	13
3.2.2 Mid-L/D Geometry.....	14
3.2.3 Flexible Low-L/D Vehicle (HIAD).....	15
3.3 Aerocapture/EDL Guidance Algorithms.....	16
3.3.1 HYPAS (Hybrid Predictor-Corrector Aerocapture Scheme) .....	16
3.3.2 Numerical Predictor Corrector Guidance (NPC).....	18
3.3.3 Theoretical EDL Guidance.....	19
3.3.4 Analytic Predictor-Corrector – Apollo-Derived Guidance .....	19
3.3.5 Guidance Comparison .....	22
3.4 Retro-propulsion.....	24
3.5 Thermal Protection Systems.....	27
3.5.1 HIAD – 23 m diameter .....	27
3.5.2 Mid L/D Aeroshell.....	28
4 Simulation Results .....	32
4.1 Aerocapture Simulation Results.....	32
4.1.1 Aerocapture Flight Path Corridor Sizing .....	33
4.1.2 Nominal Trajectory Results .....	34
4.1.3 Monte Carlo Results .....	36
4.1.4 Sensitivity Study Results .....	37
4.1.5 Trades .....	38
4.2 Entry, Descent and Landing.....	41
4.2.1 Comparison of EDL-SA to DRA5.....	41
4.2.2 EDL Strategy .....	42
4.2.3 Nominal and Monte Carlo Results .....	44
4.2.4 Sensitivities Study Results.....	52
5 Packaging.....	55
5.1 Preliminary Packaging .....	55
5.2 HIAD Packaging .....	55
6 Figures of Merit .....	58
6.1 Assessment Process.....	58
6.2 Figure of Merit Weighting .....	61
6.3 Assessment Results .....	61

6.3.1	Architecture Assessment Results.....	61
6.3.2	Technology Assessment Results .....	63
6.4	Summary .....	64
7	Viability Assessments.....	65
7.1	Dual-Layer TPS.....	65
7.2	IAD Controllability .....	68
8	Technology Investment Recommendations .....	69
9	Exploration-Class Study Open Issues.....	70
10	Large Robotic-Class Study .....	71
10.1	Packaging Feasibility.....	71
10.2	Parachutes .....	71
10.2.1	Modeling Overview .....	72
10.2.2	Deployment Modeling .....	72
10.2.3	Parachute Drag Performance .....	74
10.3	Monte Carlo Simulation Results.....	77
10.4	Robotic Class Summary.....	79
11	Bibliography.....	80
A	Appendix A. DRMs, GR&As and FOMs.....	83
A.1	Design Reference Missions .....	83
A.1.1	Exploration-Class Design Reference Mission .....	83
A.1.2	Large-Robotic Class Reference Mission.....	85
A.2	EDL-SA Study Ground Rules and Assumptions.....	88
A.2.1	General Ground Rules and Assumptions .....	88
A.2.2	Exploration Mission Ground Rules and Assumptions .....	88
A.2.3	Robotic Mission Ground Rules and Assumptions .....	88
A.2.4	Margin Policy.....	89
A.2.5	Exploration Mission Monte Carlo Parameters .....	91
A.2.6	Robotic Mission Monte Carlo Parameters .....	94
A.3	EDL-SA Study Figures of Merit.....	95
A.3.1	Description of Figures of Merit .....	95
A.3.2	Categories for Figures of Merit.....	95
A.3.3	Definitions of Figures of Merit .....	96
A.3.4	Scoring for Figures of Merit .....	96
A.3.5	FOM Proxy Parameters.....	97
B	Appendix B: EDL Transition Events.....	100
B.1	Background .....	100
B.2	Methodology .....	100
B.3	Summary of Results .....	100
B.3.1	Rigid Aeroshell to SRP .....	101
B.3.2	Inflatable Aeroshell to SRP.....	102

## List of Figures

Figure 1. Study Flow .....	1
Figure 2. Exploration Class Architectures .....	4
Figure 3. EDL-SA Major Mass Components .....	5
Figure 4. Finite-Element Model of the Rigid Aeroshell .....	6
Figure 5. Structural (left) and TPS (right) Mass for the Rigid Aeroshell of Architecture 1 .....	7
Figure 6. Reinforcing Fibers Invalid source specified. ....	8
Figure 7. Structural (left) and TPS (right) Mass for the HIAD of Architecture 2 .....	8
Figure 8. SRP Specific Impulse vs. Engine Thrust-to-Weight .....	11
Figure 9. Mid L/D (left) and HIAD (right) Vehicle Configurations .....	13
Figure 10. Representative DPLR Solution .....	14
Figure 11. Representative CBAERO Solution .....	14
Figure 12. Representative CART3D Solution .....	14
Figure 13. Anchored CBAERO Solution (left) and Subsonic CART3D Solution (right) .....	16
Figure 14. Guidance comparison for Architecture 1 .....	23
Figure 15. Guidance comparison for Architecture 8 .....	23
Figure 16. SRP Sample Throttle Profile (left) and SRP ISP vs Expansion Ratio (right) .....	25
Figure 17. Notional Tank Arrangement .....	25
Figure 18. HIAD Material Stack .....	27
Figure 19. HIAD Dual Pulse Surface Heating History and Integrated Heatload Contour .....	28
Figure 20. Mid L/D Aeroshell TPS Stack .....	29
Figure 21. Mid L/D Aeroshell Material Splitlines .....	29
Figure 22. Mid L/D Aeroshell Dual Pulse Surface Heating History and Integrated Heatload Contour .....	30
Figure 23. Aerocapture Phases .....	33
Figure 24. Available Skip-out Margin for Variations of L/D and Ballistic Number .....	34
Figure 25. Altitude Profiles for All Configurations .....	35
Figure 26. Nominal Bank Profiles for the 23 m HIAD .....	35
Figure 27. Nominal Drag Acceleration and Attitude Rate Profile for 23 m HIAD .....	35
Figure 28. Monte Carlo Results for the Rigid Mid L/D Aeroshell .....	36
Figure 29. Monte Carlo Results for the 23 m HIAD, L/D = 0.3 .....	37
Figure 30. Monte Carlo Results for the 55 m HIAD, L/D = 0.2 .....	37
Figure 31. Delta V Sensitivity to Post-Aerocapture Orbit .....	38
Figure 32. Available Skip-out Margin for Low Combinations of L/D and Ballistic Number .....	39
Figure 33. Delta V Monte Carlo Results .....	39
Figure 34. Plot of 3 sigma peak heat rate versus diameter for lines of constant L/D .....	40
Figure 35. Effect of Flight Path Angle Dispersions for L/D=0.2, Bn=33.33 kg/m <sup>2</sup> .....	41
Figure 36. EDL-SA Exploration Class Altitude Versus Velocity .....	44
Figure 37. Architecture 1 Altitude vs. Time .....	45
Figure 38. Architecture 2 Altitude vs. Time .....	45
Figure 39. Rocket Plume Hypersonic Flowfield Interactions .....	46
Figure 40. Architecture 3 Arrival Mass and Delta V .....	47
Figure 41. Architecture 4 Altitude vs. Time .....	48
Figure 42. Architecture 6 Altitude vs. Time .....	49
Figure 43. Architecture 7 Altitude vs. Time .....	49
Figure 44. Architecture 8 Altitude vs. Time .....	50
Figure 45. Architecture 2 Packaging .....	55
Figure 46. First Attempt at HIAD TPS Packaging .....	56
Figure 47. Second Attempt at Packaging the 23 m “Apollo” HIAD .....	57
Figure 48. FOMs, Sub-FOMs and Sources Used to Evaluate .....	58

Figure 49. FOM Assessment Process.....	59
Figure 50. Programmatic Risk FOM Process Flow .....	60
Figure 51. Average FOM Category Weights .....	61
Figure 52. Architecture Score from FOM Weigth Surveys and Sensitivity Studies.....	62
Figure 53. Technology Score Ranges from FOM Weight Surveys and Sensitivity Study .....	63
Figure 54. (a) curved panel covered with ~5cm honeycomh filled with PICA blocks; (b) post tested stagnation iso-q model after exposure to 620 W/cm2 for 30 seconds; and (c) post tested swept cylinder model after exposure at 140 W/cm2 for 25 seconds.....	65
Figure 55. Iso-Q Model Design of PICA atop LI-900. Dimensions in inches.....	66
Figure 56. Test Thermal Cycle to Simulate Dual Heat Pulse .....	66
Figure 57. Post tested model at the IHF run condition.....	67
Figure 58. Post tested model at the IHF run condition.....	67
Figure 59. : Clips from a movie taken during the second heat pulse simulating entry from out-of-Mars orbit after aerocapture .....	68
Figure 60. Parachute systems considered. ....	72
Figure 61. High and Low Drag Performance Curves Used for DGB Modeling.....	74
Figure 62. Summary of supersonic Ringsail flight test drag data .....	76
Figure 63. Summary of supersonic Ringsail flight test data with high and low drag performance model .....	76
Figure 64. Monte Carlo simulation results using 8000 dispersed cases for the reefed parachute configuration. ....	78
Figure A-1. Exploration-Class Design Reference Missions .....	83
Figure A-2. Mars Transfer Vehicles .....	85
Figure A-3. Outer Mold Line of a Mars Lander Aeroshell .....	85
Figure A-4. Large Robotic-Class Design Reference Mission.....	86
Figure A-5. MSL and Large Robotic-Class Mission Landing Strategies .....	87
Figure B-1. Rigid Aeroshell to SRP Transition Option .....	101
Figure B-2. Baseline Rigid Aeroshell to SRP Transition Options.....	102
Figure B-3. Inflatable Aeroshell to SRP Transition Option.....	102
Figure B-4. Baseline Inflatable Decelerator to SRP Option .....	103
Figure B-5. Inflatable Hypersonic Aeroshell to Supersonic Inflatable Transition Options.....	104
Figure B-6. Baseline Hypersonic Inflatable Decelerator to Supersonic Inflatable Decelerator Option ...	105
Figure B-7. Rigid Aeroshell to Inflatable Aerodynamic Decelerator Options .....	105
Figure B-8. Baseline Rigid Aeroshell to Inflatable Aerodynamic Decelerator .....	106

## List of Tables

Table 1. Simplified Set of Exploration Class Technologies Considered by EDL-SA.....	4
Table 2. Nominal Parameters and Mass Breakdown for Architecture 1.....	7
Table 3. Nominal Parameters and Mass Breakdown for Architecture 2.....	9
Table 4. SRP Independent Variables and Limits for Response Surface Equations.....	10
Table 5. SRP Dependent Variables.....	10
Table 6. SRP Mass Breakdown for Architectures 1 and 3.....	12
Table 7. SRP Engine Characteristics.....	26
Table 8. TPS Sizing Margins.....	27
Table 9. Mid L/D Aeroshell TPS Mass Estimates (Not including attachment or WGA).....	30
Table 10. Mid L/D Aeroshell, Windward Side Estimated Masses with Attachment.....	31
Table 11. Aerocapture Monte Carlo Dispersion Values.....	36
Table 12. Architecture Component Separation Times.....	43
Table 13. EDL-SA Monte Carlo Dispersions.....	44
Table 14. Architecture 1 Results.....	45
Table 15. Architecture 2 Results.....	45
Table 16. Architecture 4 Results.....	48
Table 17. Architecture 6 Results.....	49
Table 18. Architecture 7 Results.....	49
Table 19. Architecture 8 Results.....	50
Table 20. Component Dimensions and Masses using Standard Margins.....	51
Table 21. Nominal Environment Conditions.....	52
Table 22. Environmental Sensitivity.....	53
Table 23. Performance Sensitivity.....	53
Table 24. Design Sensitivity.....	54
Table 25. Contributors to the FOM Assessment.....	59
Table 26. TDP Recommendations.....	69
Table 27. Summary of Supersonic Ringsail Parachute Inflation Times.....	73
Table 28. Summary of Supersonic Ringsail Test Conditions.....	75
Table 29. Supersonic Parachute Performance Results.....	77
Table 30. Supersonic Reefed Parachute Performance Results.....	78
Table 31. Comparison of MSL and the Scaled Reefed Ringsail Configuration.....	79
Table A-1. Key Parameters for the Exploration-Class DRM.....	84
Table A-2. Key Parameters fo the Large Robotic-Class DRM.....	87
Table A-3. EDL-SA Subsystem Margins.....	90
Table A-4. TRL Margin Increments.....	91
Table A-5. Mid-L/D Rigid Monte Carlo Parameters.....	91
Table A-6. Low-L/D Inflatable Monte Carlo Parameters.....	93
Table A-7. Robotic Monte Carlo Parameters.....	94
Table A-8. Definitions of Figures of Merit.....	96
Table A-9. Safety and Mission Success Proxy Parameters.....	97
Table A-10. Performance and Effectiveness Proxy Parameters.....	98
Table A-11. Programmatic Risk Proxy Parameters.....	98
Table A-12. Affordability and Life Cycle Cost Proxy Parameters.....	99
Table A-13. Applicability to Other Mission Proxy Parameters.....	99
Table B-1. EDL Failure Modes.....	106

## Acronyms

AIAA	American Institute for Aeronautics and Astronautics
ADP	Advanced Development Program
AFE	Aeroassist Flight Experiment
AHF	Aerodynamic Heating Facility
ALHAT	Autonomous Landing and Hazard Avoidance Technology
Al-Li	Aluminum Lithium
Alpha ( $\alpha$ )	Angle of Attack
APAS	Aerodynamic Preliminary Analysis System
APC	Analytic Predictor-Correction
ARA	Analytical Research Associates
ARC	Ames Research Center
ARMD	Aeronautics Research Mission Directorate
AS	Aeroshell
Beta ( $\beta$ )	Side Slip Angle
BC	Ballistic Coefficient
BLDT	Balloon Launched Decelerator Test
BN	Ballistic Number
CCRB	Customer Content Review Board
CBAERO	Engineering code to compute aero and aerothermodynamics
CECE	Common Extensible Cryogenic Engine
CEV	Crew Exploration Vehicle
CFD	Computational Fluid Dynamics
CG	Center of Gravity
CNES	Centre National d'Études Spatiales
CxP	Constellation Program
DGB	Disk Gap Band
deg	degrees
deg/sec <sup>2</sup>	degrees per second squared
DGB	Disk Gap Band
DOF	Degree of Freedom
DP	Dual Pulse
DPLR	Data Parallel Line Relaxation

DRA5	Design Reference Architecture 5.0
DRM	Design Reference Mission
DSIAD	Drag Supersonic Inflatable Aerodynamic Decelerator
EDL	Entry, Descent and Landing
EDL-SA	Entry, Descent and Landing Systems Analysis
EFPA	Entry Flight Path Angle
EPR	External Peer Review
ESAS	Exploration Systems Architecture Study
ESMD	Exploration Systems Mission Directorate
ETDP	Exploration Technology Development Program
EXAMINE	Exploration Architecture Model for the IN-space and Earth-to-orbit
FE	Finite Element
FIAT	Code to model TPS thermal response
FOM	Figure of Merit
FY	Fiscal Year
GRAM	Global Reference Atmosphere Model
GRC	Glenn Research Center
GR&A	Ground Rule and Assumption
H/C	Honeycomb
HIAD	Hypersonic Inflatable Aerodynamic Decelerator
HSRI	Human-Systems Integration Requirements
HT424	TPS adhesive used on Orion, Apollo, ARA H/C
HYPAS	Hybrid Predictor-Corrector Aerocapture Scheme
Hz	Hertz
IAD	Inflatable Aerodynamic Decelerator
IHF	Interactive Heating Facility
IMLEO	Initial Mass in Low Earth Orbit
in	inch
IRDT	Inflatable Reentry and Descent Technology
Iso-q	Constant Dynamic Pressure
Isp	Specific Impulse
ISRU	In-situ Resource Utilization
JANNAF	Joint Army, Navy, NASA Airforce
JPL	Jet Propulsion Laboratory

JSC	Johnson Space Center
kg	kilograms
kg/m <sup>2</sup>	kilograms per square meter
klbf	kilopounds of force
km	kilometers
kN	kilo Newtons
LaRC	Langley Research Center
lbf	pounds of force
LADAR	Laser Radar
LAURA	Langley Aerothermodynamic Upwind Relaxation Algorithm
LCH4	Liquid Methane
LEO	Low Earth Orbit
LHIAD	Lifting Hypersonic Inflatable Aerodynamic Decelerator
LH2	Liquid Hydrogen
LM	Lunar Module
LOX	Liquid Oxygen
L <sub>s</sub>	Solar Longitude
LSIAD	Lifting Supersonic Inflatable Aerodynamic Decelerator
LoD	Length-to-Diameter
L/D	Lift-to-Drag Ratio
m	meters
m/s	meters/second
MER	Mass Estimating Relationship
MIAS	Mars Inflatable Aeroshell entry System
MJ	Mega Joules
MMOD	MicroMeteroids and Orbital Debris
MOLA	Mars Orbiter Laser Altimeter
MPS	Main Propulsion System
MSL	Mars Science Laboratory
mt	metric ton
MTV	Mars Transfer Vehicle
NA	Not Applicable
NASA	National Aeronautics and Space Administration
NPC	Numerical Predictor-Corrector

NTR	Nuclear Thermal Rocket
OCE	Office of the Chief Engineer
OMS	Orbital Maneuvering System
PDF	Probability Density Function
PICA	Phenolic Impregnated Carbon Ablator
POST2	Program to Simulate Optimized Trajectories (version 2)
PPL	Pin Point Landing
Psia	Pounds Per Square Inch in Air
q	Dynamic Pressure
RCS	Reaction Control System
RD3	Research & Development Degree of Difficulty
RFA	Request for Action
RP	Retro-propulsion
RPS	Radioisotope Systems
RSE	Response Surface Equation
RTG	Radioisotope Thermoelectric Generators
RTV	Room Temperature Vulcanized
SBIR	Small Business Innovative Research
sec	seconds
SIAD	Supersonic Inflatable Aerodynamic Decelerator
SIP	Strain Insulation Pad (Shuttle TPS)
SIRCA	Silicone Impregnated Reusable Ceramic Ablator
SLA	Super Lightweight Ablator
SMC	Strategic Management Council
SMD	Science Mission Directorate
SOA	State of the Art
SRP	Supersonic Retro-propulsion
TDP	Technology Development Program
TIM	Technical Interchange Meeting
TM	Technical Memorandum
TPS	Thermal Protection System
TRL	Technology Readiness Level
T/W	Thrust-to-Weight Ratio
UHF	Ultra High Frequency

XCG	Center of Gravity Location Along the X Body Axis
YCG	Center of Gravity Location Along the Y Body Axis
ZCG	Center of Gravity Location Along the Z Body Axis
$\Delta V$	Delta velocity
$\sigma$	standard deviation

## Acknowledgements

Many individuals, both inside and outside NASA, have contributed to the results of the EDL Systems Analysis Study. We first acknowledge the following individuals who participated directly in EDL-SA activities at some time during the course of this study: Karl T. Edquist, Richard T. French, Aga M. Goodsell, David B. Hash, Tuyen Hua, Ian C. Dupzyk, Eric M. Queen, Adam D. Steltzner, John J. Wagner, Carlos H. Westhelle, Douglas S. Whitehead, Henry S. Wright, and Michael J. Wright.

Next, we appreciate the contributions of the following technology program managers who provided guidance on our Design Reference Missions, Ground Rules and Assumptions and Figures of Merit: David J. Anderson, Samad A. Hayati, Frank Peri and James L. Pittman.

The identification of the transition mechanisms was assisted by Douglas S. Adams, Charles H. Campbell, Allen Chen, Ian Clark, Chiold D. Epp, Karl T. Edquist, Richard T. French, John C. Gallon, Carl S. Guernsey, Steve J. Hoffman, Christian de Jong, Devin M. Kipp, Ashley Korzun, Chris M. Madsen, Donald R. Pettit, Tommaso P. Rivellini, A. Miguel San Martin, Steven W. Sell, Adam D. Steltzner, Mike Tigges, and Aron A. Wolf,

The data used in the assessment of the Programmatic Cost & Risk Figures of Merit were provided by Robin A. Beck, Anthony M. Calomino, Charles H. Campbell, F. McNeil Cheatwood, Karl T. Edquist, Stephen J. Hughes and Charles J. Player.

The data used in the assessment of the Applicability to Other Missions Figures of Merit were provided by David J. Anderson, John W. Dankanich, Samad A. Hayati, Tommaso P. Rivellini, Adam D. Steltzner and Michael J. Wright.

The weighting of the Figures of Merit was performed by F. McNeil Cheatwood, Douglas Craig, Robert Dillman, Bret G. Drake, Dana C. Gould, Samad A. Hayati, James J. Reuther, L. Dale Thomas, Ethiraj Venkatapathy, Henry S. Wright (and Thomas A. Zang).

The preliminary EDL-SA results were critiqued in an Internal Peer Review by F. McNeil Cheatwood, Allen Chen, Juan R. Cruz, Dean A. Kontinos, Charles J. Player, Alan L. Strahan, Ethiraj Venkatapathy, David W. Way and Paul F. Wercinski..

The External Peer Review was performed by Mark Adler, Robert Braun, Anthony M. Calomino, John Connolly, James M. Corliss, Steven G. Labbe and Joseph Olejniczak.

The team is appreciative of the efforts of Farhad Tahmasabi and Harold M. Bell of the Office of the Chief Engineer for their guidance and support, and especially for the efforts of our sponsor, Mike Ryschkewitsch, the NASA Chief Engineer.

Finally, The EDL Systems Analysis Study was only possible because of the persistent and effective advocacy of Walter C. Englund and Stephen P. Sandford.

## EDL-SA Team

Gary A. Allen, Jr.  
James O Arnold  
Jeffery V. Bowles  
Jordi Casoliva  
George T. Chen  
Ian G. Clark  
Melmoth A. Covington  
Jody L .Davis  
Ian C. Dupzyk  
Alicia M. Dwyer Cianciolo  
Karl T. Edquist  
Walter C. Engelund  
Wenhong Fan  
Richard T. French  
Joseph A. Garcia  
Howard E. Goldstein  
Aga M. Goodsell  
Sergey Gorbunov  
David B. Hash  
Austin R. Howard  
Tuyen Hua  
Mark C. Ivanov  
David J. Kinney  
David R. Komar  
Mary E. Livingston  
Eduardo G. Llama  
M. Kathleen McGuire

Michelle M. Munk  
Richard W. Powell  
Dinesh K. Prabhu  
Eric M. Queen  
Jamshid A. Samareh  
David A. Saunders  
Anita Sengupta  
Stephen A. Sepka  
Jeremy D. Shidner  
Ronald R. Sostaric  
Margaret M Stackpoole  
Douglas O. Stanley  
Adam D. Steltzner  
Joseph W. Studak  
Farhad Tahmasebi  
Ethiraj Venkatapathy  
John J. Wagner  
David W. Way  
Carlos H. Westhelle  
Susan M. White  
Douglas S. Whitehead  
Alan W. Wilhite  
Julie A. Williams-Byrd  
Henry S. Wright  
Michael J. Wright  
Thomas A. Zang  
Carlie H. Zumwalt

## Abstract

NASA senior management commissioned the Entry, Descent and Landing Systems Analysis (EDL-SA) Study in 2008 to identify and roadmap the Entry, Descent and Landing (EDL) technology investments that the agency needed to make in order to successfully land large payloads at Mars for both robotic and human-scale missions. This paper summarizes the motivation, approach and top-level results from Year 1 of the study, which focused on landing 10–50 mt on Mars, but also included a trade study of the best advanced parachute design for increasing the landed payloads within the EDL architecture of the Mars Science Laboratory (MSL) mission.

The EDL-SA Study focused on Exploration-class missions in FY 09, i.e., cargo or crewed missions requiring between 10 and 50 mt of landed payload. Candidate technology areas were assessed against a set of eight *EDL-SA Architectures*, i.e., representative architectures (high-level designs) against which the benefits of the technology areas were evaluated. The Study used Design Reference Missions (DRMs), Ground Rules & Assumptions (GR&As) and Figures of Merit (FOMs) that were approved by the managers of the relevant NASA technology programs in May 2009, prior to the execution of the simulations and the evaluations of the FOMs. In evaluating the FOMs, the Study used simulation-based results whenever possible and subjective assessments otherwise. The major simulation-based result was the Mars Arrival Mass, i.e., the total mass of the payload plus the systems needed for Mars Orbit Insertion and Mars EDL.

The key enabling technology areas identified for investment were rigid decelerators, flexible (inflatable) decelerators, supersonic retro-propulsion, precision landing with hazard avoidance, aerocapture, and all-propulsive EDL systems.

# 1 Background

The steps in the study for the Exploration-class missions are shown in Figure 1. The NASA Strategic Management Council (SMC) commissioned the Entry, Descent and Landing Systems Analysis (EDL-SA) Study in May 2008 to identify and roadmap the Entry, Descent and Landing (EDL) technology investments that the agency needed to make in order to successfully land large payloads at Mars for both robotic and human-scale missions. This decision and the governance structure for its implementation are described in internal Agency documents—the Program Decision Memorandum [1] and the Terms of Reference [2] respectively, from August 2008. The EDL-SA Team was composed of members from four NASA centers—Ames Research Center (ARC), Jet Propulsion Laboratory (JPL), Johnson Space Center (JSC) and Langley Research Center (LaRC). The Aeronautics Research Mission Directorate (ARMD), the Exploration Systems Mission Directorate (ESMD), the Science Mission Directorate (SMD) and the Office of the Chief Engineer (OCE) provided funding and oversight. LaRC led the EDL-SA Team, and the oversight was coordinated by the OCE. The project plan was approved in October 2008. Technical work on the project commenced in November 2008.

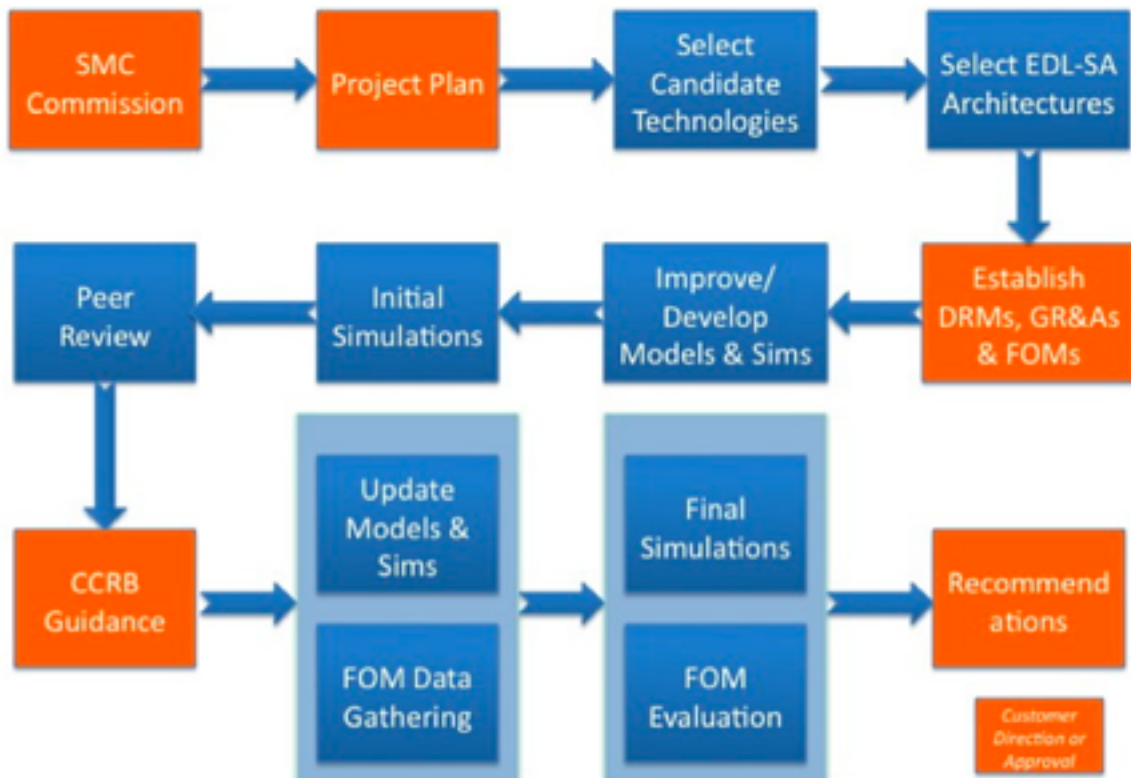


Figure 1. Study Flow

The EDL-SA Team held a brainstorming session in November 2008 to identify candidate technologies for consideration. The context for the technology brainstorming was the Mars Design Reference Architecture 5.0 [3] (DRA5). In keeping with standard practice in systems analysis for technology evaluation, the technologies were assessed against the suite of EDL-SA Architectures. The set of EDL-SA Architectures only needs to include options that encompass all candidate technology areas. The architectures and technologies are described in Section 3.

The Report of the Design Reference Missions, Ground Rules and Assumptions, and Figures of Merit

present the basic guidelines for the study and are provided in Appendix A. The Design Reference Mission was taken to be the Aerocapture and EDL Phases of DRA5. The Figures of Merit are described in Section 6.

To the maximum extent possible existing processes and tools were employed in the EDL-SA Study. Nevertheless, numerous refinements to processes and tools were needed in order to address the specifics of this study. Details on the models and simulations utilized are given in Section 3. The initial simulations and FOM data gathering were performed, and then an External Peer Review (EPR) in September 2009 provided recommendations for improvement. Most of the Requests for Action from this EPR were implemented; however, resource constraints and the priority given by the oversight committee on concentrating on the Large-robotic-class Study in FY 2010 left some recommended work incomplete. Recommendations for follow-on work are provided in Section 9. The Exploration-class Study was wrapped up in February 2010; the principal results from it are summarized in Section 4 to Section 7. Some preliminary work on Large-robotic-class missions was performed the first year. See Section 10 for the formulation, methodology and results.

## 2 Exploration Class Architectures and Technologies

The EDL-SA Team held a brainstorming session at its November 2008 Workshop to identify candidate technologies for consideration. The context for the technology brainstorming was the Exploration-class DRM, namely, the Aerocapture and EDL phases of the Mars Design Reference Architecture 5.0 [3] (DRA5). In fact, one of the Ground Rules for the Study permits only changes to the Aerocapture and EDL phases of DRA5. The baseline EDL architecture—Architecture 1—was that of DRA5: a rigid, mid-L/D aeroshell used for aerocapture and hypersonic entry deceleration, followed by supersonic retro-propulsion. Alternatives to this concept were then identified using a common “tree” approach, and refined by engineering judgment and the availability of reasonable models.

The technology areas that emerged from this brainstorming and subsequent refinement were

- \* Rigid Mid Range Lift to Drag Ratio Aeroshell (Rigid Mid-L/D AS)
- \* Lifting Hypersonic Inflatable Aerodynamic Decelerator (LHIAD)
- \* Supersonic Retro-Propulsion (SRP)
- \* Drag Supersonic Inflatable Aerodynamic Decelerator (DSIAD)
- \* Deployable Lifting Supersonic IAD With Skirt (LSIAD-Skirt)
- \* Dual-Pulse Thermal Protection System (DP TPS-Flexible and DP TPS-Rigid)

The working example of a Rigid Mid-L/D Aero shell is the “ellipsled” used in DRA5, which has an elliptical (current analysis assumes a hemispherical) nose and a cylindrical aft section. No attempt was made to further refine this aerodynamic shape. For Inflatable Aerodynamic Decelerators (IADs), the main distinctions are whether the IAD primarily provides lift or drag and whether it is used at hypersonic or supersonic (or both) speeds. For the thermal protection systems, there is an important distinction between TPS for flexible “aeroshells” (for IADs) or for rigid aeroshells. This set of technologies as reviewed with technology program managers from ARMD, ESMD, and SMD in May 2009. The group did not identify additional technologies to be considered.

During the initial screening process, methods of hard landing such as airbags were eliminated, so all of the architectures assumed powered subsonic phases as the only practical way to attain pinpoint landings next to pre-deployed assets, as required by DRA5. Engineering details such as leg design, crushable segments, and stroke length were not studied. A hazard detection and avoidance system (such as ALHAT) is considered necessary, but sensor requirements were not evaluated in the Year 1 activities.

At the External Peer Review in September 2009, the EDL-SA team received feedback that a rigid, deployable system should have been considered. This option was not carried explicitly because it is in the class of large, blunt-body vehicles to which inflatable decelerators belongs, but the areal mass of deployables is judged to be greater than inflatables, so inflatables were studied as the bounding case. In the future, rigid deployables will appear in the EDL taxonomy and will likely be considered on the roadmaps developed jointly by the EDL-SA and the technology programs. Other systems studies and contracts within the Small Business Innovation Research (SBIR) program have investigated deployables.

Towed ballutes were briefly considered but ultimately judged unwieldy for decelerating masses of this size.

For the purposes of 3-DOF performance simulations, and to stay within the constraints of the study schedule and budget, simplifications were made for modeling the various technologies. The important parameters of aerodynamic decelerators at this level are frontal area, aerodynamic characteristics (L/D), and mass. For instance, an LHIAD was assumed to have enough internal pressure to act as a rigid blunt body, and the mass model reflected the gas and gas generation system necessary to prevent buckling. (The validity of this assumption was investigated in a separate, parallel effort.) All propulsion stages,

whether in the hypersonic, supersonic or subsonic regimes, used a common mass and sizing model.

In keeping with standard practice in systems analysis for technology evaluation, the technologies were assessed against a suite of *EDL-SA Architectures*, i.e., a collection of representative architectures (high-level designs) against which the benefits of specific technology areas can be evaluated. The set of EDL-SA Architectures only needs to include options that encompass all candidate technology areas. The architecture suite is illustrated in Figure 2 and the resulting simplified set of technologies is listed in Table 1. Evaluation of the technologies is accomplished by evaluating metrics at the architecture level, and then extracting the benefits (or penalties) of the technologies pairwise by comparison of architectures that differ only in the specific technologies.

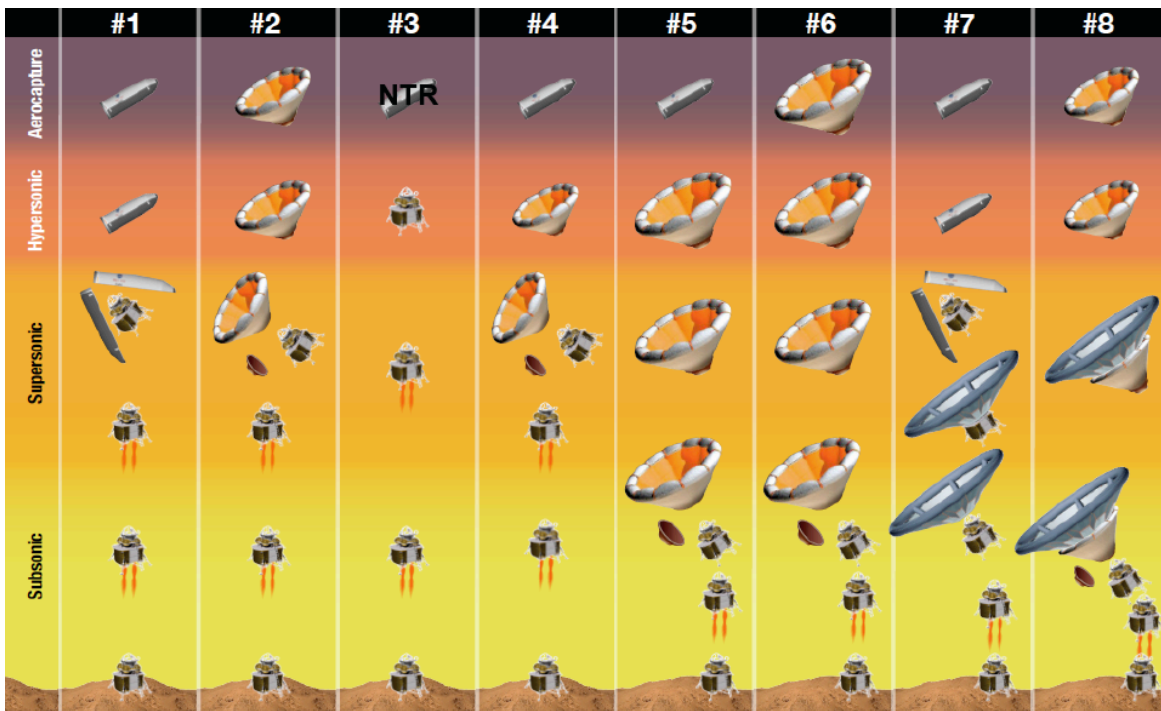


Figure 2. Exploration Class Architectures

Table 1. Simplified Set of Exploration Class Technologies Considered by EDL-SA

	Aerocapture	Hypersonic	Supersonic	Subsonic
Architecture 1	Rigid Mid-L/D AS	Rigid Mid-L/D AS	Propulsion	Propulsion
Architecture 2	Lifting HIAD	Lifting HIAD	Propulsion	Propulsion
Architecture 3	N/A	Propulsion	Propulsion	Propulsion
Architecture 4	Rigid Mid-L/D AS	Lifting HIAD	Propulsion	Propulsion
Architecture 5	Rigid Mid-L/D AS	Lifting HIAD	Same LHIAD	Propulsion
Architecture 6	Lifting HIAD	Lifting HIAD	Same LHIAD	Propulsion
Architecture 7	Rigid Mid-L/D AS	Rigid Mid-L/D AS	Drag SIAD	Propulsion
Architecture 8	Lifting HIAD	Lifting HIAD	LSIAD-Skirt	Propulsion

### 3 Exploration Class Component Model

#### 3.1 Mass Models

There are two key requirements for the EDL-SA mass models: they shall be parametric and consistent across all architectures. Parametric models are mathematical representations that relate the component mass to vehicle dimensions and mission key environmental parameters such as maximum deceleration and total heat load. The model consistency is achieved by sharing similar components across all eight architectures.

The EDL-SA architecture suite contains five unique components (see Figure 3): the rigid mid-L/D aeroshell, a lifting hypersonic inflatable decelerator (LHIAD), a drag supersonic inflatable decelerator (DSIAD), a lifting supersonic inflatable decelerator implemented with a skirt on an LHIAD (LSAID-Skirt), and subsonic/supersonic retro-propulsion (SRP). The details of the mass modeling approach are being documented in a separate NASA report and an AIAA paper to be available in late 2010. The next four subsections provide an overview of parametric mass models for rigid mid-L/D aeroshell, HIAD, SIAD, and SRP.

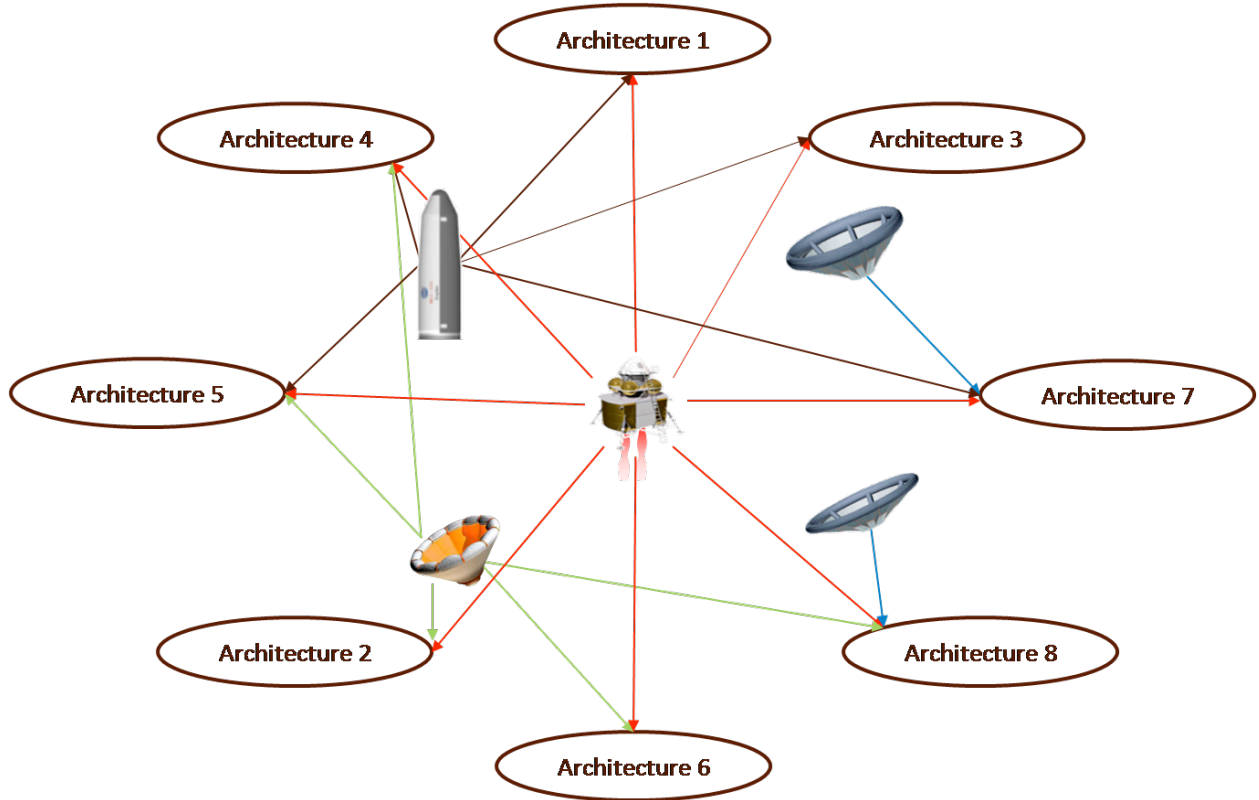


Figure 3. EDL-SA Major Mass Components

##### 3.1.1 Rigid Mid-L/D Aeroshell

The rigid mid-L/D aeroshell is a modified version of the dual-use Ares V shroud used by the DRA5 study. The aeroshell has a straight barrel section with a hemispherical nose cap. The nominal total length is 30 m and the nominal outside diameter is 10 m. (Recent packaging results indicate that a rigid aeroshell with either SRP or SIAD for supersonic deceleration can comfortably fit within the Ares V

shroud; however, simulation results are not yet available for this option.) The mass model for rigid mid-L/D consists of six subcomponents: structure, acoustic blanket, separation mechanism, body flaps, avionics, and TPS.

The Ares-V finite-element (FE) analysis process was used to generate the structural mass estimates. The work was performed by Daniel Pinero and Lloyd Eldred. Loft [4], an in-house computer program, was used to automate the FE model generation with appropriate launch, aerocapture, and entry load cases. NASTRAN® and Hypersizer® were used to analyze and determine optimal structural mass subject to material and buckling constraints that were developed for the Ares V project. The barrel section consists of eight longerons and six frames (divided into five design groups). Hemisphere nose section consists of 8 longerons formed into one design group. Payload is attached to the second and the fifth frames: see Figure 4. A 25% mass growth allowance was added to the optimal mass to account for minimum gage design and required fasteners and other structural components not included in the FE model to obtain a current best estimate of the mass. A

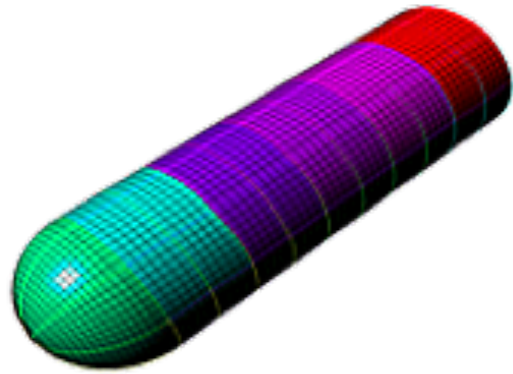


**Figure 4. Finite-Element Model of the Rigid Aeroshell**

response surface equation (RSE) for the structural mass estimate was developed based on FE mass estimates. The RSE includes the following independent variables: diameter, total length, arrival mass, maximum dynamic pressure, and maximum lateral and axial decelerations. Figure 5 shows structural mass variation for nominal cases, excluding system-level mass growth allowance and system-level margin. Acoustic constraints for Mars EDL-SA payload are presently unknown. Mars surface power system may include radioisotope systems (RPSs), which may have a considerable impact on the acoustic blanket design. Standard acoustic blankets are most effective at 400 Hz and above (e.g., Titan IV has a three inch blanket with a one kg/m<sup>2</sup> areal density). The Cassini blanket design was driven by radioisotope thermoelectric generators (RTGs) environment, which was qualified for the Galileo and Ulysses missions. The blanket was designed for 200-250 Hz (six inch blanket with a 3.9 kg/m<sup>2</sup> areal density). Ares V is currently (October 2009) using a heavier, one-inch thinner, blanket (five inch blanket with 6.28 kg/m<sup>2</sup> areal density), and this blanket is used for the rigid aeroshell model. It is recognized that, depending on the packaging schemes selected for the architectures utilizing IADs, the IAD material may serve a dual use as acoustic blanket. Possible packaging arrangements are provided in Section 5. However additional detailed analysis and testing are needed and so for this analysis, the acoustic blanket mass is book kept separately. The mass estimate will be adjusted when there is additional information and a better understanding of Mars EDL payload acoustic requirements and packaging arrangements.

The mass for the body flaps is a point design mass that is added to the aeroshell mass. There are two flaps that are 2 m long by 13.1 m wide; assuming 150 degrees warp angle. The areal density is 16.7 kg/m<sup>2</sup> for flaps and 9.8 kg/m<sup>2</sup> for the TPS. The mass estimate for flaps includes additional mass for actuation, hydraulics, and AU consumables. However the body flaps were not required in the final analysis. The TPS is a dual-layer PICA on top of LI-900, and the mass model is function of reference area and total heat load for aerocapture and entry. The TPS mass includes an attachment mass, which is 44% of the TPS mass and is shown in Table 10. Figure 5 shows TPS mass contours, excluding attachment mass, the system level mass growth allowance, and system margin. Table 2 shows nominal simulation parameters and mass breakdown for rigid mid-L/D aeroshell for Architecture 1.

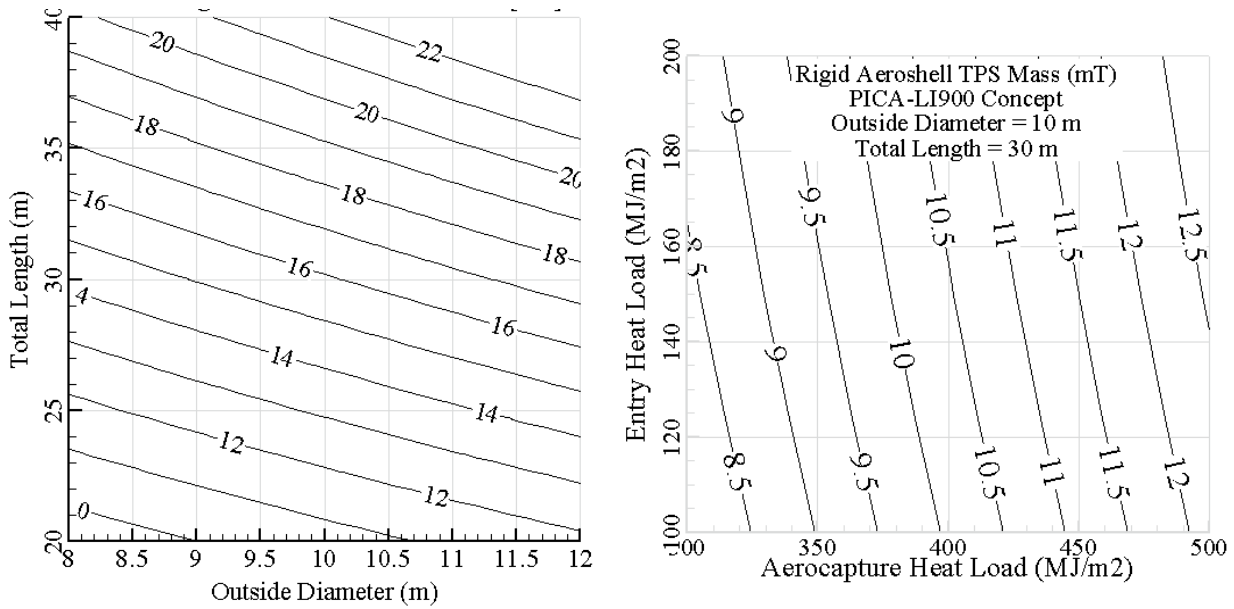


Figure 5. Structural (left) and TPS (right) Mass for the Rigid Aeroshell of Architecture 1

Table 2. Nominal Parameters and Mass Breakdown for Architecture 1

Variable	Value	Mass Components	kg
Diameter, m	10	Structure	5482
Length, m	30	Acoustic Blanket	6415
Aerocapture Heat Load, MJ/m <sup>2</sup>	345	Separation System	2065
Entry Heat Load, MJ/m <sup>2</sup>	130	Avionics	222
Max Dynamic Pressure, kPa	11	Flap	1729
Max Lateral Deceleration, m/s <sup>2</sup>	29	TPS	9199
Max Axial Deceleration, m/s <sup>2</sup>	4	Total	25112
Arrival Mass, mT	110		

### 3.1.2 Hypersonic Inflatable Aerodynamic Decelerator (HIAD)

The HIAD design is based on Mars Inflatable Aeroshell Entry System (MIAS) model [5] which is a 60° sphere-cone aeroshell. The model consists of an inflatable structure, flexible TPS, avionics, separation system, payload adapter and a rigid payload containment structure known as a heatshield. The inflatable mass model is based on the models developed by NASA in the 1960's and 1970's, and the model incorporates a double stacked-toroid consisting of radial straps to tie toroids together and carry radial loads, gores to carry circumference pressure loads, axial straps to carry the buckling loads, torus reinforce fabric to counter the hoop stress, a gas barrier, inflation gas, and gas generators. The straps and reinforcing fabrics are made of Kevlar-49, and the gores and gas barrier are made of Upilex. The mechanical properties of fabrics are reduced for operations in an elevated thermal environment. The design factors of safety for the HIAD follow the NASA standard for soft goods [6].

The toroidal structural concept is based on Brown's design [7] that uses a minimum-weight fiber-reinforced film. The design uses widely spaced reinforcing fibers bonded to the surface of the film, as shown in Figure 6. Brown concludes that the 12X advantage in specific strength of fiber compared to

film results in a 7X lower mass, compared to the same size torus fabricated with unreinforced film for the same burst pressure. It is assumed that the fabric bondline temperature is 200°C with material knockdown factor of 0.5. The material knockdown factor needs further testing for better understanding. The load factor of safety is set to 4 per NASA requirements for soft goods. Figure 7 shows the HIAD inflatable mass contours for various diameter and maximum dynamic pressures based on a 3.6 m heatshield diameter. The inflatable mass includes radial straps, gores, tori, inflation gas, and inflation system with appropriate knockdown factors due to an elevated temperature environment and NASA factors of safety. The solid gas generator is used to produce the inflation gas.

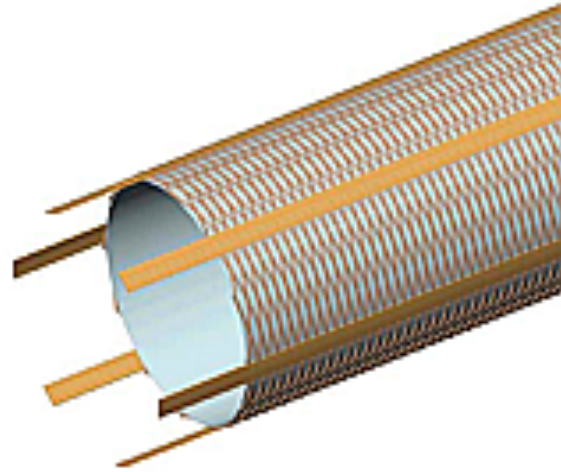


**Figure 6. Reinforcing Fibers**

Brown [8] recommends using 7.55% of launch mass for the adapter. The payload adapter for this study is set to 2% of arrival/entry mass because the adapter is assumed to carry small mechanical load during launch and it is primarily used during the aerocapture and entry phases.

The flexible TPS is silica felt/silicone, and the parametric model is a function of reference area, the aerocapture heat load, and entry heat load. The current flexible TPS mass model is for an ablator that is limited to diameters less than 50 m. The TPS areal density for aeroshell diameters greater than 50 m is held fixed at the areal density of a 50 m aeroshell. The TPS model is suitable for high to moderate heat rates and loads. The use of this TPS model for architecture 6 could produce less accurate results. The next generation of mass model will include a mass model for a flexible insulator that will be suitable for lower heat rates and heat loads. Figure 7 also shows TPS mass contours for Architecture 2 as a function of heat loads. Table 3 shows the nominal parameters and mass breakdown for Architecture 2.

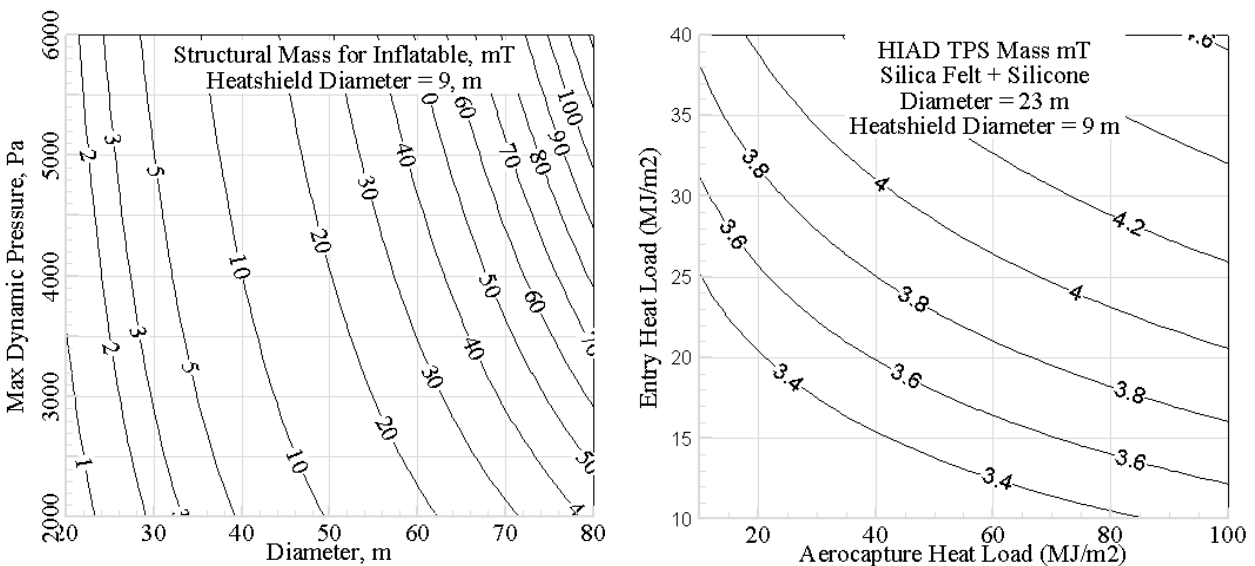


**Figure 7. Structural (left) and TPS (right) Mass for the HIAD of Architecture 2**

**Table 3. Nominal Parameters and Mass Breakdown for Architecture 2**

<b>Variable</b>	<b>Value</b>	<b>Components</b>	<b>Mass, mT</b>	<b>%</b>	<b>Areal Density, kg/km<sup>3</sup></b>
Diameter, m	23.0	Adapter*	2.2	21.2	5.3
Heatshield diameter, m	9.0	Heatshield	1.1	10.2	2.6
Aerocapture Heat Load, MJ/m <sup>2</sup>	87.3	Inflatable	1.8	16.8	4.2
Entry Heat Load, MJ/m <sup>2</sup>	26.1	Avionics	0.1	0.9	0.2
Max Dynamic Pressure, Pa	4240.1	Separation	1.3	12.4	3.1
Payload Mass, mT	40.0	TPS	4.0	38.5	9.7
Arrival Mass, mT	83.6	<b>Total</b>	<b>10.5</b>	<b>100.0</b>	<b>25.1</b>
HIAD Mass, mT	10.5	* [8] 0.0755*support mass +50			

### 3.1.3 *Supersonic Inflatable Aerodynamic Decelerator (SIAD)*

The SIAD, deployed after peak heating, is a hypercone model with no TPS and no knockdown factors for fabric due to high temperature. The SIAD model does include NASA recommended factors of safety for loads. A modeling approach similar to HIAD was used to design the SIAD components.

### 3.1.4 *Supersonic/Subsonic Retro-Pulsion (SRP)*

Architectures 1, 2, and 4 use supersonic RP modules and Architectures 5 through 8 use subsonic RP. Architecture 3 uses RP for the entire EDL segment.

The Exploration Architecture Model for the IN-space and Earth-to-orbit (EXAMINE) [9] modeling tool, developed in-house at LaRC, was used to develop the parametric mass estimates of the SRP stage for all architectures. To eliminate the need for manual performance and sizing iterations, the SRP stage sizing and mass estimation was provided to the trajectory in the form of RSEs that enabled the SRP stage sizing and closure process to be completed simultaneously with trajectory optimization.

Three RSE mass models were generated: one for aero-entry architectures that do not jettison discrete dry mass prior to entry (Architectures 1, 2, 6, 7, 8); one for aero-entry architectures that jettison a portion of the entry system dry mass prior to entry (Architectures 4, 5); and one for the all-propulsive architecture (Architecture 3). Table 4 shows independent variables as well as the upper and lower limits for the response surface equations. Table 5 shows the dependent variables.

The primary SRP structure is an 8.8 m diameter aluminum-lithium (Al-Li) cylinder that supports the tank system and payload. This primary structure mass is estimated from a historically based empirical curve fit [10]. Thrust structure mass is based on a historical fit accounting for stage diameter, the number of engines and the thrust load. Secondary structure mass is 25% of the primary plus thrust structure masses. Landing gear mass is 2.5% of the landed mass on Mars. Multilayer insulation (MLI) is 5 cm thick (39.4 kg/m<sup>3</sup>) covering the exterior structure, providing thermal control of the spacecraft. It is assumed that the payload provides power. The design includes a fluid-cooling loop that collects heat from the avionics cold-plates and cryogenic tankage (up to 10 kW), and heat is returned to payload thermal cooling system for heat rejection. The avionics model includes UHF, X-band, Ka-band communication systems, quad-fault tolerant flight computer, ranging and Doppler used for interplanetary position determination, and dual-fault tolerant laser radar (LADAR) altimeter for precision landing and hazard avoidance.

**Table 4. SRP Independent Variables and Limits for Response Surface Equations**

Architectures	1,2,4,5,6,7,8		3	
	Lower Bound	Upper Bound	Lower Bound	Upper Bound
Payload, mT	10	60	10	60
Terminal Descent $\Delta V$ , km/s	0.2	1.5	4	5.5
Initial T/W (Mars g's)	3	11	1	4
Area Ratio	10	200	10	200
Aeroshell (Struc+TPS+misc), mT	5	55	NA	NA
Aerocapture Apo-Correct. $\Delta V$ , m/s	0	150	NA	NA
Descent Orbit insertion $\Delta V$ , m/s	0	500	NA	NA
Percent pre-entry aeroshell Jettison, %	20*	90*	NA	NA

\*Used for Architectures 4 and 5

**Table 5. SRP Dependent Variables**

Dependent Variables
SRP Initial Mass, mT
Aeroshell initial Mass*, mT
Stack Mass at Arrival, mT
Stack Mass at Entry, mT
Stack Mass at Terminal Descent Initiation
Stack Mass at Landing, mT
SRP Propellant Mass, mT
SRP RCS Propellant Mass, mT
Aeroshell RCS propellant mass*, mT
RP Thrust per Engine
Engine T/W (Mars g's)

\*Not Applicable for Architecture 3

Liquid oxygen (LOX) and liquid methane (LCH<sub>4</sub>) propellants are used for both the main propulsion system (MPS) and the reaction control system (RCS). The MPS has four pump-fed expander engines each operating at 650 psia chamber pressure and a mixture ratio of 3.5. Because stage thrust-to-weight (T/W) and engine area ratio were selected as independent variables, the required thrust varies from case to case and in the overall closure/optimization. Thus, a set of RSEs for the MPS were developed to quickly predict the engine characteristics (vacuum specific impulse, engine thrust-to-weight, engine length and exit diameter) as a function of required thrust and area ratio. Figure 8 shows the specific impulse (Ispv) and engine T/W data used in the performance and sizing analysis.

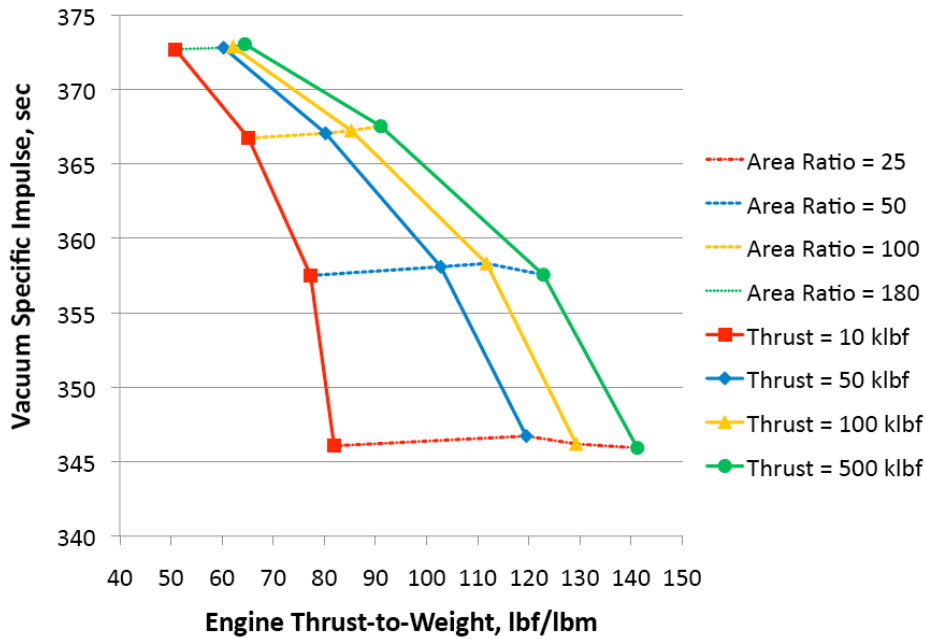


Figure 8. SRP Specific Impulse vs. Engine Thrust-to-Weight

For all architectures except Architecture 3, two Al-Li cylindrical LOX tanks and two Al-Li cylindrical LCH<sub>4</sub> tanks are packaged within the primary structure with the maximum diameter of each MPS tank limited to 3 m. For the all-propulsive Architecture 3, the 2x2 tank packaging arrangement yielded tanks with extremely high length-to-diameters (L/D) due to the need to package the additional propellant required by the all-propulsive case. At high tank L/D the tank and stage structure mass grows fast and does not allow model convergence. Thus, to limit the maximum tank length-to-diameter, an inline tank arrangement was used for Architecture 3 with one forward LOX tank, one aft LCH<sub>4</sub> tank, each limited to 8.8 meters in diameter. For all architectures, the MPS tanks stored propellant at 50 psia and utilized advanced cryogenic propellant management technology to minimize boiloff (50 layers of MLI plus single-stage cryocooling system) and provide autogeneous pressurization and control.

The RCS has sixteen pressure-fed thrusters each producing 100 lbf. Each thruster operates at a chamber pressure of 125 psia, a mixture ratio of 3.0, and an area ratio of 40, delivering a vacuum specific impulse of 334.5 sec. The RCS propellants are stored at 250 psia in two spherical graphite-wrapped aluminum tanks, one for LOX and one for LCH<sub>4</sub>. To minimize boiloff, 30 layers of MLI plus a single-stage cryocooling system are employed while a 6000 psia gaseous helium system provides consumables for RCS tank pressurization.

For all architectures, 100 m/s  $\Delta V$  is allocated for RCS operation during landing. For Architecture 3, an additional 100 m/s  $\Delta V$  is allocated for RCS operation during entry.

Ground rules of the study required the dry mass growth allowance be 15% of the basic dry mass and an additional 30% (of the basic mass) is carried as system level margin. Thus, a total of 45% dry mass reserve is included in the mass estimates. Table 6 shows the mass breakdown for Architectures 1 and 3.

Table 6. SRP Mass Breakdown for Architectures 1 and 3

Mass Item	Arch 1 - Rigid Mid- L/D Aeroshell	Arch 1 - Retro Propulsion Stage	Arch 3 - Retro Propulsion Stage
Primary Body+Thrust Structure	0.0	2076.3	4353.2
Secondary Body Structure	0.0	519.1	1088.3
Aeroshell Structure, TPS, Misc Mass	25111.8	0.0	0.0
Multilayer Insulation	0.0	107.2	83.2
Space Engines & Installation	0.0	1845.9	2623.4
RCS Engines & Installation	202.5	153.7	153.7
MPS Fuel Tanks & Feed/Fill/Drain Sys.	0.0	471.6	1877.4
MPS Oxidizer Tanks & Feed/Fill/Drain Sys.	0.0	512.1	3150.3
RCS Fuel Tanks & Feed/Fill/Drain Sys.	129.9	74.0	267.1
RCS Oxidizer Tanks & Feed/Fill/Drain Sys.	134.4	81.8	310.9
Pressurization System	0.0	90.9	1244.9
Power Management & Distribution	0.0	366.1	366.1
Command, Control, and Data Handling	0.0	12.7	12.7
Guidance & Navigation	0.0	10.3	10.3
Communications	0.0	61.0	61.0
Vehicle Health Management	0.0	0.0	0.0
Cabling and Instrumentation	0.0	35.4	35.4
TCS Heat Acquisition	0.0	120.1	120.1
TCS Heat Transport	0.0	322.9	322.9
TCS Heat Rejection	0.0	325.0	325.0
Landing Legs	0.0	1317.7	1801.6
System Level Margin	7673.6	2551.2	5462.3
Mass Growth Allowance	3836.8	1275.6	2731.1
<b>Dry Mass w/ Growth</b>	<b>37089.1</b>	<b>12330.6</b>	<b>26400.9</b>
Pressurant	2.9	53.2	684.8
Unused Fuel	41.8	73.5	1113.6
Unused Oxidizer	68.9	252.0	3863.4
<b>Inert Mass</b>	<b>37202.6</b>	<b>12709.2</b>	<b>32062.8</b>
Usable OMS Fuel	0.0	3155.8	52258.4
Usable OMS Oxidizer	0.0	11045.3	182904.3
Usable RCS Fuel	2088.9	517.7	3422.1
Usable RCS Oxidizer	3446.7	1553.2	10266.3
<b>Gross Mass</b>	<b>42738.2</b>	<b>28981.2</b>	<b>280913.9</b>

Masses do not include 15% Project Mass Growth Allowance

## 3.2 Aerodynamic and Aerothermal Modeling

Two classes of vehicle configurations were analyzed during the first year of the study: 1) a rigid, mid-L/D vehicle and 2) a low-L/D flexible vehicle often referred to as the Hypersonic Inflatable Aerodynamic Decelerator or HIAD concept. Figure 9 presents the vehicle configurations as analyzed for the first year effort.

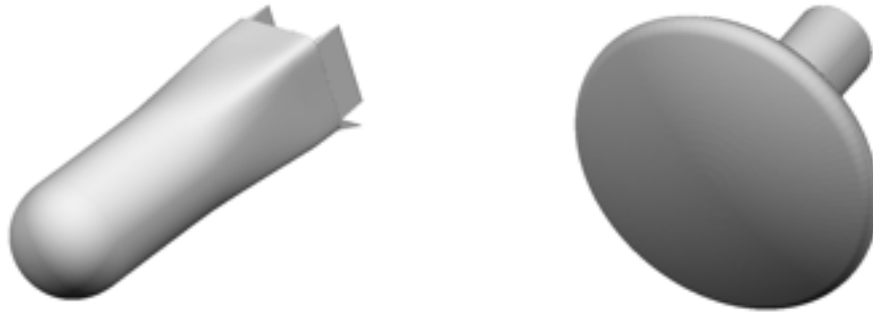


Figure 9. Mid L/D (left) and HIAD (right) Vehicle Configurations

### 3.2.1 Tool Set

A suite of engineering and high-fidelity aerodynamic and aerothermal analysis tools was used to develop the aerodynamic and aerothermal databases for the two vehicle configurations depicted in Figure 9. The analysis tools including CBAERO [11], DPLR [12] [13], LAURA [14] [15], NEQAIR [16], and CART3D [17].

The CBAERO software package is an engineering level aero-thermodynamics tool for predicting the aerodynamic and aero-thermodynamic environments of general vehicle configurations. CBAERO makes use of an unstructured surface grid of triangles to define the outer mold line of the vehicle configuration. No volume mesh is required. Solution times are on the order of seconds on a typical desktop computer for providing integrated forces and moments as well as the full aerothermal environments over the entire vehicle surface. For the present work CBAERO is used as the basis of the engineering-level aerodynamic and aerothermal analyses upon which corrections, based on high-fidelity CFD, are applied.

The two high-fidelity CFD codes used in the development of the aerodynamic and aerothermal databases included: The Langley Aerothermodynamic Upwind Relaxation Algorithm (LAURA) code and the NASA Ames' Data Parallel Line Relaxation (DPLR) code. These codes solve finite-volume formulations of the Reynolds-averaged Navier-Stokes equations, including chemistry affects.

The prediction of shock radiation was performed with NEQAIR. NEQAIR is a line-by-line spectroscopy and one-dimensional radiation transport tool. The code computes radiation transport (from the free stream to the vehicle surface) along straight lines of sight using a tangent-slab approximation. The data at points on a line of sight are obtained through interpolation from a volume solution computed using DPLR or LAURA, i.e., radiative heating is obtained assuming the flow and radiative processes are uncoupled. NEQAIR constructs accurate spectra at every point on a line of sight, computes the integrated radiative intensity from the spectral distribution, and transports the energy to the next point on the line of sight through one-dimensional transport.

Finally, CART3D is a high-fidelity inviscid analysis package for conceptual and preliminary aerodynamic design, allowing users to quickly perform automated CFD analysis on complex geometries. The package includes utilities for geometry import, surface modeling and intersection, mesh generation, flow simulation and post-processing of results. The CART3D packaged was used to provide rapid

turnaround of aerodynamic solutions in the subsonic and low supersonic regimes.

### 3.2.2 Mid-L/D Geometry

The mid-L/D rigid vehicle concept was based on a nominal 10x30 meter reference geometry used during the Mars DRA5 study. The original DRA5 configuration, based on a simple cylinder and spherical nose cap geometry had no provisions for body flaps or speed brakes. The present concept slightly modified the aft body section to allow for the incorporation of both a body flap and speed brakes. The nominal hypersonic L/D is 0.5 at angle of attack of 55°. The configuration was constrained to fit within the Ares V shroud, as specified defined by the EDL-SA ground rules.

The aerodynamic model covers Mach 1.3 through 50, angles of attack of 0 through 90°, and dynamic pressures of 1.E-7 through 0.75 bars. The aerodynamic models covers body flap deflections in the range of -10 to 50°, and the speed brake for the range of 0 to 60°. The aerodynamic model was developed using three separate aerodynamic models generated with the DPLR, CART3D, and CBAERO software packages. Over 600 high-fidelity CART3D solutions were run on the baseline, as well as a control-surface-deflected configuration. DPLR was run at a single (Mach 33) flight condition to anchor the high Mach number aerodynamics. Representative solutions from DPLR, CART3D, and CBAERO are shown in Figure 10, Figure 11 and Figure 12. Note that while the CART3D and CBAERO configurations included the full details of the body flap and speed brake, the DPLR geometry was simplified to remove the gaps between the control surfaces.

The aerodynamic database is a merger of the aerodynamic solutions from DPLR, CART3D, and

CBAERO. The DPLR solutions were used to adjust the CBAERO solutions at high Mach number using a simple delta correction form. The CART3D solutions were used exclusively below Mach 5, with the exception that the CBAERO viscous forces and moments were used to adjust the inviscid CARTD solutions. For the Mach numbers from 5 to 10 the CART3D and CBAERO solutions were linearly weighted such that the solution ramps from purely CART3D solution at Mach 5 to the purely CBAERO solution (anchored against DPLR) at Mach 10.

The detailed aerothermal model is based on the previous DRA5 analyses and covers Mach 1.3 through 50, dynamic pressures of 1.E-7 through 0.75 bars, at a

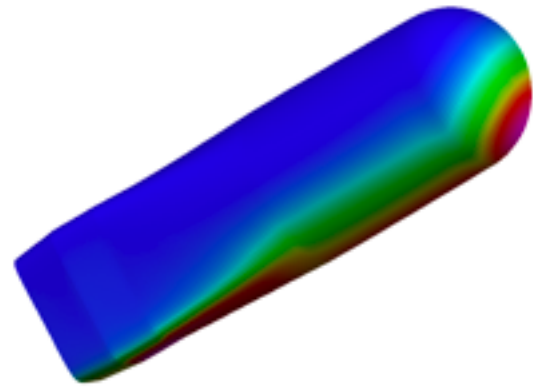


Figure 10. Representative DPLR Solution

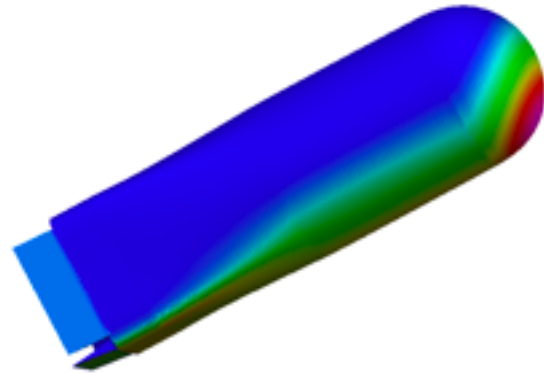


Figure 11. Representative CBAERO Solution

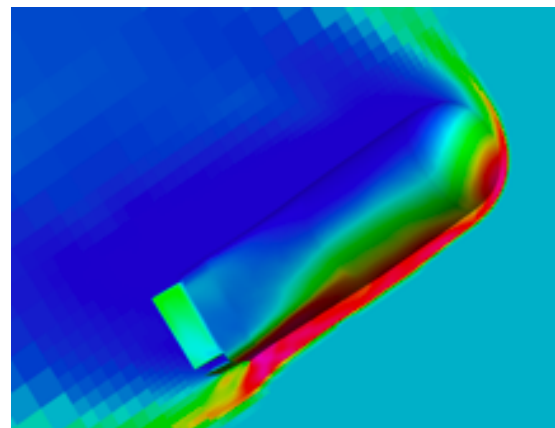


Figure 12. Representative CART3D Solution

single angle of attack of 55°. The 55° angle of attack corresponds to the nominal L/D of 0.5. The database was created using CBAERO and is anchored against a single DPLR/NEQAIR solution set at Mach 33, corresponding to the DRA5 peak total heating point. The aerothermal database provides the aerothermal environments over the entire vehicle surface. The flow was assumed to be fully turbulent, fully catalytic, with a radiative equilibrium wall boundary condition. The surface emissivity was assumed to be 0.85, although this value is subsequently adjusted in the TPS analysis based on the material selections.

### **3.2.3 Flexible Low-L/D Vehicle (HIAD)**

Initial studies for the low-L/D flexible vehicle concept pointed led to a design L/D of 0.3 and a baseline diameter of 23 meters. An initial configuration based on a 60° and 70° sphere-cone configurations were chosen based on similar studies, specifically the Russian MIAS concepts, and the heritage of the Viking 70° sphere-cone geometry. However, the poor aerothermal behavior of these sphere-cone shapes, specifically the augmented turbulent heating due to entropy swallowing affects, led the design towards a constant radius heat shield configuration based on the Apollo geometry. The final configuration is shown in Figure 9 has a nominal L/D of 0.3 at approximately 20° angle of attack. Note, for this study the payload and 'backshell' configurations were undefined, and were assumed to have small impacts on the supersonic and hypersonic aerodynamics. For subsonic Mach numbers a simplified payload configuration was assumed.

In the supersonic and hypersonic ranges, the similarity of the HIAD configuration to the Crew Exploration Vehicle (CEV) heat shield permitted the leveraging of the existing CEV aerothermal database. The CEV aerothermal database is a combination of high-fidelity CFD and engineering methods. The high-fidelity CFD codes, DPLR and LAURA, are used for the prediction of convective heating, and NEQAIR for the prediction of shock radiation heating. The high-fidelity CFD codes are run sparingly at critical conditions that bound the expected flight envelope. The engineering-level analysis code, CBAERO, is then anchored against the high-fidelity CFD and used to create a dense aerothermal database for use in TPS selection and sizing.

For the present flexible configuration, the existing CEV aerothermal database was leveraged by using CBAERO to adjust for both scale (5 m to 23 m) and planet (Earth to Mars). The resultant aerothermal database provided the aerothermal environment over the entire vehicle surface. A representative, anchored, CBAERO solution for the flexible configuration is shown in Figure 13. Integration over the surface of the predicted pressures and shears provided the integrated forces and moments used in the aerodynamic database for all supersonic and hypersonic Mach numbers. For subsonic and transonic Mach numbers the CART3D package was used to calculate the forces and moments on the 23-meter HIAD with a representative payload container attached. Estimates for the viscous drag at these lower Mach numbers were obtained using CBAERO. A representative subsonic CART3D solution for the flexible configuration is also shown in Figure 13. The final aerodynamic and aerothermal model covers Mach 0.3 through 50, angles of attack of 0 through 33°, and dynamic pressures of 1.E-7 through 0.75 bars.

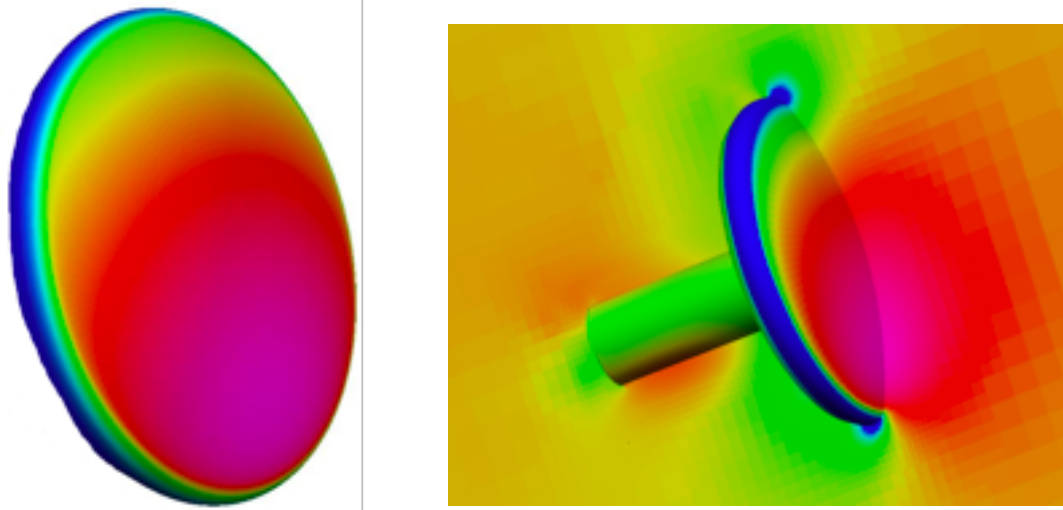


**Figure 13. Anchored CBAERO Solution (left) and Subsonic CART3D Solution (right)**

### **3.3 Aerocapture/EDL Guidance Algorithms**

Several guidance algorithms were developed and used to design both the aerocapture and EDL portions of flight. The guidance algorithms considered, assessed the feasibility of each architecture to aerocapture with acceptable margin and to maneuver during entry such that the vehicle could reach a specified target. Algorithms considered included the Hybrid Predictor-Corrector Aerocapture Scheme, (HYPAS), a Numerical Predictor Corrector Guidance (NPC), a theoretical “all knowing” guidance and an Apollo derived Analytical Predictor Corrector Guidance. For entry analysis, the theoretical guidance was used because of its ease of implementation and relatively quick run time. However to validate the EDL results, entry performance was compared to select simulations using both the NPC and APC guidance.

#### **3.3.1 HYPAS (Hybrid Predictor-Corrector Aerocapture Scheme)**

The HYPAS aerocapture guidance algorithm [18] [19], developed at JSC, guides a lifting vehicle through the atmosphere to a desired exit orbit apoapsis and inclination using bank angle control. The guidance uses an analytically derived control algorithm based on deceleration due to drag and altitude rate error feedback. Inputs to the guidance algorithm are the current vehicle position, velocity, sensed acceleration, and body attitude. The algorithm outputs a commanded bank angle and the direction to bank from the current attitude. The guidance algorithm is adaptable to a wide range of initial state vectors, vehicle lift-to-drag ratios and ballistic coefficients, planetary atmospheres, and target apoapsis and inclinations by only changing a set of initialization constants. Furthermore, by tuning these constants, other trajectory constraints can be controlled such as maximum dynamic pressure, deceleration, heat rate, and the amount of the theoretical corridor captured.

A significant feature of the HYPAS algorithm is that no reference trajectories are computed prior to flight; all references are computed and updated during flight. This analytic, “on-the-fly” approach leads to efficient code, minimal data storage requirements, and minimal preflight effort. The non-numerical, non-iterative scheme ensures fast and consistent execution times.

The original version of the HYPAS algorithm was developed for the Aeroassist Flight Experiment (AFE) program. During the AFE program, the algorithm was tested, compared, and evaluated against

other guidance algorithms in three and six degree-of-freedom computer-based simulations. The HYPAS guidance algorithm was selected for the space flight test, and development of the flight code was on schedule until the AFE program was cancelled. Since the AFE program, the HYPAS algorithm has been used in numerous human and robotic exploration mission studies. These studies involved developing nominal and dispersed trajectory simulation results for aerocapture at Earth, Mars, Titan and Neptune for a wide range of vehicle L/D, ballistic coefficients, entry conditions, and target orbits. HYPAS was also in the evaluation phase for the NASA/CNES 2005 Mars Sample Return Mission [20] [21], which included an aerocapture orbiter at Mars. This work has provided the opportunity to gain a deep understanding of how the guidance algorithm performs in a variety of situations. Modifications have been made as necessary to improve performance and robustness.

The HYPAS guidance algorithm consists of two phases. In the first phase, or capture phase, bank angle commands are generated to stabilize the trajectory and drive the vehicle toward equilibrium glide conditions, where lift, gravity, and centripetal forces are balanced. When the vehicle decelerates to a specified velocity, the second phase, or exit phase, begins. In the exit phase, the velocity vector at atmospheric exit altitude is analytically predicted each guidance computation cycle. Bank angle commands are then generated so that the velocity achieved at exit altitude will produce an orbit with the target apoapsis. This two-phase approach allows separate tuning of initialization constants to maximize robustness during capture and maximize performance during exit.

Target apoapsis is achieved by controlling the vertical component of the lift vector through bank angle commands. The guidance algorithm follows a reference altitude rate and drag profile, generating bank angle commands using the control equation

$$\cos \phi_{cmd} = \cos \phi_{eq.gl.} - G_h \left( \frac{\dot{h} - \dot{h}_{ref}}{\bar{q}} \right) + G_d \left( \frac{D - D_{ref}}{\bar{q}} \right)$$

where  $\phi_{cmd}$  is the commanded bank angle,  $\dot{h}$  is the altitude rate,  $\bar{q}$  is the dynamic pressure,  $D$  is the deceleration due to drag, and  $\phi_{eq.gl.}$  is the bank angle required for equilibrium glide.  $G_h$  and  $G_d$  are gains selected to provide the desired natural frequency and damping ratio response to a second order differential equation in altitude. Their values can be adjusted to maximize performance or robustness.

During the capture phase, when equilibrium glide is targeted, the reference altitude rate,  $\dot{h}_{ref}$  is zero, and the reference drag is computed each cycle by

$$D_{ref} = K \left( \frac{V_I^2}{R} - g \right) \frac{C_D}{C_L}$$

where  $V_I$  is current inertial velocity,  $R$  is current radius vector magnitude,  $g$  is acceleration due to gravity,  $C_L$  and  $C_D$  are lift and drag coefficients, and  $K$  is a factor to determine how much of the lift vector should be used to maintain equilibrium glide. The guidance will attempt to insure the vehicle will not skip out by balancing the vertical forces. Selection of the gains controls the point in the entry in which equilibrium glide is established, thereby controlling heat rate and g-loads.

During the exit phase of the guidance, a constant reference altitude rate is computed so that the velocity at atmospheric exit will provide the desired target apoapsis altitude. This reference altitude rate is updated each guidance cycle based on the difference between the predicted and desired exit velocity. The equation for updating the reference altitude rate is

$$\dot{h}_{ref}^{(1)} = \dot{h}_{ref}^{(0)} + \frac{V_{miss}}{(dV_{miss} / d\dot{h})}$$

where  $V_{miss}$  is the difference between the predicted velocity at exit and the velocity required at exit to achieve the apoapsis target with given reference altitude rate. The predicted exit velocity is computed from an analytic equation that assumes an exponential atmosphere and constant radial velocity to atmosphere exit for estimating velocity loss due to drag. The desired exit velocity is simply computed from orbital mechanics equations.

The guidance algorithm requires an estimate of the current atmospheric density. An estimate of the density is derived from the measured deceleration due to drag assuming a nominal ballistic coefficient using

$$\rho_{mes} = \frac{2D_{mes}}{V_r^2} \left( \frac{m}{C_D S} \right),$$

where  $V_r$  is the current relative velocity, and  $D_{mes}$  is the sensed deceleration due to drag. The guidance algorithm models the atmosphere density as a simple exponential law of altitude

$$\rho_{exp} = \rho_0 e^{(h_0 - h)/h_s}$$

where  $\rho_0$ , and  $h_0$ , are the reference density and altitude, and  $h_s$  is the scale height. A density scale multiplier  $K_\rho$  is defined as the ratio of the density expected from the exponential model and the measured density. A first order low-pass filter of the form

$$K_\rho = (1 - K)K_\rho + K(\rho_{mes} / \rho_{exp})$$

is used to smooth high-frequency atmosphere disturbances and control the guidance response rate to density changes. Then, the estimate of the atmosphere density is computed by

$$\rho_{est} = K_\rho \rho_{exp}$$

Note that with this approach, the guidance algorithm automatically compensates for dispersions in both atmospheric density and vehicle drag coefficient.

Bank reversals are performed periodically to achieve the target orbit inclination. The lateral logic in the guidance algorithm uses an inclination or wedge angle dead band that is a function of inertial velocity. Whenever the inclination or wedge angle error exceeds this dead band, a roll reversal is commanded. The direction to bank is selected through a series of tests that examine current velocity, angular distance to roll, and difference between reference and navigated altitude rate.

### 3.3.2 Numerical Predictor Corrector Guidance (NPC)

The Numerical Predictor Corrector algorithm [22] was originally developed as candidate guidance for both the aerocapture and entry of the Mars Surveyor Program 2001 mission and the aerocapture of CNES Mars 2005 Sample Return Orbiter. Orion is developing a NPC for its lunar return guidance. The NPC algorithm operates using an outer loop called every simulation time step and an inner loop, called at some specified interval (e.g. every 10 seconds). For the EDL-SA implementation, the NPC receives perfect navigated state conditions (position and velocity) as well as current roll angle and sensed body-axis accelerations. The algorithm integrates 3DOF translational equations of motion using a fourth-order Runge-Kutta integration scheme.

The inner loop includes models of the planet, gravity field, vehicle aerodynamics, body attitude, mass properties and atmosphere. The inner loop of the algorithm produces a command vector that includes roll

angle and reversal time. A state history, including range to target, energy and time rate of change in energy is also stored. The state information is used to modify the roll angle magnitude between updates.

The alteration is done in the outer loop by comparing the actual state conditions with the predicted state conditions and then modifying the roll angle appropriately. A half-interval search method is used to determine the appropriate roll angle and reversal time. Sensed acceleration data is used to update the internally stored atmosphere density profiles and aerodynamics. This is done by calculating the ratios of normal and axial sensed acceleration and comparing them to the values predicted by the guidance algorithm. In addition, the guidance routines are used to calculate a local density scale height. By knowing both the aerodynamic accelerations ratios and the local density scale height, scalar multipliers to the guidance predicted aerodynamics and an altitude bias to the guidance atmosphere model can be calculated. These scalar multipliers and altitude bias quantities are averaged over a 10 second intervals and the averages are used within the inner loop.

The predictor corrector inner loop is activated on a deceleration trigger that is tailored for each architecture. Once the predictor-corrector is invoked, the vehicle guidance strategy is a combination of roll angle magnitude and roll reversal. The general strategy is to iterate on the roll angle magnitudes until the predicted miss distance is within a preselected tolerance. Roll reversals are commanded if the heading error exceeds a preset limit. Roll angle magnitude and reversal times are then passed to the outer loop for execution.

### ***3.3.3 Theoretical EDL Guidance***

The “Theoretical EDL Guidance” was developed as highly adaptable to support all the architectures. It also had the ability to be detuned such the results would be comparable to those expected from flight guidance algorithms. It is POST2 based and has full knowledge of all environmental parameters such as aerodynamics, atmospheric density and wind profiles. The flight phases are representative of the numerical predictor-corrector and the Apollo-derived algorithms that were used in this study. The theoretical guidance used bank angle magnitude to control the range to the target and bank angle direction to control crossrange. After the range control phase the guidance switched to a heading alignment phase where the guidance used bank angle to remove any residual cross range error, and placed the vehicle at the proper velocity, altitude and range from the target to initiate the staging and propulsive descent phase.

### ***3.3.4 Analytic Predictor-Corrector – Apollo-Derived Guidance***

The Analytic Predictor-Corrector (APC) used in the EDL-SA is a combination of a modified Apollo entry guidance [23] and the Apollo powered descent guidance [24]. The modified Apollo entry guidance was a candidate guidance algorithm for both the aerocapture and entry of the Mars Surveyor Program 2001 mission, and the aerocapture of CNES Mars 2005 Sample Return Orbiter. It is the guidance used for the MSL Entry, and will be the guidance for Orion return from the ISS. The modified Apollo powered descent guidance is currently under evaluation for Altair’s lunar propulsive descent guidance.

#### ***Atmospheric Entry Phase***

*Guidance Logic* – In this section, an overview and the main characteristics of the Apollo-derived entry terminal point controller are presented. The original Apollo atmospheric entry guidance was designed for lunar return; however, sufficient mission flexibility was required to accommodate the large variations in actual entry conditions, including those of Earth orbit test flights and all types of lunar mission aborts. To satisfy re-designation requirements for a weather alternate landing area, an upper altitude controlled skip entry capability was included. However, the Mars entry application considered in this paper does not require a skip phase. Therefore, only the final entry phase will be used.

The final entry phase algorithm controls to a terminal range and velocity target using pre-derived influence coefficients with respect to errors about a nominal L/D reference trajectory. This reference

trajectory is defined by range-to-go, drag acceleration, and altitude rate as a function of relative velocity.

The predicted range-to-go ( $R_p$ ) is calculated as a function of drag ( $D$ ) and altitude rate ( $\dot{r}$ ) errors with respect to the nominal reference trajectory profile and the associated influence coefficients; see equation 1.

$$R_p = R_{ref} + \frac{\partial R}{\partial D}(D - D_{ref}) - \frac{\partial R}{\partial \dot{r}}(\dot{r} - \dot{r}_{ref}) \quad 1$$

The commanded vertical component of the lift-to-drag ratio is calculated as the addition of the reference L/D plus a function of the difference between the actual and predicted range to go

$$\left(\frac{L}{D}\right)_c = \left(\frac{L}{D}\right)_{ref} + \frac{K(R - R_p)}{\partial R / \partial (L/D)} \quad 2$$

The commanded bank angle is then calculated as

$$\phi_c = K_{bank} \cos^{-1}\left(\frac{(L/D)_c}{L/D}\right) \quad 3$$

where  $K_{bank}$  is the bank directional control ( $\pm 1$ ). The sign of  $K_{bank}$  is reversed each time the target crossrange out-of-plane central angle exceeds the reversal criterion, which is a quadratic function of the relative velocity.

The partial derivatives of predicted range in equations 1 and 2 are the controller gains, which are derived using linear perturbation theory with the nominal reference trajectory by reverse integration of the differential equations adjoint to the linearized equations of motion. Optimized control gains for converging the dispersed trajectory are implemented in the guidance as tabular functions of relative velocity. Because of slow system and trajectory responses to guidance commands, performance is empirically enhanced by the use of the over-control gain  $K$  in equation 2 to improve range convergence behavior.

To minimize disturbance of downrange control near the target, bank reversals are inhibited below a certain relative velocity magnitude. If the bank command is not in the same direction as the target at this point, then a final reversal is commanded prior to setting the inhibit flag. After that, a heading control phase is initiated in which the bank command is defined by

$$\phi_c = K_{hc} \tan^{-1}\left(\frac{C_r}{D_r}\right)$$

where  $K_{hc}$  is the overcontrol gain for the heading control phase and where  $C_r$  and  $D_r$  are the crossrange and downrange to the target, respectively.

*Methodology* – The reference trajectories basically consist of two segments. The first one, covering velocities approximately higher than 2 km/s, usually requires large bank angles such that the constraints on heat load, heat rate, and deceleration loads are met. The second segment, covering velocities lower than 2 km/s, is designed such that the vertical lift of the entry vehicle be increased in order to further reduce the terminal relative velocity at a given terminal altitude. Vertical lift margin is provided in this segment in order to allocate dispersions. However, the reference trajectory for the final part of this last segment calls for a full lift up configuration below the velocity at which the heading control phase is set

to start.

### ***Powered Descent Phase***

*Guidance Logic* – The guidance logic for this phase is a quadratic guidance that uses a pre-stored gravity turn steering thrust reference profile that reaches the landing site at the touchdown conditions. It commands thrust and attitude to reduce position and velocity errors at touchdown.

In this logic, the acceleration profile (a) is restricted to a quadratic equation

$$a = c_0 + c_1t + c_2t^2 \quad 4$$

The acceleration profile is integrated to develop the analytic equations for velocity and position

$$v = \int_{t_0}^t adt = c_0(t - t_0) + \frac{1}{2}c_1(t - t_0)^2 + \frac{1}{3}c_2(t - t_0)^3 + v_0 \quad 5$$

$$r = \int_{t_0}^t vdt = \int_{t_0}^t \int_{t_0}^t adt = \frac{1}{2}c_0(t - t_0)^2 + \frac{1}{6}c_1(t - t_0)^3 + \frac{1}{12}c_2(t - t_0)^4 + v_0(t - t_0) + r_0 \quad 6$$

Equations 4, 5 and 6 can be rewritten as

$$tgo = t - t_0$$

$$a_t = c_0 + c_1tgo + c_2tgo^2$$

$$v_t - v_0 = c_0tgo + \frac{1}{2}c_1tgo^2 + \frac{1}{3}c_2tgo^3$$

$$r_t - r_0 - v_0tgo = \frac{1}{2}c_0tgo^2 + \frac{1}{6}c_1tgo^3 + \frac{1}{12}c_2tgo^4$$

Where the target tgo, r<sub>t</sub>, v<sub>t</sub>, and a<sub>t</sub> come from the reference profile. Solving for the coefficients c<sub>0</sub>, c<sub>1</sub>, and c<sub>2</sub> in matrix form results in

$$\begin{pmatrix} c_0 \\ c_1 \\ c_2 \end{pmatrix} = \begin{pmatrix} 1 & -6/tgo & 12/tgo^2 \\ -6/tgo & 30/tgo^2 & -48/tgo^3 \\ 6/tgo^2 & -24/tgo^3 & 36/tgo^4 \end{pmatrix} \begin{pmatrix} a_t \\ v_t - v_0 \\ r_t - r_0 - v_0tgo \end{pmatrix}$$

Hence, the generic acceleration command for each axis is given by

$$a_{cmd} = c_0 + c_1t + c_2t^2$$

Thus, the thrust command is given by

$$T_{cmd} = \sqrt{a_x^2 + a_y^2 + a_z^2}$$

At each guidance call, the coefficients are recalculated in each axis and  $t$  is set to zero. The initial state for the two-point value boundary value problem is the current vehicle state. The burn length to go,  $t_{go}$ , will decrease as the vehicle approaches the target state. As  $t_{go}$  becomes very small, the coefficient terms will tend toward infinity. There are typically two different methods employed to prevent this from happening. One method is to use a target state that forces the vehicle to follow the desired trajectory path without the intent of actually reaching that target. The guidance phase is then terminated prior to  $t_{go}$  approaching zero. The second method is to utilize a fine count, where the coefficients are not recalculated after  $t_{go}$  goes below a pre-selected value  $t_{fc}$  (typically 1-2 sec). During the fine count, the coefficients are not recalculated, and  $t$  is not reset at each guidance call.

The pointing direction in terms of pitch and yaw are calculated as follows

$$\begin{aligned} pitch &= \arctan(a_x/a_z) - \pi/2 \quad f \text{ ora}_z > 0 \\ pitch &= \arctan(a_x/a_z) + \pi/2 \quad f \text{ ora}_z < 0 \\ pitch &= 0 \quad f \text{ ora}_z = 0 \\ yaw &= \pi/2 - \arctan\left(a_y/\sqrt{a_x^2 + a_z^2}\right) \quad f \text{ ora}_y > 0 \\ yaw &= -\left(\pi/2 + \arctan\left(a_y/\sqrt{a_x^2 + a_z^2}\right)\right) \quad f \text{ ora}_y < 0 \\ yaw &= 0 \quad f \text{ ora}_y = 0 \end{aligned}$$

*Methodology* – The reference profile is a gravity turn trajectory that consists of three segments: a constant thrust level, followed by a ramp down, and a smaller constant thrust level. Two target points are determined for the whole trajectory, one is set at the end of the ramp down segment for a few seconds before the end of the trajectory, and the other is set at the end of the trajectory, which ends at the predetermined final conditions. The fine count method is the one that has been used in the study, with a  $t_{fc} = 2$  sec.

### 3.3.5 Guidance Comparison

Figure 14 shows the comparison of a Monte Carlo analysis using APC, NPC and theoretical guidance's for Architecture 1. Both high fidelity guidance algorithms (APC & NPC) can provide the required targeting accuracy (10 m with perfect navigation) and have minimal impact on the design parameters (max g's, max heat rate and load, staging conditions, etc). Results are similar for Architecture 2 results not shown here.

Figure 15 shows a similar comparison for Architecture 8. Unlike the Architecture 1 and 2 results, the current detuning level of theoretical guidance may not be sufficient as the theoretical guidance analysis uses significantly less propellant. Also note that the APC terminal descent guidance produces tighter propellant statistics than current NPC strategy.

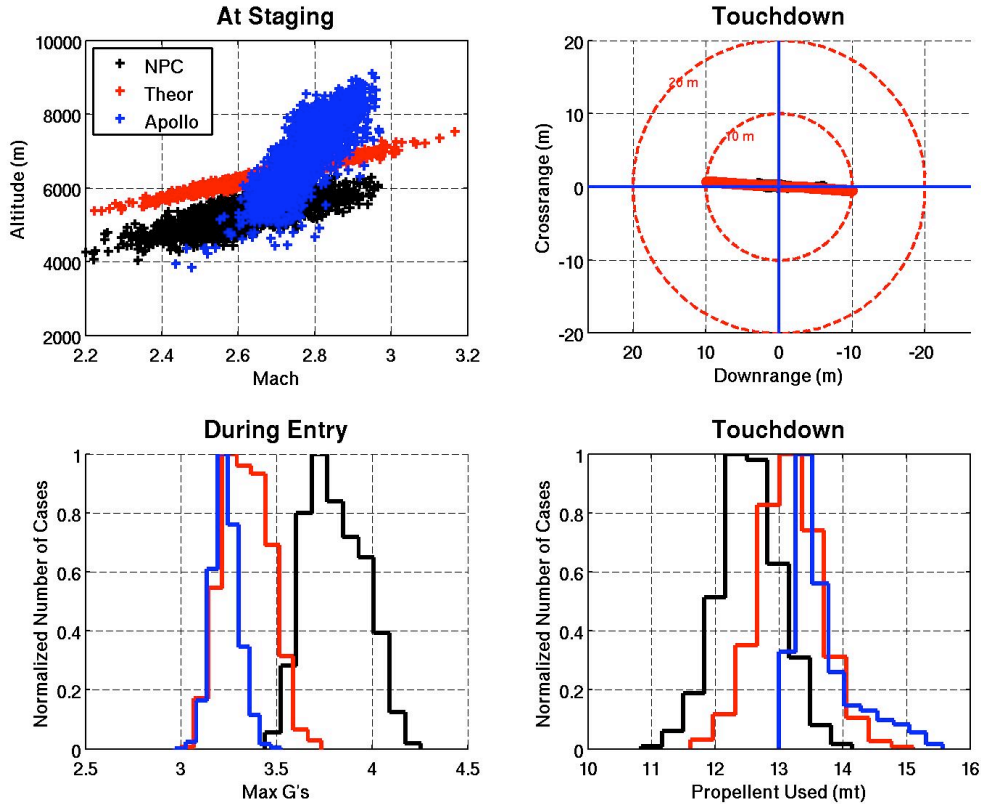


Figure 14. Guidance comparison for Architecture 1.

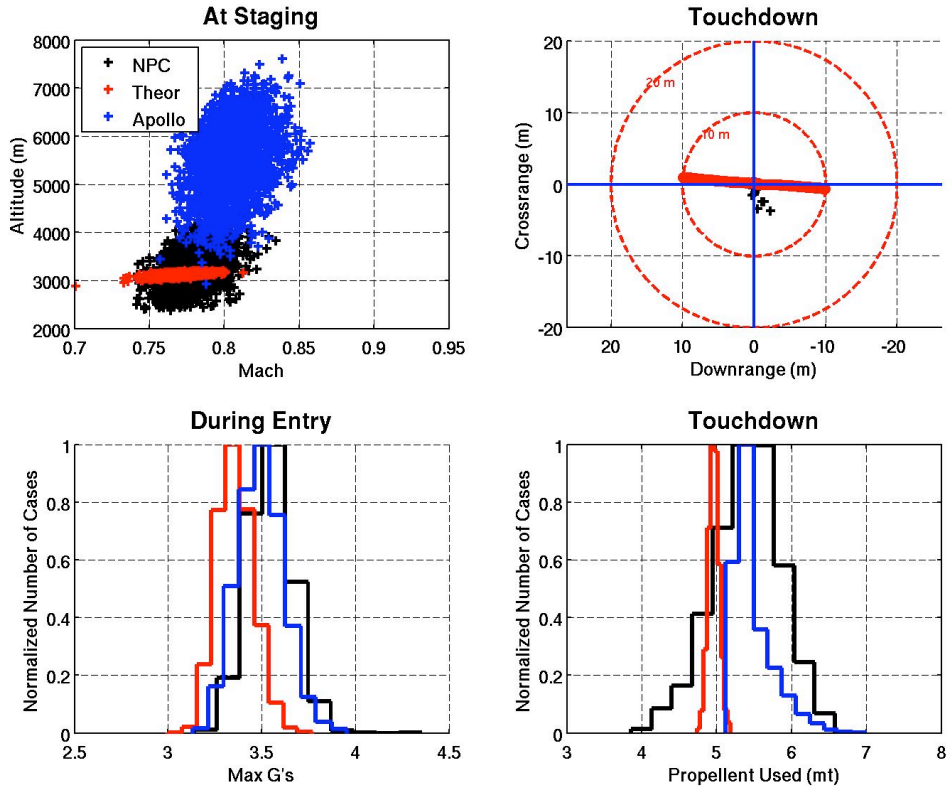


Figure 15. Guidance comparison for Architecture 8.

### 3.4 Retro-propulsion

The primary objectives of the Supersonic RetroPropulsion (SRP) study element for EDL were to provide: (a) Isp and thrust/weight ratio guidance for use in higher-level vehicle parametric modeling and (b) high level system design insight to the team. A literature review, commercial modeling software, and system design experience were used to provide these products. Using the provided system requirements, an assessment of the state-of-the-art for liquid oxygen/liquid methane (LOX/LCH<sub>4</sub>) propulsion, engine throttle range considerations, a notional design including main engine thrust, weight, Isp performance, cycle options, engine configuration, tank sizing and forward work were provided.

For the purposes of the study, DRA5 was the starting point, with the ranges identified in that report limited to a representative point design, as specified by the EDL study lead. Key requirements included a LOX/LCH<sub>4</sub> methane propulsion system. This propellant combination is generally considered space-storable and ISRU (in-situ resource utilization) compatible. Given an initial vehicle combined mass of 62 mT and a 3 g (earth) initial deceleration, 1.8 MN (400,000 lbf) initial thrust is required. Throttle-able for landing, the final thrust is ~10% at shutdown. For sizing purposes, a delta V of 600 m/s was used. Similarly, for the ellipsed vehicle, with 5 deg/s<sup>2</sup> control rates, a smaller RCS thruster of 9kN (2000 lbf) for roll/pitch and a larger RCS thruster of 62kN (14,000 lbf) for yaw are required.

The SOA for LOX/LCH<sub>4</sub> is driven primarily by recent development efforts funded through EDTP. These efforts are primarily geared toward upgrade concepts for the Altair Lunar Ascent Vehicle, although the same technologies would also be useful for a non-toxic, high performance propulsion system for the ORION Service Module, and potentially a Lunar Lander Descent Stage. These efforts are all geared toward relatively low thrust and low delta-V missions, as appropriate for a Lunar Ascent vehicle application. Many of these efforts begin to ramp down in the 2011 timeframe. The total technology effort is ongoing at 6 NASA centers, a dozen contractors in 30 or 40 separate technology development programs. Overall, the TRL could be considered medium for RCS and small Main Engines, and low for large, throttle-able main engines. (Significant engine development efforts include a prototype 22kN/5klbf fixed thrust ascent engine, a 176kN/40klbf breadboard injector with heat sink chamber, a 44kN/10klbf workhorse engine and several 444N/100lbf RCS thrusters delivered). In addition to the EDTP work, numerous studies have been performed on LOX/LCH<sub>4</sub> engines, from 44kN to 900kN. A Korean engine of 90kN is advertised as space qualified, although it has not been flown to date.

Engine throttle range considerations are primarily related to the lower ~50% limit typical of most large pump fed engines. Injector dynamics, pump and turbine design, engine cooling and performance drop-off at low throttle levels limit the practical throttle range for most engines. A recent demo of the CECE LOX/LH<sub>2</sub> achieved 13%, which suggests potential for at least one well-characterized engine. A recent LOX/kerosene Russian engine achieved 30% throttle on the test stand. Pressure fed engines are more amenable to wide throttle range, but are impractical for the large thrust levels needed for the Mars Lander.

Throttle considerations, along with a desire from the vehicle control team to have engines in multiples of three, led to a notional design of 6 engines for further study. Such a cluster could have ½ the engines shutdown at 40-50% throttle, with the balance throttled up to 100% to maintain the descent rate. Then these 3 engines would throttle down to ~20-30% for landing, a reasonable, if optimistic goal for throttle range with many years left to develop such an engine. With ½ the engines operating at low throttle, the desired 10% total thrust at shutdown is thus achieved. An example of the profile settings is provided on the left in Figure 16. Given the DRM sizing constraints, the notional propulsion system design would include 6 engines of 300kN thrust each. Using commercially available engine modeling software, a parametric analysis was performed and a final engine design was chosen that optimized for Isp. Not surprisingly, the high Isp solution of 374s is achieved at the expense of a very high expansion ratio of

180, which drives a very tall nozzle. The figure in the right of Figure 16 illustrates a typical curve of expansion ratio for increasing Isp, albeit for a slightly different mixing ratio. The engine T/W ratio is 60, although several papers and historical precedent suggest that 70 is achievable with adequate development. Further improvements in T/W could be achieved at additional expense, although an optimized engine is well beyond the scope of this study.

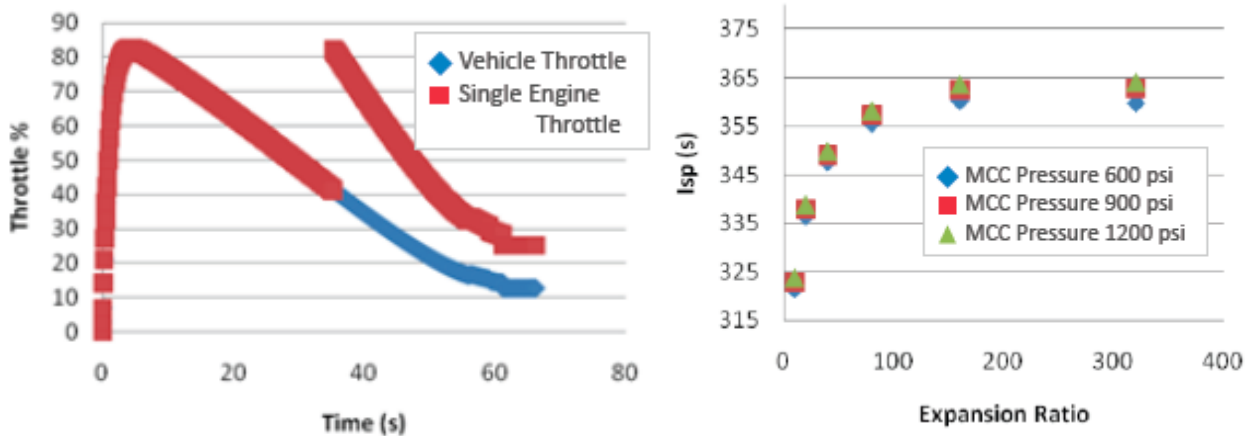


**Figure 16. SRP Sample Throttle Profile (left) and SRP ISP vs Expansion Ratio (right)**

Similar to the propulsion system, a notional design for the propellant tanks is based on the DRA5 sizing of a 62 mT vehicle (with 40 mT payload, 10 mT structure and 12 mT propellant) and the proposed mixture ratio of 3.5. Relative to most lander designs (e.g. all propulsive descent as in Apollo LM), the tanks are rather modest in size, as expected with a modest delta-V requirement and the relatively short burn time of less than 3 minutes. Assuming a common tank diameter of 1.5 m, 9330 kg of LOX would be stored in a pair of 8.2 m<sup>3</sup> tanks, 2.5 m tall. Similarly, 2670 kg of LCH<sub>4</sub> would be stored in a pair of 6.1 m<sup>3</sup> tanks, 2.2 m tall. A notional tank arrangement is shown in Figure 17. Specifics of the tank design are provided in Table 7.

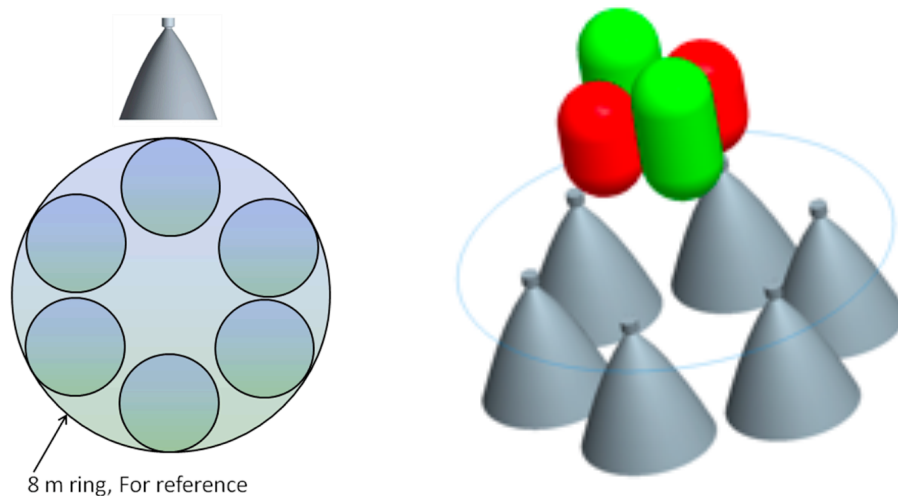


**Figure 17. Notional Tank Arrangement**

**Table 7. SRP Engine Characteristics**

<b>Characteristic</b>	<b>Metric</b>	<b>English</b>
Total Thrust at Initiation	1.8 MN	400,000lb
Engine Thrust	300 kN	67,000 lb
Chamber Pressure	6.2 MPa	900 psia
Engine Height	2.8 m	9.2 ft
Nozzle Height	2.3 m	7.6 ft
Nozzle Exit Diameter	2.5 m	8.2
Engine Mass	550 kg	1210 lbm

Forward work identified in this study may be grouped into engine, tank and vehicle-level considerations. The engine startup in the reverse flow field during Mars entry has two major components: engine startup and nozzle size/stiffness. The startup pressure in the chamber was calculated (by the aerothermal team) at 5.2 kPa (0.75 psia). This pressure is well within our experience base, since sea-level and vacuum starts are both common operations. A much more significant question is the interaction between a large nozzle and the unsteady flow stream around the vehicle at startup, and the dynamic response of the flow stream to mass flow introduced behind the bow shock, along with nozzle stiffness. The relative size of the nozzles is also much larger than has ever been tested in wind tunnels, as is the significant mass flow into the oncoming flow stream. Multiple nozzles interacting both with each other and the environment adds another layer of complexity.

Nozzle issues aside, the development of a large, throttle-able LOX/LCH<sub>4</sub> engine is also required, although some progress has been made on some elements of the engine at both NASA and various contractor facilities (most relevant is the Pratt Whitney 60klb LOX/LCH<sub>4</sub> effort which has performed some study and turbo-pump testing of an upgraded variant of the well-known RL10 engine). Numerous other studies are available in the AIAA and JANNAF databases, although relatively little hardware has been built or tested. One promising concept for reducing engine height is an aerospike solution, although throttling would likely be a challenge with a single large engine. The aerospike concept is generally chosen for its inherently altitude-compensating nozzle-less external flow field, but here the elimination of a large nozzle would be a good fit for the Mars Lander mission.

Propellant tankage forward work should include liner-less composite overwrapped tanks, which have been demonstrated at smaller scale, including a Garvey Aerospace sounding rocket. The elimination of the metal liner may reduce the tank mass up to 50%. The relatively small size of the tanks, relative to the vehicle size, suggests that an integrated tank/structural element solution is unlikely. Transit times with LOX/LCH<sub>4</sub> should be compatible with the Mars mission timeline, since a Ball Aerospace study on a proposed ORION Service Module concept design was capable of 6 months lunar loiter with minimal boil-off losses. Large area MLI and MMOD may be a challenge.

In summary, an Isp range of 365 to 375 seconds appears reasonable, with the higher numbers requiring more development. For conventional nozzles, the upper end of the Isp range will lead to large nozzles, awkward for the Mars Lander, suggesting the practical solution will either be at the lower end of performance or depend on an alternate concept such as an aerospike solution. Similarly a T/W range of 60 to 70 should be realistic, with the higher end requiring more work. No large (300kN) throttleable engine technology is available, although very preliminary work has been performed for a fixed thrust 280kN engine. Most of the current LOX/LCH<sub>4</sub> propulsion development work begins to ramp down in 2011, and the ongoing work is targeted at much smaller systems than the Mars Lander will require. Engine startup and interaction with the unsteady flowfield behind the vehicle bow shock will require significant CFD analysis, wind tunnel testing and subscale flight tests, e.g. sounding rocket experiments. Vehicle drag, flutter and stiffness will interact and should be considered a significant development area.

Propellant tank size is rather modest due to the modest delta-V requirements, but tank, MLI and MMOD weight are significant contributors to vehicle mass.

### 3.5 Thermal Protection Systems

Estimated thermal response models were used in the sizing analysis of the thermal protection systems (TPS) needed for the HIADs and rigid mid-L/D aeroshells. For both aeroshells the sizing was performed on a dual heat pulse mission (aerocapture, cool down in orbit and out-of orbit entry). The sizing analysis is based on the tools and practices developed by the Orion TPS ADP. The TPS sizing tool (which makes use of the ablative thermal analysis tool FIAT [25]) was extended for EDL-SA to include the capability to size dual layer TPS. The margins applied to TPS masses are documented in [26] and summarized in Table 8. The margins were developed based on the Orion TPS ADP experience. (Note that the rigid mid-L/D aeroshell analysis was run before the margin document was finalized so those analyses used the Orion values for initial temperature and recession uncertainty.)

**Table 8. TPS Sizing Margins**

Parameter	Value
Initial Temperature	10°F (Rigid Aeroshell 70°F)
Radiation Sink Temperature	70°F
Allowable Bondline Temperature	550°F
Blowing Factor	0.4
Ablator Fail Lien	50%
Thermal Margin	108°F
Gap Heating Factor	1.0
Recession Uncertainty, Default FOS	1.3, 1.1 (Rigid Aeroshell 1.2)

#### 3.5.1 HIAD – 23 m diameter

**TPS Material Properties and Stack** – Currently no flexible ablative material exists that meets the estimated HIAD requirements. For this study, estimates for possible properties of a flexible Silica/Silicone ablator were created and used in the TPS sizer. The properties were based on SIRCA-15 (15 lb/ft<sup>3</sup>) with some modifications. The virgin density reduced to 10 lb/ft<sup>3</sup> and the char density was assumed to be 8 lb/ft<sup>3</sup>. The thermal conductivity was taken to be 80% of the SIRCA-15 conductivity. The Silicone decomposition and virgin and char emissivities were kept the same as SIRCA-15. The material stack up used for HIAD is shown in Figure 18. For these analyses a conservative assumption of no structure or thermal mass was used.

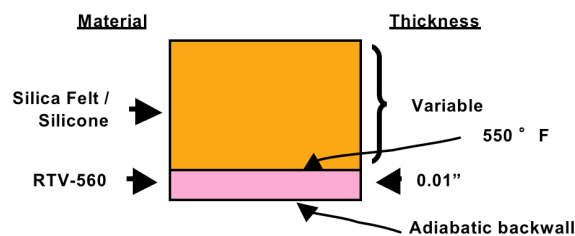


**Figure 18. HIAD Material Stack**

**Aerothermal Environment** – The HIAD dual pulse environment for aerocapture and entry is shown in Figure 19. The plot on the left shows maximum total heating for the nominal aerocapture in red and the 80 metric ton entry in blue. (The curves are plotted one after the other for visualization, but in reality there is a long on-orbit cooling period between them.) The integrated heatload contour is shown on the right. Fully margined analysis estimates that the 23 m HIAD experiences around 100 W/cm<sup>2</sup> during aerocapture and 30 W/cm<sup>2</sup> during entry.

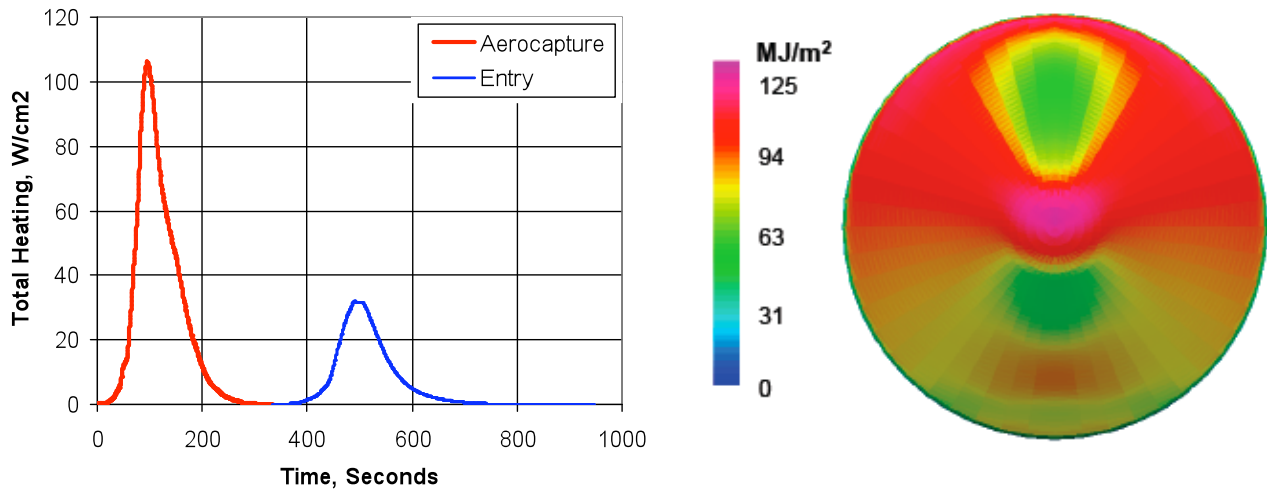


**Figure 19. HIAD Dual Pulse Surface Heating History and Integrated Heatload Contour (Fully Margined)**

**TPS Analysis Results** – The computed mass for a bond line temperature of 550<sup>0</sup>F was predicted to be 3.2 mt, including the RTV (Room Temperature Vulcanized bonding agent) attachment mass and not including WGA. These mass calculations are employed in the EDL-SA HIAD mass estimating relationships (MERs). Some bondline temperature sensitivity studies were run which showed a 12% increase in the TPS mass if the allowable bondline temperature were reduced to 250<sup>0</sup>C (482<sup>0</sup>F).

### 3.5.2 Mid L/D Aeroshell

**Background** – For DRA 5, TPS masses for a forebody heat shield made of a single material (PICA) were very large. The DRA 5 TPS subteam conceived a dual-layer TPS with the PICA ablator atop a low thermal conductivity substrate such as the Shuttle tile material or SLA 561. Individually, these TPS materials are at a high TRL, but a dual layer TPS system made of these materials has never been evaluated or tested. Using existing thermal response models for PICA and LI-900, preliminary hand analysis of the dual layer concept at three body points indicated that the concept could reduce TPS masses by about 27%, not accounting for attachments.

This updated analysis used the new sizing code to do entire body dual layer TPS sizing. The concept for PICA atop the LI-900 Shuttle tile material is shown to be capable of reducing the windward TPS mass by 37%, not accounting for TPS attachments or weight-growth allowance.

**TPS Material Stack and Analysis Methodology** – The TPS material stack used for the mid L/D aeroshell analysis is shown in Figure 20. The tile was attached to the substructure with a standard RTV/SIP configuration. The analysis substructure was a titanium plate and represents the thermal mass of typical aeroshell thermal masses. The ablator was modeled directly above the tile. No adhesive or attachment between the ablator and tile was modeled. This was considered to be sufficiently conservative for this analysis cycle.

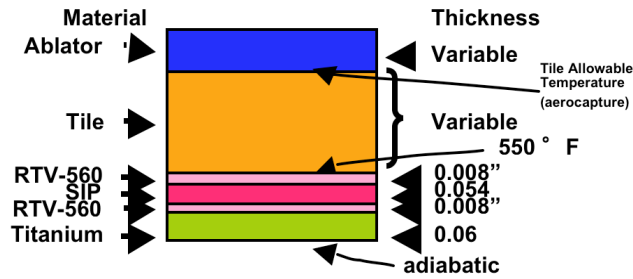


Figure 20. Mid L/D Aeroshell TPS Stack

The material splitlines for the mid L/D vehicle are determined by the maximum temperature seen at each location during aerocapture and entry. They are shown in Figure 21. The leeward sections are tile only and were sized by a transient run that included both aerocapture and entry with a long on-orbit cool off between. For the windward dual layer sections, it is assumed that the on-orbit cool off between the aerocapture and entry phases is sufficiently long enough for the TPS system to cool completely to the initial temperature. It is also assumed that the ablator is needed to protect the tile during aerocapture, but is not needed during entry. So for the windward dual layer TPS analyses, the aerocapture and entry phases was separated and run in two steps. For the first step, the ablator was removed from the model and the tile layer was sized to survive the entry environment while maintaining the allowable bondline temperature at the tile/RTV interface. For the second step, the ablator was reattached to the model. The ablator was then sized to maintain the tile allowable surface temperature at the ablator/tile interface (as well as the allowable bondline temperature at the tile/RTV interface) during aerocapture.

Note, that the above described analysis method assumes that ablator is needed to protect the tiles in a dual-layer stack during the aerocapture phase only. However, the validation testing of the dual heat pulse, dual layer concept presented in Section 7.1 below shows some slumping of the LI-900 at the peak entry heating rates once the PICA has ablated away. Therefore, future analysis should consider leaving a thin amount of ablator (or char) at the end of aerocapture to protect the tile during entry at the highest heat flux areas of the windward dual-layer section.

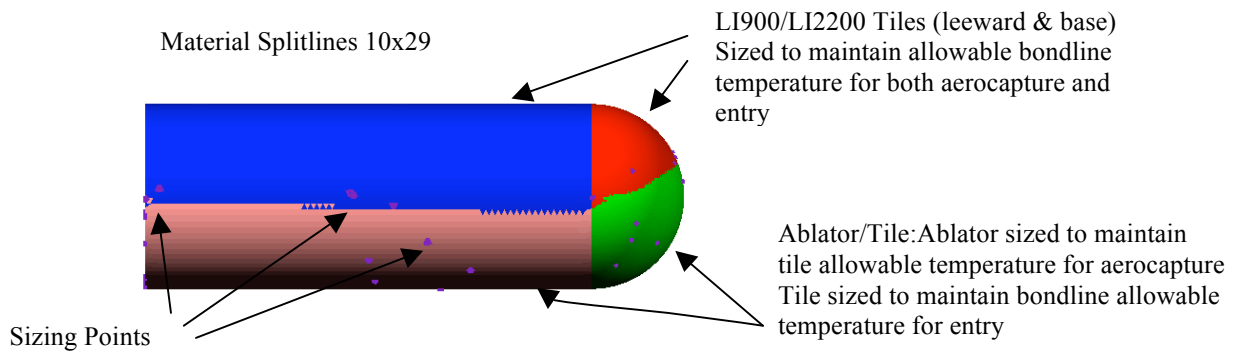
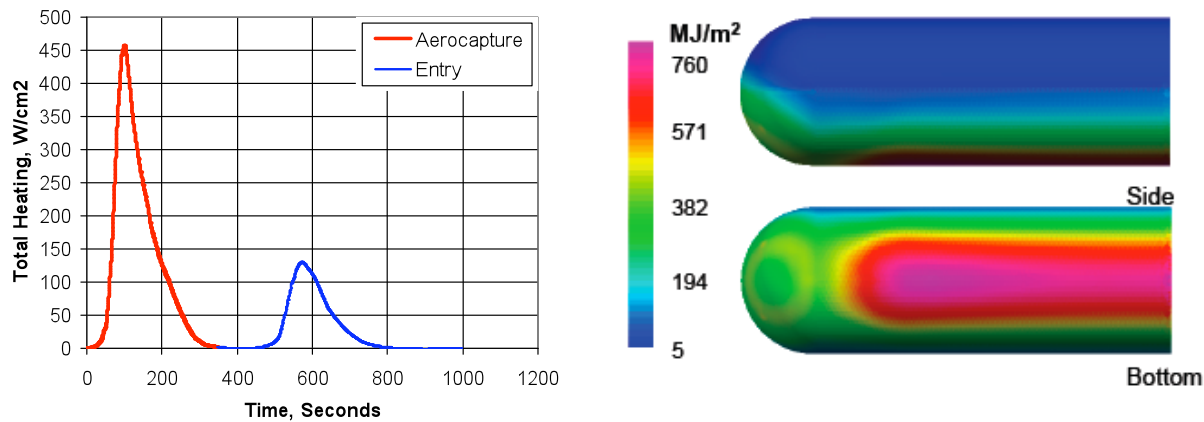


Figure 21. Mid L/D Aeroshell Material Splitlines

**Aerothermal Environment** – The mid L/D aeroshell dual pulse environment for aerocapture and entry is shown in Figure 22. The plot on the left shows maximum total heating for the aerocapture in red and the entry in blue. (The curves are plotted one after the other for visualization, but in reality there is a long on-orbit cooling period between them.) The integrated heatload contour is shown on the right. Fully

margined analysis estimates that the mid L/D aeroshell sees around 450 W/cm<sup>2</sup> during aerocapture and 120 W/cm<sup>2</sup> during entry.



**Figure 22. Mid L/D Aeroshell Dual Pulse Surface Heating History and Integrated Heatload Contour (Fully Margined)**

*TPS Analysis Results Not Including Attachments* – Results for the mid L/D aeroshell TPS sizing analysis are shown in Table 9. Analyses were run for the ablator PICA over two different tiles, LI-2200 and LI-900. For comparison, a case was also run with PICA only on the windward surface of the vehicle. The results show that if the lightweight LI900 tile is used with PICA, there is an estimated TPS mass savings over the whole vehicle of 34%. These estimates do not include masses for the attachment of the ablator to the tile or for any structure to hold the TPS.

**Table 9. Mid L/D Aeroshell TPS Mass Estimates (Not including attachment or WGA)**

Windward TPS	PICA Only Mass, kg	Dual Layer PICA/LI-2200 Mass, kg	Dual Layer PICA/LI-900 Mass, kg	Savings	Savings
Nose Windward	1670	1350	1000	19%	40%
Body Windward	8750	7020	5580	20%	36%
<b>TOTAL Vehicle TPS*</b>	<b>11260</b>	<b>9210</b>	<b>7420</b>	<b>18%</b>	<b>34%</b>

\*Includes Leeward Tiles

*Estimates for Attachment Weights* – Estimates for TPS system attachment weights were performed and are shown in Table 10. Two attachment methods were considered, a shuttle like tile system with 25.4 cm square tiles and a honeycomb system with 5 cm blocks bonded into a honeycomb, which was bonded to the substructure. The 5 cm honeycomb system estimates were made by scaling measured masses from Applied Research Associates, ARA [27] for 5 cm thick PICA blocks in phenolic impregnated silica fabric honeycomb with RTV on 5 sides of the PICA blocks. (Note, the “TPS Mass” column differs slightly from the total values in Table 9 because mass was removed for the gaps and the volume calculations were updated to account for the curvature of the vehicle). The shuttle like tile systems are considered to be unrealistic for manufacturing of the dual layer system, so method 2 was discounted. However, method 3 (5 cm blocks in honeycomb) using PICA over LI900 tiles still shows a 24% mass savings over PICA alone (method 1). The mass calculations for method 3 are employed in the EDL-SA mid L/D mass estimating relationships (MERs).

**Table 10. Mid L/D Aeroshell, Windward Side Estimated Masses with Attachment**

TPS	Attachment Method	TPS Mass, kg	Attachment Mass, kg	Total Mass, kg	Comments
1	PICA Only Shuttle like Tile System 25.4 cm tiles 0.07 RTV gap filler RTV/SIP/RTV to structure	10,600	1,100	11,700	Note*
2	PICA/LI-900 Shuttle like tiles 25.4 cm tiles 0.07 RTV gap filler RTV/SIP/RTV to structure	6,700	900	7,600	Un-bonded PICA on LI-900 Unrealistic from Manufacturing Consideration Feasibility demonstrated at coupon level.
3	PICA/LI-900 5 cm HC System HT424 HC to structure RTV blocks to HC RTV blocks to structure	6,500	2,900	9,400	23% heavier than method 2, but 24 % lighter than PICA only

\* Orion considered the PICA (#1) option for use with a titanium honeycomb carrier structure system but chose an Avcoat option instead based on overall system level risk and reliability. MSL used a system of PICA tiles direct-bonded to a composite substructure with RTV filled gaps. PICA tiled system selection, while accepted for MSL and not for CEV Orion, is based on system level integration issues and reliability requirements. Any tiled system for human mission design will have to overcome concerns similar to the ones considered by Orion.

**Conclusion** – The TPS sizing results presented here, along with the validation testing of the dual heat pulse, dual layer concept presented in section 7.1 below, demonstrate the credibility of providing the TPS for the 10x29 meter Mid L/D aeroshell (ellipsled) for future human Mars missions. The use of a 5 cm honeycomb for the windward TPS installation appears to enable the manufacture of the large heat shield.

The thermal performance of the PICA atop LI-900 TPS installed with the honeycomb is shown to be predictable for the dual heat pulse environment. The dual layer TPS concept, including attachments, provides significant mass savings compared to a PICA-only solution. Three caveats are made here: (1) As shown in work by the Orion TPS ADP, PICA recession at heat rates below 50 W/cm<sup>2</sup> is not well predicted by FIAT, owing to out-of equilibrium gas-solid interactions within the material at those conditions. As with Orion, the low heating conditions will be experienced by the mid L/D aeroshell at the “tails” of the two flight heat pulses. (2) Four-point positive and negative flexural tests of PICA atop LI-900 in ~ 5 cm honeycomb showed encouraging results for test articles fabricated on an aluminum substrate. However, further development on the bonding of the honeycomb to realistic composite substrates has not been performed to date. (3) The “fencing” caused by non-uniform ablation of the honeycomb and PICA at low heat fluxes may be an issue and requires testing and refinement of the phenolic impregnated fiberglass honeycomb technology.

## 4 Simulation Results

The simulation used to evaluate the EDL-SA architectures is the Program to Optimize Simulated Trajectories (POST2) [28], which is a generalized point mass, discrete parameter targeting and optimization simulation. POST2 has the capability to target and optimize multiple vehicles near a rotating oblate planet and has extensive heritage for simulating ascent, descent, and orbiting trajectories including past missions like Shuttle, Genesis, Stardust, Genesis, and Mars Missions including, Pathfinder, Odyssey Orbiter, Exploration Rovers, Reconnaissance Orbiter, and the Phoenix Lander. POST2 is also used extensively in current missions like Mars Science Laboratory, Launch Abort Systems and Ares.

Specific models used to tailor production POST2 for the EDL-SA purposes include use of the Mars Global Reference Atmosphere Model 2005 (MarsGRAM) [29], a standard accepted throughout the field. The entry date was arbitrarily chosen to be November 3, 2010 (a MSL derivative). The atmosphere entry altitude is approximately 125 km. The planet model included a gravitational constant equal to  $4.2828376383e13 \text{ kg}\cdot\text{m}^2/\text{s}^2$  with a mean equatorial radius equal to 3396190 m, a mean polar radius of 3376200 m and a planet rotation rate of  $7.088218e-5 \text{ rad/sec}$ . The gravity model included a JPL Mars 85x85 model truncated at  $20\times 20$ . The terrain model used  $1/32^{\text{nd}}$  deg Mars Orbiter Laser Altimeter (MOLA) data.

Other EDL-SA simulation specific models, described in previous sections, include aerodynamic and aerothermodynamic models for the HIAD, SIAD and Rigid Aeroshell (Section 3.2) and tension cone based on a previous CEMENT study; mass properties, derived from response surface equations for HIAD, SIAD and Rigid Aeroshell (Section 3.1); a propulsion model (Section 3.4); various guidance routines of varying fidelity tailored for specific flight scenarios (Section 3.3). In addition EDL-SA assumes that the trajectories have perfect Navigation knowledge and that technologies required to perform precise landings will be leveraged from ALHAT.

The purpose of the first year of the EDL SA was to examine alternative architectures that would provide the aerocapture phase required by DRA5 for the cargo delivery vehicles and the EDL required by both the cargo and crewed vehicles. The approach velocity and target orbit were provided by DRA5. To summarize: 1) the hyperbolic approach velocity was set at 7.36 km/s; 2) the target orbit was a 1Sol (33793km x 250 km); 3) EDL initiates from the 1 Sol orbit; 4) the landing site is at 0 m altitude; 5) the touchdown provides 10 m accuracy; and 6) the deceleration profiles remain within those limits set for a deconditioned crew. It was assumed for all the architectures that a reaction control system (RCS) would be the primary control. To emulate the characteristics of a RCS without having to design a control system, a “pseudo-controller” was used where the bank acceleration, maximum bank rate, and bank direction are modeled.

The simulation was used for both the aerocapture and entry, descent and landing analysis. Details of nominal reference trajectories, sensitivity studies and Monte Carlo analysis results are presented in this section.

### 4.1 Aerocapture Simulation Results

The purpose of aerocapture is to use atmospheric drag to slow the vehicle from a hyperbolic velocity relative to the planet into an elliptical orbit. Figure 23 shows the aerocapture trajectory and major events. The aerocapture phase (events numbered 2-8) is followed by a periapsis raise burn (9), then a (nominally zero) cleanup burn (10) which place the vehicle into the desired post-aerocapture target orbit. Following a period of time in orbit, a de-orbit burn is performed in order to establish the desired atmospheric interface to initiate the EDL phase, which culminates with touchdown on the Martian surface.

The eight combinations of architectures selected contain three different aerocapture scenarios. The first is a mid-L/D rigid aeroshell. The second is a 23 m diameter inflatable aeroshell (HIAD). The third configuration is a large HIAD (~55 m), sized to achieve a peak heat rate of  $50 \text{ W/cm}^2$  ( $3\text{-}\sigma$ ). The decision process for the sizing of the 55 m HIAD is discussed in detail in 4.1.5, in the discussion of the Breakpoint Study.

For consistency in the mass modeling, a  $\Delta V$  budget is allocated for aerocapture not to exceed 150 m/s. Also, based on historical practice and to ensure robust Monte Carlo analysis, the skip-out margin, defined as the difference between the flight path angle flown for the pass and the flight path angle, which results in a flyby, is required to be greater than 1 deg. Peak acceleration results are compared to the Human-Systems Integration Requirements (HSIR) [30] limits and checked to ensure that no exceedances have been observed.

Section 3.3.1 describes the HYPAS guidance used to determine the aerocapture trajectories.

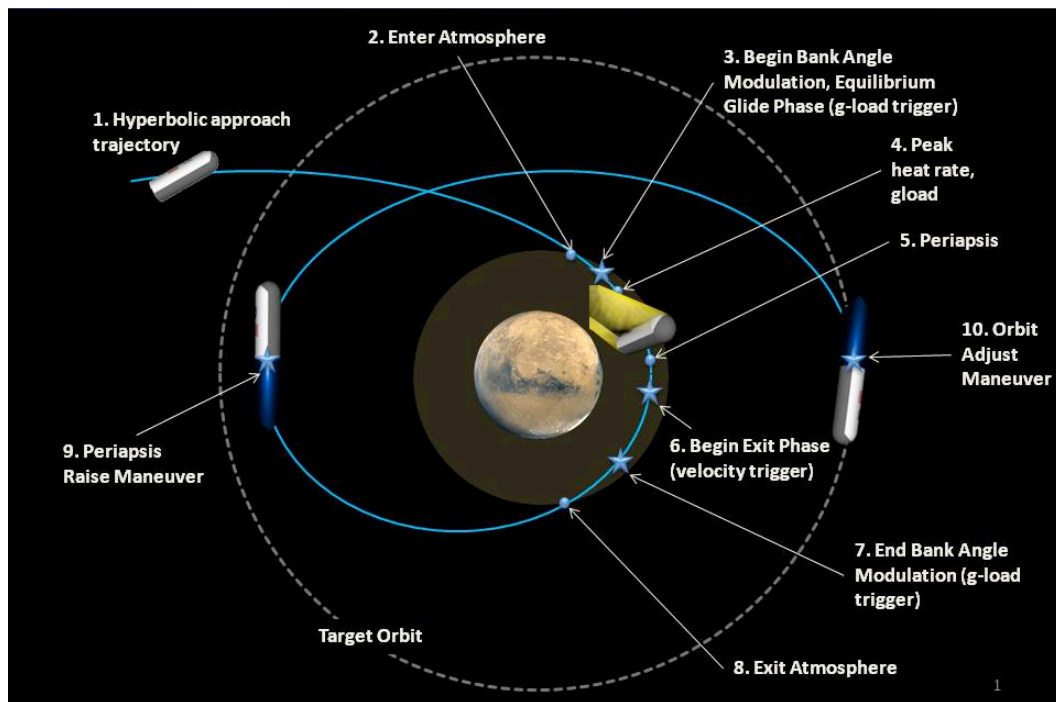


Figure 23. Aerocapture Phases

#### 4.1.1 Aerocapture Flight Path Corridor Sizing

Initially, the theoretical lift up-lift down profile was flown, in place of HYPAS, to gain an understanding of the expected performance for the three aeroshell designs. Values of skip-out margin can be obtained from studying these results. Skip-out margin is the difference between the flight path angle flown for an individual case and the flight path angle that causes skip-out. Figure 24 shows the amount of available skip-out margin for a range of ballistic numbers and L/D values. The flight path angle is chosen such that the maximum g-load is 4-Earth g's. The figure also highlights the three aeroshell designs studies in this analysis according to each design's L/D and ballistic number combination and the amount of skip-out margin available for each design. Historically, a skip-out margin of 1 degree is required to see good performance (i.e. no cases lost to skip-out) in the Monte Carlo runs. The 23 m diameter inflatable aeroshell has 1.25 degrees, the 55 m diameter inflatable aeroshell has roughly 0.9 degrees, and the rigid aeroshell has approximately 1.6 degrees. Therefore, good performance is expected from Monte Carlo analysis for all configurations excluding the 55 m diameter inflatable aeroshell.

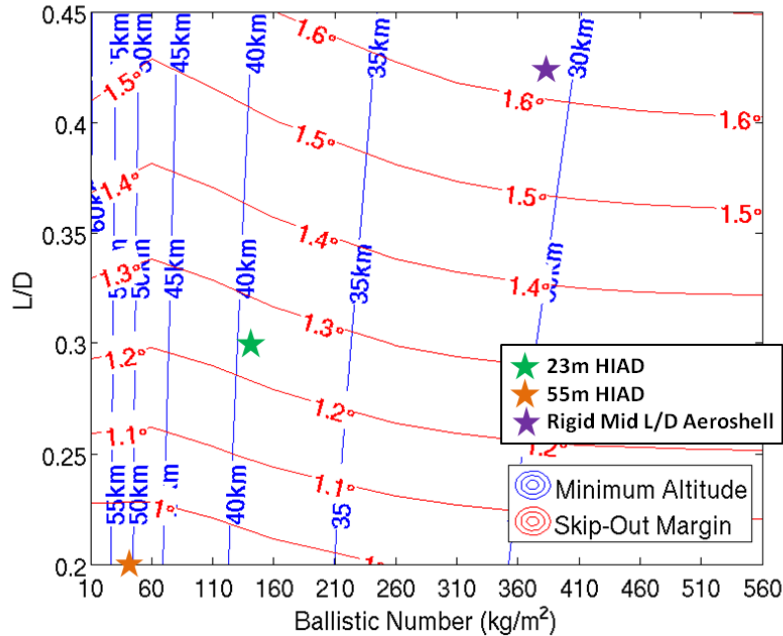


Figure 24. Available Skip-out Margin for Variations of L/D and Ballistic Number

#### 4.1.2 Nominal Trajectory Results

Reference trajectories were developed for the three different aeroshells using a 1 Sol (33793 km x 250 km) post-aerocapture target orbit. For each of these references, the HYPAS analytical closed-loop guidance algorithm was used to generate the trajectories.

The simulation inputs include using the MarsGRAM 2005 atmosphere and the aerodynamic model described in Section 3.2.3. Additionally, an entry velocity of 7.36 km/s was selected, and the flight path angle at entry interface was chosen to meet the desired peak g-load for each case. Figure 25 compares the altitude profiles for each of the three configurations studied, and shows that the minimum altitude decreases as the ballistic number increases. The 55 m HIAD has the lowest ballistic number, and reaches a minimum altitude just below 50 km. Conversely, the rigid aeroshell is the highest ballistic number and reaches a minimum altitude of slightly higher than 30 km.

Figure 26 and Figure 27 show the key trajectory guidance parameters for the 23 m HIAD nominal trajectory. These parameters include bank, drag acceleration, and altitude rate profiles. The bank profile, which the guidance algorithm commands in order to fly the drag acceleration and altitude rate profile reference trajectory, shows good performance in that the bank is consistently being modulated and does not saturate the guidance by holding full lift up (0 degrees) or full lift down (180 degrees) during the guided portion of the maneuver. Additionally, the drag acceleration and altitude rate profiles follow their reference profiles as expected. The drag acceleration profile is trying to pull the vehicle deeper into the atmosphere in order to avoid skip-out, whereas the altitude rate profile is attempting to maintain the equilibrium glide condition of constantly increasing altitude. However, the actual trajectory does not match the reference profiles exactly, as each profile is attempting to achieve competing objectives. Similar nominal trajectory data was generated for the 55 m HIAD and rigid aeroshell cases. All of these nominal trajectories were designed to a maximum of 3-Earth g's.

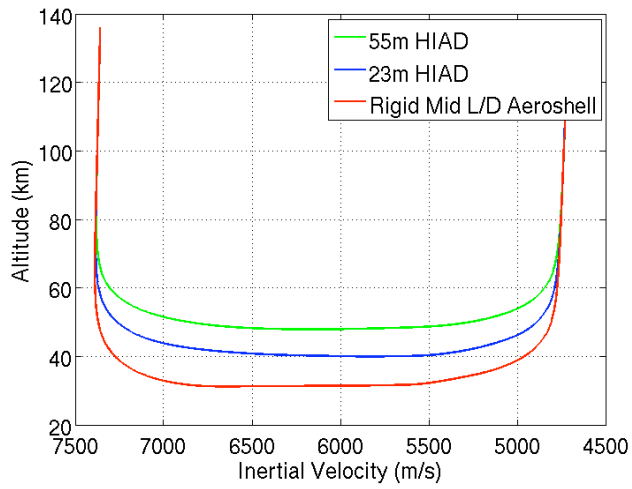


**Figure 25. Altitude Profiles for All Configurations**

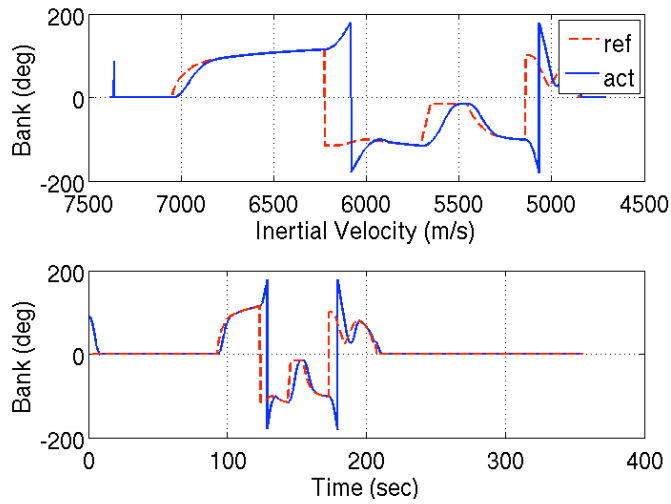


**Figure 26. Nominal Bank Profiles for the 23 m HIAD**

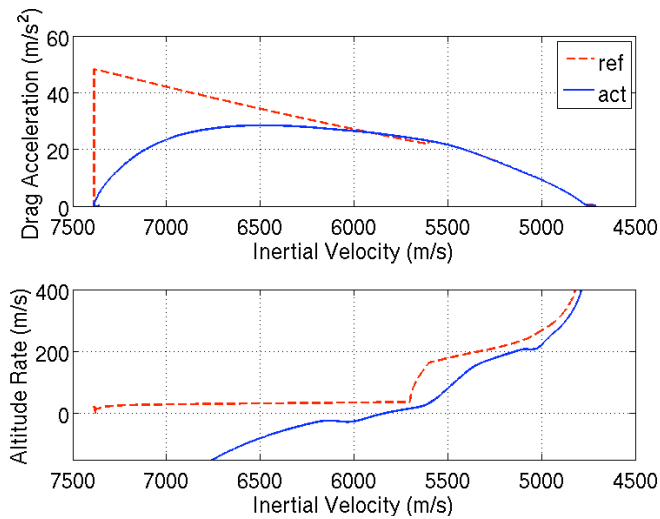


**Figure 27. Nominal Drag Acceleration and Attitude Rate Profile for 23 m HIAD**

### 4.1.3 Monte Carlo Results

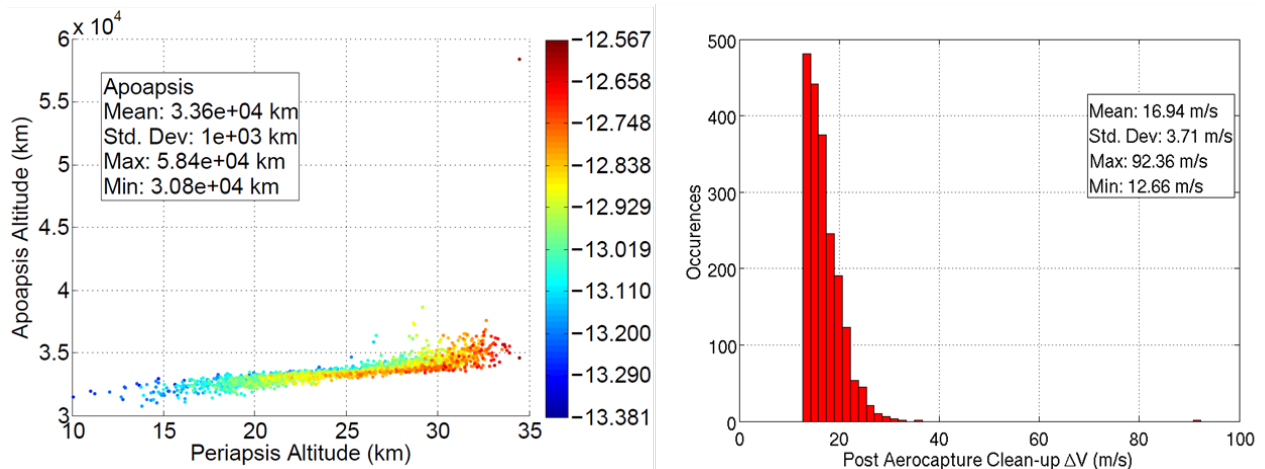
Sets of 2000 case Monte Carlo runs were completed for each of the reference profiles, and the HYPAS gains were optimized for  $\Delta V$  performance within each set. The applied dispersions are listed in Table 11.

**Table 11. Aerocapture Monte Carlo Dispersion Values**

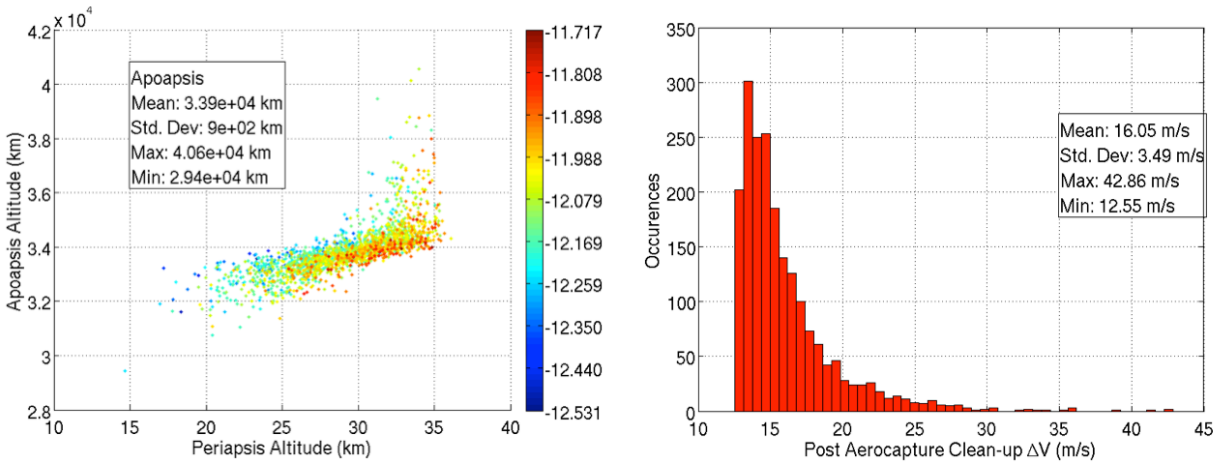
Dispersion	Value
Aerodynamic	+/- 10% (normal, $3\sigma$ )
Angle of Attack	+/- 5% (normal, $3\sigma$ )
Entry Flight Path Angle (EFPA)	+/- 0.35 deg (normal, $3\sigma$ )
Dust Tau	0.1:0.9 + random density perturbations
Mass	+/- 5% (normal, $3\sigma$ )

Figure 28 through Figure 30 show key Monte Carlo results for each of the three aeroshell designs considered in this study. The figures are shown in order of decreasing ballistic number and L/D, with the rigid mid-L/D aeroshell having the highest combination of the two, and the 55 m HIAD having the lowest. With the exception of one extraneous high point in the Rigid Mid L/D Monte Carlo results, it is observed that, as ballistic number and L/D decreases, the range of apoapse altitude reached and the amount of  $\Delta V$  required to perform the post aerocapture clean up burn increases. There is a direct correlation between the size of the apoapse altitude target miss distance and the amount of  $\Delta V$  required to clean up that miss distance. The larger the miss distance, the larger the clean up burn must be to put the vehicle into the target 1 sol orbit.

The single high apoapse altitude observed in the rigid aeroshell is due to poor tuning in the guidance gains. With improved guidance tuning, the maximum  $\Delta V$  value for that design could be brought below the maximum  $\Delta V$  observed in the 23 m HIAD and 55 m HIAD cases which are well tuned and the performance observed is ideal.



**Figure 28. Monte Carlo Results for the Rigid Mid L/D Aeroshell**



**Figure 29 Monte Carlo Results for the 23 m HIAD, L/D = 0.3**

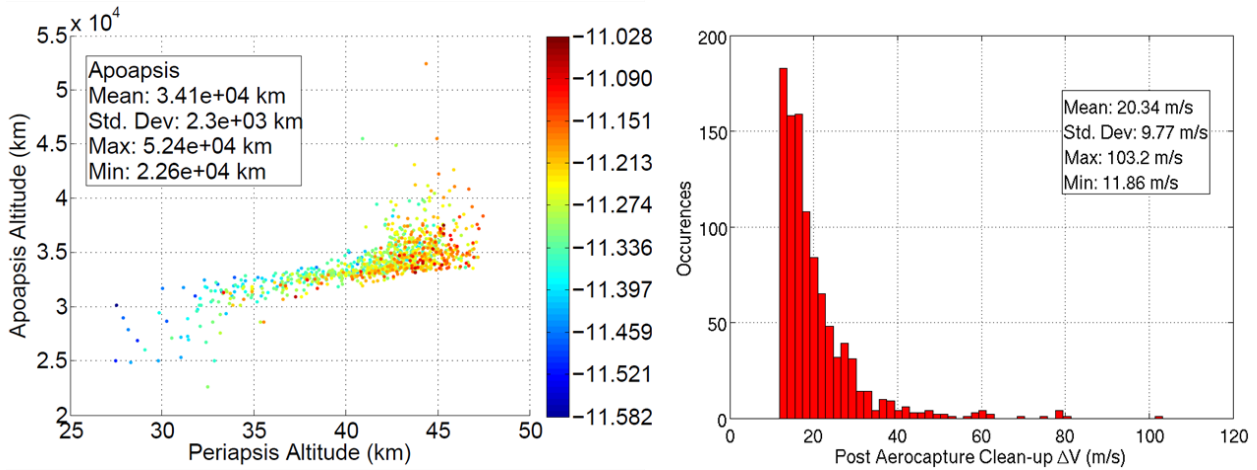


**Figure 30. Monte Carlo Results for the 55 m HIAD, L/D = 0.2**

The trend in larger apoapse altitude and higher  $\Delta V$  values for the rigid aeroshell and the 55 m HIAD can be attributed to a decrease in L/D value. As stated previously, the larger the apoapse altitude, the larger the clean-up burn. The lower the L/D, the less lift the vehicle is able to command throughout the guided portion, which increases the difficulty the guidance has to achieve the target altitude rate profile. This, coupled with the worst of the Monte Carlo dispersions, creates individual cases in which the guidance, commanding the maximum amount of lift, is still unable to meet the altitude rate targets and exits the atmosphere with a large apoapsis altitude error. Though less than ideal performance is observed in Figure 10 for the L/D=0.2 case, the required  $\Delta V$  is still below the budgeted 150 m/s, therefore, the performance has been deemed acceptable.

#### 4.1.4 Sensitivity Study Results

Several sensitivity studies were also performed to evaluate the effect of additional parameter changes on the post aerocapture clean up  $\Delta V$ . Nominal trajectories were simulated that parametrically varied atmosphere inputs such as season, dust opacity, and time of day over the full or expected range, as well as the initial mass and target orbit. Gain scaling (but not tuning) was performed for the mass sensitivity

cases, and no gain changes were made for the atmosphere sensitivities. An examination of the results of atmosphere and mass sensitivities resulted in no significant variation (less than 8 m/s) or trends in variation of  $\Delta V$  primarily because of vehicle velocity and the fact that the guidance is capable of flying out the variations. That was not the case for the sensitivity study that considered various target orbits.

The choice of target orbit, or post aerocapture apoapsis altitude (ranging from 33,793 km to 500 km) was determined to have a significant effect on the  $\Delta V$  required for the post-aerocapture cleanup maneuver. Figure 31 shows the cleanup  $\Delta V$  that results from the sensitivity that compared the aerocapture of a 23 m HIAD vehicle into both a 1 sol and 500 km circular post-aerocapture target orbit. A significant difference in mean  $\Delta V$ , roughly 100 m/s, is observed.

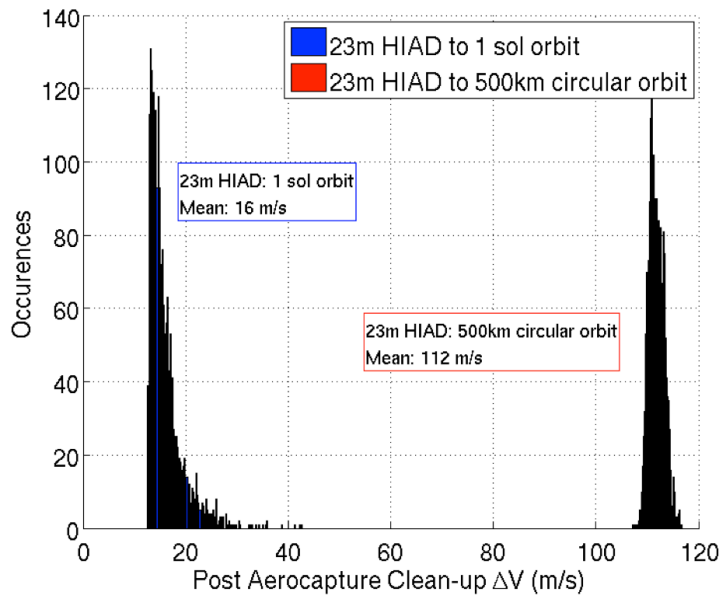


**Figure 31. Delta V Sensitivity to Post-Aerocapture Orbit**

#### 4.1.5 Trades

**Breakpoint Study** – Architecture 2 assumes a 23 m HIAD, and due to the heat rate results from the aerocapture and entry simulations, the HIAD required heavy ablator TPS material. At the External Peer Review a request was made to examine the lower limits in L/D and ballistic coefficient that would enable the HIAD to maintain heat rates less than  $50 \text{ W/cm}^2$  thus possibly requiring a lighter insulating-only TPS. Since the higher heat rates are seen during aerocapture, a study was initiated to determine the aerocapture HIAD performance “break point.”

The range of L/D considered for the study was 0.1 to 0.3, and ballistic numbers ranged from 25 to  $50 \text{ kg/m}^2$ . Sixteen specific combinations of L/D and ballistic numbers were considered for a scaled MIAS shape inflatable aeroshell configuration that aerocaptured into a 1sol orbit. Results show that performance is highly sensitive to L/D, and that poor performance is observed for L/D’s less than 0.25.

Revisiting the concept of skip-out margin and understanding the amount available for each combination can provide insight into aerocapture performance. Figure 32 shows the skip-out margin available for the 16 combinations considered. The plot shows that for L/D values less than 0.25, the amount of skip-out margin is less than the one-degree required to obtain sufficient performance.

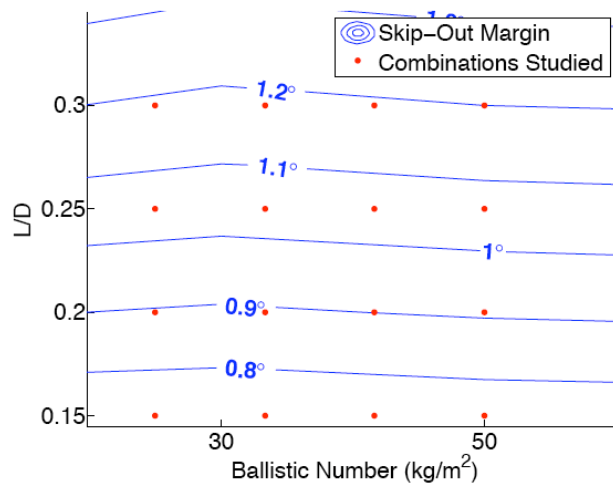


Figure 32. Available Skip-out Margin for Low Combinations of L/D and Ballistic Number

Using well-tuned guidance gains for a high L/D and ballistic number combination, the gains were scaled down and a 2000 case Monte Carlo simulation was performed for each of the sixteen combinations.

Figure Figure 33 shows post aerocapture  $\Delta V$  range required to target the 1 sol orbit for each of the combinations.

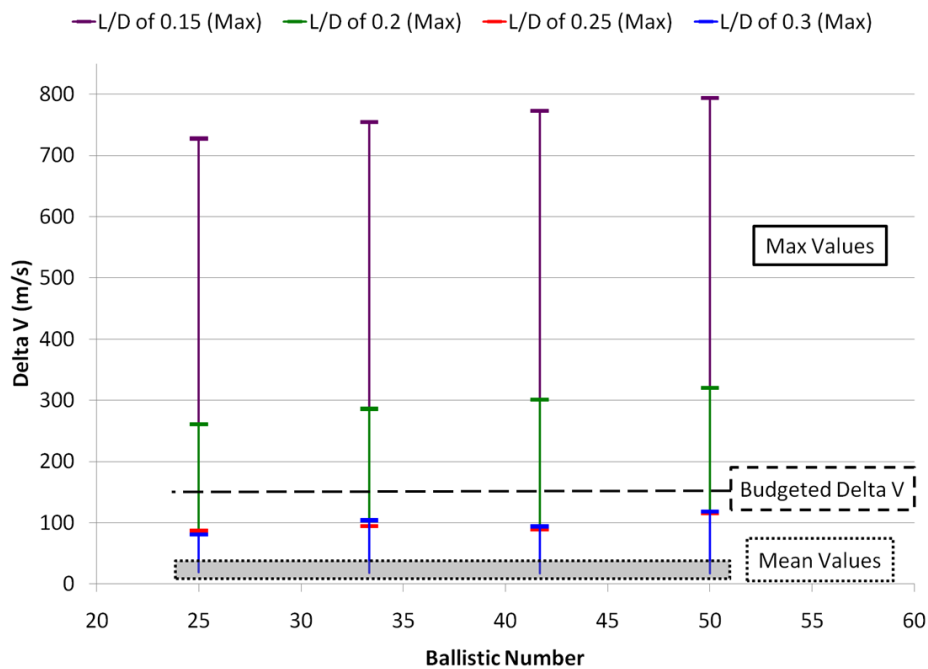


Figure 33. Delta V Monte Carlo Results

The key parameter to note is the maximum  $\Delta V$  value required to clean up large apoapsis miss distance for each value of L/D. A large miss in apoapsis altitude requires a corresponding large amount of

$\Delta V$  to clean up the orbit. Validating known poor performance at low skip out margins, the  $L/D=0.15$  data has several cases that require more than 700 m/s of clean up  $\Delta V$ , significantly exceeding the budgeted amount of 150 m/s. Even for a  $L/D=0.2$ , 300 m/s of  $\Delta V$  is required, exceeding the budgeted amount, while the cases with  $L/D=0.25$  and  $L/D=0.3$  show acceptable performance.

Figure 34 shows the relationship between the Monte Carlo 3-sigma peak heat rate values and HIAD diameter. Each line represents a different value of  $L/D$ , which is shown to have a relatively small effect on the peak heat rate. The data also show that the choice of HIAD diameter (or the effect of ballistic coefficient) has a significant effect on the peak heat rate.

Initial mass and aerodynamic models limited the HIAD diameter to 50 m. The breakpoint study considered whether holding to a 3-sigma peak heat rate of less than 50  $W/cm^2$  would enable use of the same models by maintaining diameters below 50 m. Based on results shown in Figure 34, it is clear that no combination of ballistic number and  $L/D$  considered for the break point study is sufficient to meet both the peak heat rate and diameter constraints. Meeting the heating constraint was considered more important than meeting the diameter constraint; therefore, the HIAD diameter was allowed to increase to 55 m.

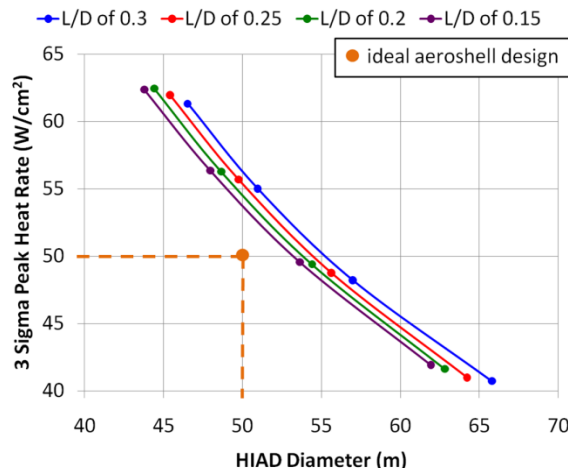


Figure 34. Plot of 3 sigma peak heat rate versus diameter for lines of constant  $L/D$

The previous data include dispersed results for a scaled, but un-tuned set of guidance gains. The next step in characterizing the breakpoint was to choose a breakpoint set of cases for which to tune gains to examine improvements in performance. Gain tuning is a labor intense process, so only 4 of the 16 cases were selected for tuning. By examining Figure 30 combinations with a  $L/D$  lower than 0.2 exceeded the  $\Delta V$  budget, therefore  $L/D = 0.2$  was established as the  $L/D$  breakpoint. Additionally, Figure 34 shows that HIAD diameters in the 50 to 55 m range come closest to satisfying heat rate constraint, therefore corresponding ballistic numbers of 41.67 and 33.33  $kg/m^2$  established the ballistic number breakpoint. Therefore, the two  $L/D$  and ballistic number breakpoints were combined to form the four combinations to be optimized using guidance gain tuning.

The attempt to improve performance by tuning guidance gains was also improved by making a change in assumed entry flight path angle dispersion in the Monte Carlo. The previous Monte Carlo analysis had included a 0.35 deg variation in entry flight path angle. However it was felt that a reduction in the dispersion to 0.25 deg was acceptable and achievable by the time of the actual aerocapture flights. The results of these modification for the optimized  $L/D = 0.2$ , ballistic number of 33.33  $kg/m^2$  (or 55 m diameter) are shown in Figure 35. The effect of reducing the flight path angle dispersion and optimizing the guidance tuning results in a maximum  $\Delta V$  (with the exception of one case circled in red) below the

budgeted 150 m/s.

L/D=0.15 cases (not shown) still remained almost 400 m/s over the budget, therefore, L/D=0.2 was determined to be the breakpoint in L/D. The final ballistic number breakpoint was selected as 33.33 kg/m<sup>2</sup>, which corresponds to the 55 m HIAD. In summary, the breakpoint of the aerocapture simulation using the HYPAS guidance algorithm was determined to be for cases below an L/D of 0.2 and ballistic number of 33.33.

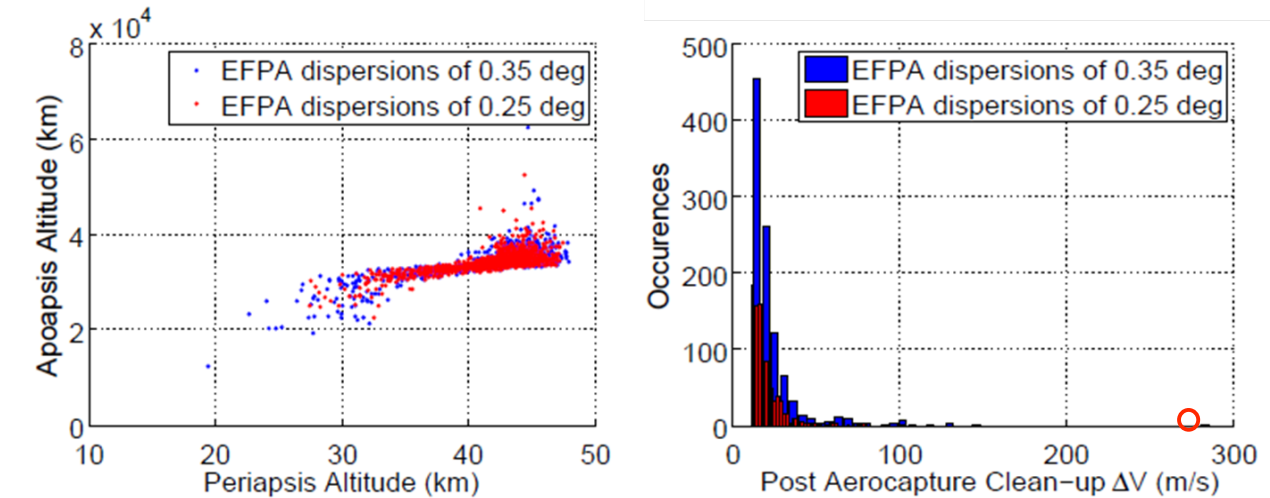


Figure 35. Effect of Flight Path Angle Dispersions for L/D=0.2, Bn=33.33 kg/m<sup>2</sup>

## 4.2 Entry, Descent and Landing

### 4.2.1 Comparison of EDL-SA to DRA5

EDL-SA Architecture 1 is based largely on and is an extension of the EDL work done for DRA5. Due to the scope of a reference mission, DRA5 considered only a single idealized (in-plane, non-dispersed) nominal trajectory for Mars EDL. The performance of the theoretical guidance was verified by the NPC and Apollo-derived guidance algorithms. Due to lack of dispersion analysis in DRA5 and the assumption that a Mars cargo vehicle would have to demonstrate human rated g loads (~3g's), the entry g's were limited to a constant 2 g's. However since DRA5, the Constellation Program Human-Systems Integration Requirements, HSIR, document has indicated that the entry g level can be as high as 4 or greater for short durations. So the entry g's for EDL-SA has been constrained to a maximum of 4 g's on entry including dispersions. Using linear feed back to maintain a constant 2 g entry, a throttle setting to maintain a constant 3g terminal descent and simple mass model, DRA5 provided an initial design point for modeling more detailed EDL phases for multiple EDL-SA architectures.

Other design characteristics similar to both DRA5 and EDL-SA include entry from a 1 Sol orbit (33793 x 250 km), use of a 10x30 m rigid aeroshell (for the EDL-SA rigid mid L/D configurations), a 40 mt useable landed payload, a 3g system thrust-to-weight and an 80 lbf/lbm engine thrust-to-weight. The touchdown phase for both studies, similar to Viking, reduced the vehicle velocity to 2.5 m/s for 5 seconds prior to touchdown at 0 km above the MOLA areoid at an equatorial landing site which was fixed for all EDL-SA architectures to allow for cross and down range dispersion evaluation.

Throughout the DRA5 EDL analysis it was evident that the design and conclusions relied heavily on a crude mass model. Initial mass estimates were extrapolated from vehicles orders of magnitude less massive than DRA5. Work was done for EDL-SA to incorporate response surface methodology to

increase the fidelity of the structural masses, and thermal analysis was performed to obtain better estimates of TPS material mass to the first order. The result of incorporating the structural, TPS and propellant models into a single routine, which could be iterated to convergence within the POST2 simulation, was a mass model that provided traceability to individual components as well as the ability to apply standard and growth margins appropriately. EDL-SA recognizes the limitations of the mass model and realizes that detailed packaging analysis of the components is required to further increase the fidelity of the model.

Little is known about the ability to control the very large vehicles considered for EDL-SA. DRA5 used only a “pseudo”, in-plane guidance. EDL-SA analysis incorporated a more flight-like theoretical guidance that included analysis of various control methods, namely using bank reversals and direct center of gravity control. For bank angle control realistic bank reversals and error bounds were set to provide three reversals, nominally. For center of gravity control a mass movement rate of one inch per second is assumed. Unlike a flight guidance algorithm, the theoretical guidance has full knowledge of the atmosphere and aerodynamics and is much quicker to implement and run in the simulation. The performance of the theoretical guidance was verified by both NPC and Apollo-derived guidance algorithms.

#### 4.2.2 EDL Strategy

**DRA5** – To summarize, the DRA5 simulation used a pseudo guidance activated at 1.75 g’s on entry. The pseudo guidance uses linear feedback to select the (constant) bank angle to maintain 2 g’s. The simulation was allowed to select the time to turn off the guidance and fly full lift up until selecting engine initiation. Engines were modeled to hold 3 g’s until the vehicle velocity was 2.5 m/s at which time the vehicle holds that velocity for 5 seconds prior to touch down. The entry trajectory is idealized but, as will be shown, provided a good approximation of the higher fidelity EDL-SA strategy.

**EDL-SA** – The strategy of the EDL-SA exploration class EDL is similar for all architectures and is described in detail. Specific design parameters allowed to vary between architectures are noted. The entry phases include deorbit, atmospheric entry, pullout, and heading alignment. Descent phases include lander/drag device separation and terminal descent. The landing phase details vehicle touch down criteria.

The first step in the exploration mission EDL design (and the primary difference from DRA5) is to converge the mass model using an in-plane guidance and to determine the appropriate entry point such that the trajectory ends at the preselected landing target. Controlled parameters include the deorbit  $\Delta V$  from apoapsis of a 1 Sol orbit and the altitude at which the separation from the drag device occurs such that the vehicle lands within 50 m of the target. The POST2 simulation modifies the trajectory until parameters such as dynamic pressures and aero-heating characteristics permit mass model convergence.

The first EDL phase, *deorbit*, begins with the POST2 simulation selecting the deorbit  $\Delta V$  from the apoapsis of the 1 Sol elliptical orbit to modify heat rate and dynamic pressure as needed to minimize the arrival mass. The second phase, *atmospheric entry*, begins at a geographic radius of 3255.2 km and the atmosphere is activated. The third phase, *pullout*, performed after the mass model has converged, is achieved using the theoretical guidance that employs either a bank reversal strategy based on allowable heading error as a function of velocity, another notable difference from DRA5.

For bank control, if the error, input by the user, is exceeded, a bank reversal is commanded. The allowable error may be different for each architecture but will nominally produce 3 reversals. POST2 is also allowed to select the initial bank angle, which is approximately 90 deg to allow for margin from either the full lift up (bank angle = 0 deg) or full lift down (bank angle = 180 deg) configuration. The guidance is initiated at 1.25 g’s for EDL-SA.

The next phase, *heading alignment*, begins at a specified velocity; the value may vary between architectures. Bank angle accelerations of five deg/s<sup>2</sup> and a max rate of 20 deg/s are based in realistic flight controllers. During the heading alignment phase, the objective is to drive the azimuth error to the landing site target to 0 deg at engine initiation. The velocity at which heading alignment begins as well as the allowable errors required to produce three reversals, nominally, may vary between architectures. These phases summarize the **entry** portion of the trajectory.

The **descent** begins with the *separation* phase in which the simulation determines the altitude to jettison the entry drag device (rigid aeroshell, HIAD, or SIAD). For DRA5 the event was assumed to be instantaneous. However, the lack of higher fidelity vehicle separation models and the desire to more realistically model the event, the mass of the decelerator is instantaneously jettisoned and the Lander vehicle is allowed to free-fall for a given amount of time to ensure no recontact. Table 12 provides the separation times for each of the architectures based on assumptions made about the nature of the separation. Details of work done to further characterize the separation or transition events can be found in Appendix B. After the allotted time, the terminal descent engines are initiated, commencing the *terminal descent* phase. Terminal descent design is governed by the desire to balance the fuel saved of using higher throttle settings (therefore higher g's) at a low altitude close to the landing site with maintaining control authority to fly out errors to allow precise landing capability (within 50 m of the target). Therefore the terminal descent is designed to use, nominally, a maximum throttle setting of 80% to reach the desired maximum nominal acceleration (2.5 g's) for only an instant before throttling back to fly a linear velocity curve with respect to changes in altitude.

The final phase, **landing**, also known as the *touch down* phase, is based on Viking heritage. Once the vehicle reaches 2.5 m/s, the velocity is held constant for 5 second until the vehicle touches down at 0 km above the MOLA areoid at -1.18 deg North latitude and 182 deg East longitude.

**Table 12. Architecture Component Separation Times**

Architecture	Separation	Time (s)
1	Rigid areoshell from descent stage	20
2,4,5,6	HIAD from descent stage	15
7	Rigid aeroshell from SIAD	20
7	SIAD from descent stage	10
8	HIAD and SIAD from descent stage	10

As mentioned previously, certain parameter values like deorbit  $\Delta V$ , altitude at separation, heading alignment initiation and azimuth errors, as well as additional separation and deployment events required in Architectures 7 and 8, can vary between architectures. However, the general strategy for each architecture remains the same. Figure 36 shows the reference altitude versus velocity plot for each architecture.

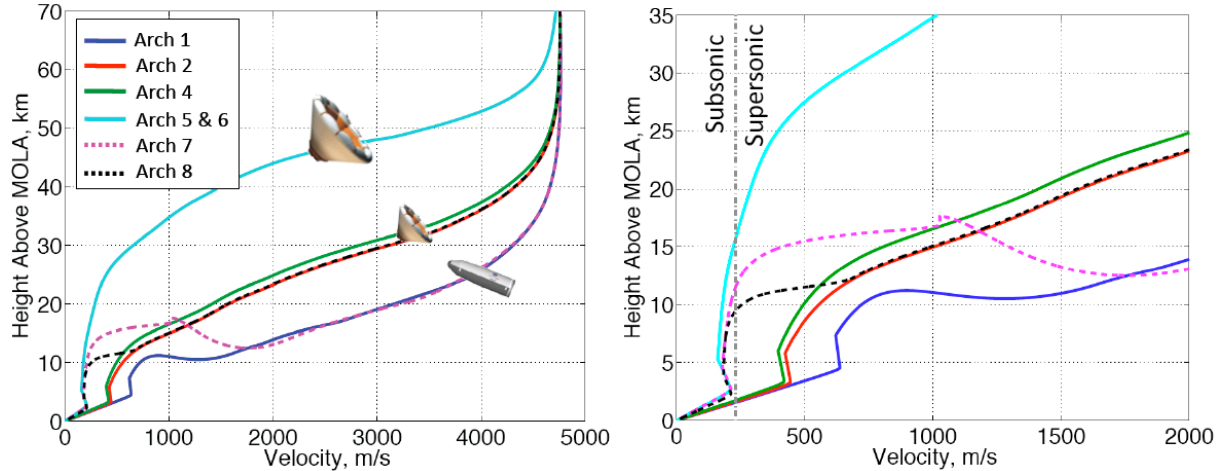


**Figure 36. EDL-SA Exploration Class Altitude Versus Velocity**

### 4.2.3 Nominal and Monte Carlo Results

Each exploration architecture was simulated using POST2 according to the strategy and models outlined previously. Unlike DRA5, Monte Carlo dispersion analysis (using 2000 cases) was performed on most architectures, including dispersion on aerodynamics, entry state and the atmosphere. Table 13 shows the nominal value and perturbation for each Monte Carlo input parameter. The aerodynamic coefficient multipliers are applied to aerodynamic database output and the atmospheric model (MarsGRAM) dispersions and winds are applied to all cases except the nominal. Detailed nominal trajectory and Monte Carlo results for the architectures are provided below.

**Table 13. EDL-SA Monte Carlo Dispersions**

Parameter	Nominal Value	Perturbation	Distribution
Nominal Coefficient multiplier	1	+/- 10 % ( $3\sigma$ )	Normal
Axial Coefficient multiplier	1	+/- 10 % ( $3\sigma$ )	Normal
Angle of Attack (deg)	55.0, -22.2, -22.2, 55.0, -22.2	+/- 5 ( $3\sigma$ )	Normal
Engine $I_{SP}$ (sec)	369	+/- 2.5 % ( $3\sigma$ )	Normal
Entry FPA (deg)	-10.8, -9.9, -9.0, -10.8, -9.8	+/- 0.25 ( $3\sigma$ )	Normal
Atmospheric Random Number	1	1-29999	Uniform
Dusttau	0.7	0.1:0.9	Uniform

**Architecture 1** – The Architecture 1 entry configuration, selected for its similarity to DRA5, includes a mid-L/D rigid aeroshell for aerocapture and hypersonic flight and supersonic retro-propulsion for descent and landing. Figure 37 shows the timeline below 30 km. The vehicle flies at 55 degrees angle of attack and has a L/D of 0.5. The heading alignment phase begins at 1700 m/s and the nominal terminal descent throttle setting is set at 80%. However, for the Monte Carlo analysis, the throttle setting is allowed to increase to 90%, which result in several cases that fly a more aggressive descent profile and use considerably less propellant than the nominal case. Additional 1 and 99 percentile Monte Carlo results, including Mach, dynamic pressure and altitude dispersions at aeroshell separation and terminal descent initiation, are included in Table 14. The DRA5 arrival mass estimate of 110.9 mt is remarkably

close to the higher fidelity EDL-SA arrival mass of 110.1 mt shown in Table 20, implying that the approximations made for DRA5 adequately represent current knowledge. Because of the use of an aeroshell, Architecture 1 is considered to be at a higher TRL than the drag devices considered in other architectures. However, several technology challenges remain for the aeroshell including packaging, detailed modeling of the separation event and engine initiation at supersonic velocities.

**Architecture 2** – Architecture 2, which uses a HIAD for aeorcapture and entry along with supersonic retro-propulsion for terminal descent, was selected to evaluate the mass savings of using a dual use TPS HIAD over a rigid mid-L/D areoshell. The 23 m inflatable design is based on the MIAS concept and is currently at a lower TRL than the rigid aeroshell. The angle of attack for the vehicle is -22 degrees and the L/D is 0.33. Percentile dispersion values are provided in Table 15. The plot of the altitude versus time curve for Architecture 2 is shown in Figure 38. Plotted for reference is the similar curve for Architecture 1. Note that for Architecture 2 the 3-sigma low range to target at terminal descent initiation has been reduce from 7 km in Architecture 1 to 2.7 km resulting in reduced timeline margin for terminal descent. However, use of the HIAD, based on the mass models developed for EDL-SA, reduces the entry mass over Architecture 1 by nearly 25 mt, making it an advantageous alternative to Architecture 1, despite technical challenges including HIAD packaging, separation and dual-use TPS.

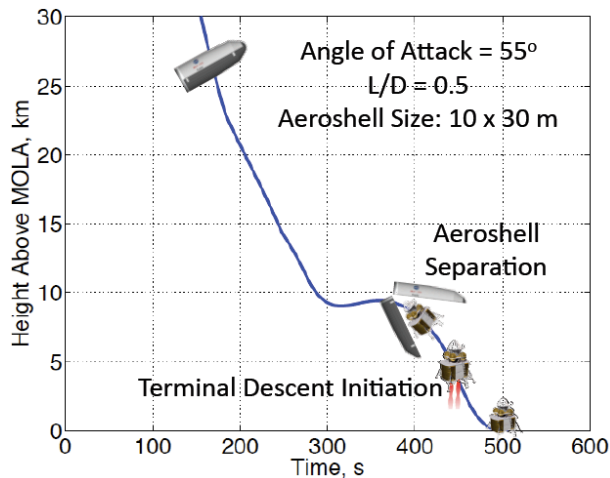


Figure 37. Architecture 1 Altitude vs. Time

**Table 14. Architecture 1 Results**

	1%	Mean	99%
<b>Aeroshell Separation</b>			
Mach	2.4	2.7	3.3
Dyn. Pres., N/m <sup>2</sup>	1077.7	1283.4	1598.3
Altitude, km	6.5	7.5	8.9
<b>Terminal Descent Initiation</b>			
Dyn. Pres., N/m <sup>2</sup>	1479.2	1721.8	2049.4
Altitude, km	3.3	4.6	6.9
Range To Targ, km	6.7	10.9	25.4
Prop Use, t	12.4	14.2	16.9

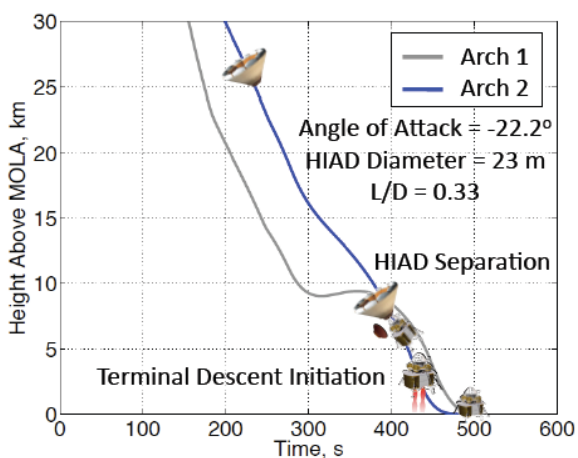
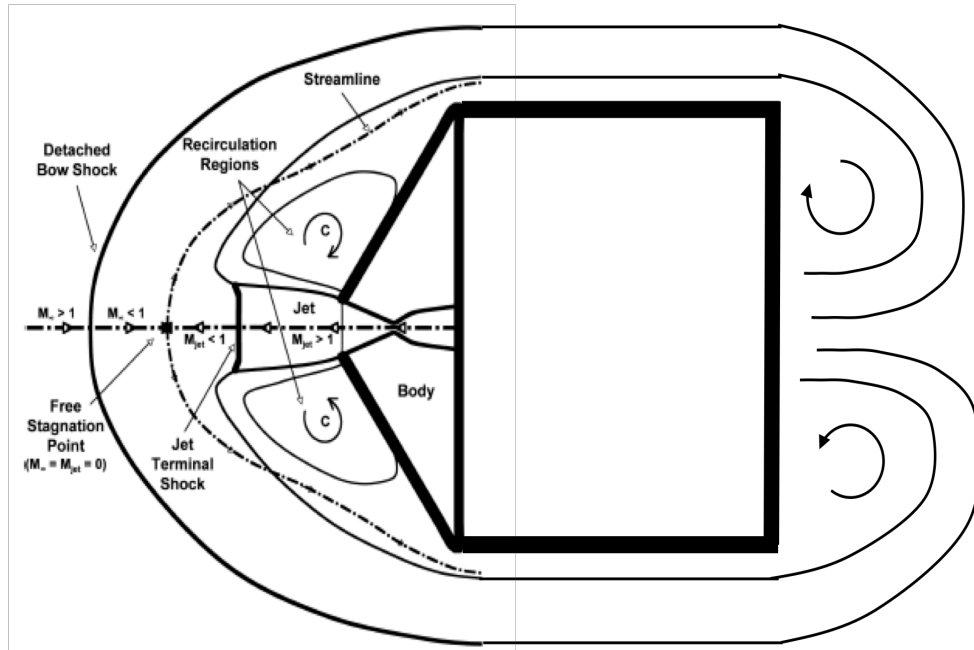


Figure 38. Architecture 2 Altitude vs. Time

**Table 15. Architecture 2 Results**

	1%	Mean	99%
<b>HIAD Separation</b>			
Mach	1.6	1.8	2.1
Dyn. Pres., N/m <sup>2</sup>	563.3	646.4	780.0
Altitude, km	5.1	5.7	6.5
<b>Terminal Descent Initiation</b>			
Dyn. Pres., N/m <sup>2</sup>	775.3	881.8	1027.2
Altitude, km	2.5	3.3	4.6
Range To Targ, km	3.3	4.9	8.5
Prop Use, t	9.0	10.0	11.4

**Architecture 3** – Architecture 3, the all-propulsive entry configuration, was the least complex EDL alternative and, using only engines, was considered to be at a relatively high TRL compared to the other architectures. However, there are major technology questions concerning the flowfield interactions of the rocket plume firing into the atmosphere at hypersonic and supersonic conditions as illustrated in Figure 39 [31]. Unknown are the impact of the total pressure on the nozzle performance and internal nozzle flow (possible flow separation), the flow stability and the resulting dynamics on vehicle control, and the resulting drag and aerodynamic heating.



**Figure 39. Rocket Plume Hypersonic Flowfield Interactions**

Because of the unknowns in drag and aerodynamic heating from the diverted forebody flowfield, the initial study results, used to determine feasibility, included no drag and no aerodynamic heating. Because no estimate of drag was made in this initial assessment, the conservative approach was to assume that no drag would be used to decelerate the system to reduce the  $\Delta V$ . The same flow-diversion assumptions were also made for the aerodynamic heating; thus no thermal protection system was used.

Therefore, Architecture 3 assumed that a nuclear thermal rocket, NTR, performs the Mars Insertion burn to place the vehicle into a 1 Sol orbit. The strategy for deorbit and entry from 1 Sol was optimized using an instantaneous burn ( $\Delta V=1200$  m/s) to transition to an intermediate orbit of 250 x 250 km orbit and then a deorbit burn of 186 m/s thereby minimizing the arrival mass and gravity losses.

The trajectory simulation was initiated at the deorbit condition. Initial thrust-to-weight ratio (T/W) was varied from 1.01 to 3.7 Mars  $g$ 's, and the altitude at thrust initiation was optimized. At a T/W of 1.010, the thrust initiation altitude was 250 km, and at T/W = 3.7 the altitude was 50 km. With atmospheric interface at approximately 125 km, the cases for T/W greater than 1.8 may not be valid with the no-drag assumption because the nozzle and vehicle forebody are not protected with diverted flow unless a very low-thrust flow divert could be used. A unique EXAMINE based mass model was developed for Architecture 3 and is summarized in Section 3.1.4 and includes no TPS mass. The deorbit mass results of the trade study can be seen in the solid lines in Figure 40. No cases exceeded the HSIR requirements for human  $g$  levels because the maximum deceleration was 3.7 Mars  $g$ 's or 1.2 Earth  $g$ 's.

The lowest deorbit mass resulted from a system T/W of 1.01 Mars g's and a total  $\Delta V$  of 5292 m/s. Using the study baseline LOX/CH4 engines with a specific impulse of 369 seconds, the arrival mass was 310 mt which is 282% higher than Architecture 1.

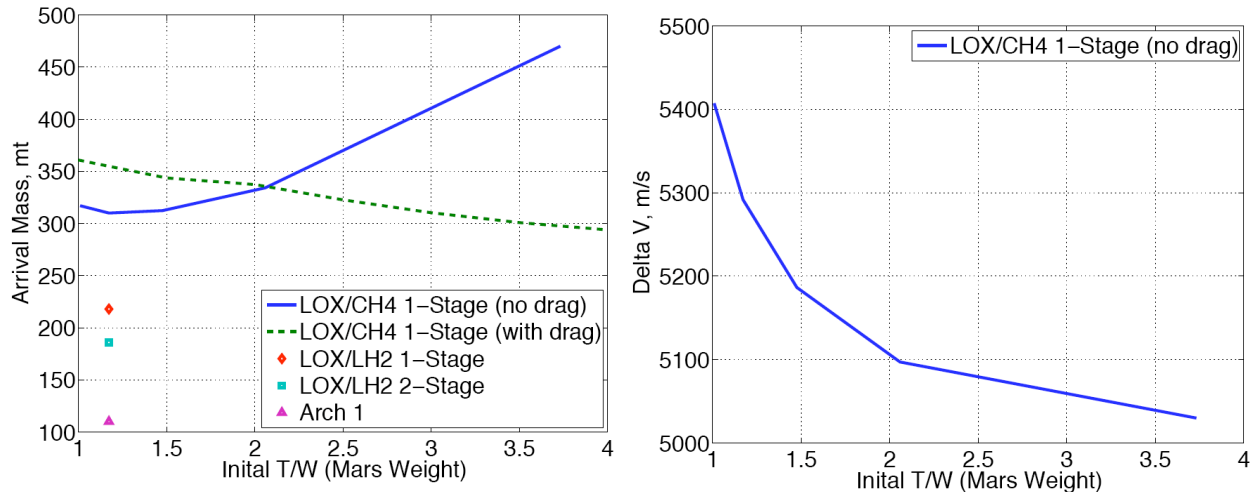


**Figure 40. Architecture 3 Arrival Mass and Delta V**

The initial study shows that an all-propulsive entry is feasible, albeit with much higher arrival masses than the other architectures considered, and it is noted that the initial study neglected several key parameters. Namely that the drag from recirculation of the flow on the forebody, skin friction drag on the sides, and base drag on the aft body is not negligible and that the no-heating assumption that utilized no TPS may be highly optimistic. Minimal mass margins were carried in this study, which differed from the margin policy used for the other Architectures. Therefore, for comparison, a second study was performed that accounted for the base drag of the aft body assuming a circular area with a nine-meter diameter. The trajectory was designed such that it maintained stagnation heat rates below  $25 \text{ W/cm}^2$ , which would eliminate the need for TPS. A mass margin policy was included that was similar to that used to evaluate the other Architectures. Also, because atmosphere drag was included, a larger (though not optimized) intermediate orbit of  $400 \times 250 \text{ km}$  was considered. As the initial thrust to weight of the vehicle was increased, the altitude at which the engines are ignited also drops, resulting in larger losses due to drag. The increases in drag loss result in less propellant required to slow the vehicle and therefore, the arrival mass is reduced. The arrival mass corresponding to the trajectories that include drag loss, thermal constraints and margined masses are shown in the dashed line in Figure 40. Lower arrival masses can be achieved using larger initial thrust to weight.

The arrival mass can further be reduced by optimizing the intermediate orbit and/or using advanced technology or staging. Using LOX/LH2 engines with a specific impulse of 450 seconds, which are the same technology engines as the cryogenic DRA5 Mars Transfer Vehicle option, the mass may be reduced to 218 mt. This option also requires the same zero-boiloff technology as the Earth-to-Mars transfer vehicles. Adding a second LOX/LH2 stage, the mass may be further reduced to 186 mt; however, this staging benefit must be traded with the additional cost and reduced reliability of using a second stage with a vehicle that is still 169% heavier than Architecture 1. It is noted that there is also no TPS or mass margin included in these estimates. No Monte Carlo analyses were performed for Architecture 3.

**Architecture 4** – The entry portion of Architecture 4 is identical to Architecture 2. However, consideration was given to Architecture 4 to compare the mass savings of using a single use (entry only) TPS on a 23 m HIAD to the dual use (aerocapture and entry) version used in Architecture 2. Therefore,

different from Architecture 2, Architecture 4 uses a rigid areoshell for aerocapture, then, prior to entry, the HIAD is inflated. The result is a larger arrival mass of 109.0 mt compared to Architecture 2's 83.6 mt but the entry mass is lighter by almost 8 mt due, in part, to the 4 mt lighter HIAD mass. Because of the difference in the entry ballistic coefficient, the architectures have slightly different trajectories but the Monte Carlo analysis results are nearly the same. See Figure 41 and Table 16. The component mass numbers are compared in Table 20. The increase in launch mass and mission complexity of using a separate aerocapture system, in addition to the technical challenges already present in Architecture 2, did not make this configuration appear practical.

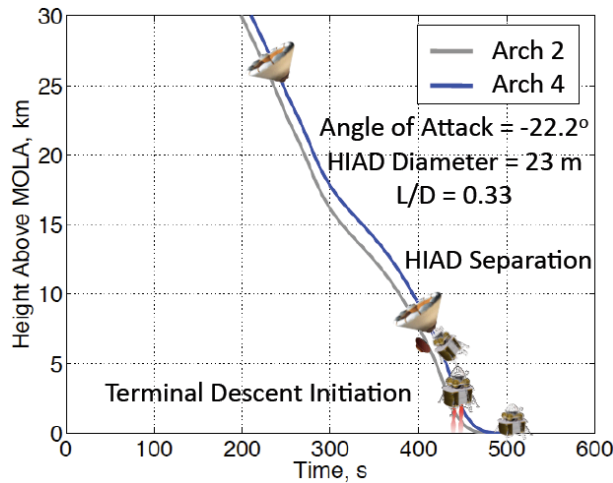


Figure 41. Architecture 4 Altitude vs. Time

Table 16. Architecture 4 Results

	1%	Mean	99%
<b>HIAD Separation</b>			
Mach	1.5	1.7	1.9
Dyn. Pres., N/m <sup>2</sup>	493.1	557.4	657.6
Altitude, km	5.3	5.9	6.7
<b>Terminal Descent Initiation</b>			
Dyn. Pres., N/m <sup>2</sup>	690.5	781.1	895.9
Altitude, km	2.7	3.3	4.5
Range To Targ, km	3.1	4.4	7.2
Prop Use, t	8.8	9.6	10.9

**Architectures 5 and 6** – Architectures 5 and 6 were selected to compare the arrival mass savings of using a very large HIAD down to subsonic speeds as an alternative to supersonic retro-propulsion, considered in Architecture 2 and 4. (This is a contingency in the event that supersonic retro-propulsion proved to be an unusable option for an exploration class mission.) Architecture 5, like Architecture 4, compared the mass saving of using a single-use TPS HIAD for entry and a rigid aeroshell for aerocapture. The simulation optimized the HIAD diameters to be 68 m and 82 m for Architectures 5 and 6 respectively. While the mass of the aeroshell and smaller HIAD in Architecture 5 did result in a lower arrival mass than Architecture 6's dual use HIAD, there was an issue in the mass model used for both architectures that calls all the results into question. The issue is that the TPS mass model used for the large HIADs was limited to a 50 m diameter. Extrapolation beyond that diameter resulted in the assumption that the areal density of the material was constant, which is not likely to be the case. Also there are additional EDL timeline challenges of successfully slowing the vehicle to subsonic speeds with adequate altitude margin to initiate the terminal descent engines and land at the target. The timeline for Architecture 6 is provided in Figure 42. Architecture 5 is very similar. A low throttle setting of nominally 65% is used to slow the vehicle starting at approximately 2.5 km such that the vehicle can touch down at the target. The large diameter HIAD flies at the same angle of attack -22 deg and same L/D as in Architecture 2. Monte Carlo one and 99% dispersions are also provided in Table 17. However, the results indicate that investments in supersonic retro-propulsion might be a more prudent choice over very large diameter HIAD systems, which will have packaging and separation technical challenges.

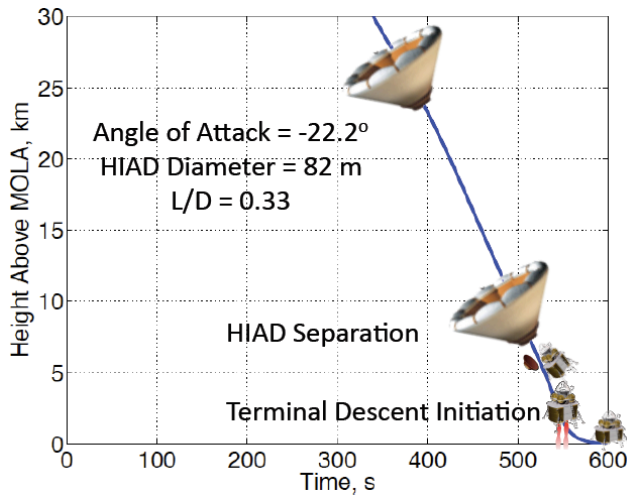


Figure 42. Architecture 6 Altitude vs. Time

Table 17. Architecture 6 Results

	1%	Mean	99%
<b>HIAD Separation</b>			
Mach	0.7	0.7	0.7
Dyn. Pres., N/m <sup>2</sup>	93.3	99.5	106.3
Altitude, km	5.0	5.2	5.4
<b>Terminal Descent Initiation</b>			
Dyn. Pres., N/m <sup>2</sup>	199.9	214.1	230.4
Altitude, km	2.6	2.7	2.9
Range To Targ, km	0.6	0.7	1.0
Prop Use, t	6.7	6.9	7.2

**Architecture 7** – Architecture 7 was selected as an alternative to Architecture 1 assuming that supersonic retro-propulsion was an infeasible option for exploration-class missions. Architecture 7 replaces supersonic retro-propulsion with a 51 m diameter SIAD and subsonic retro-propulsion. The nominal timeline compared to Architecture 1 is shown in Figure 43. Monte Carlo statistics are provided in Table 18. The entry strategy remains the same. To accommodate wind effects on the large unguided SIAD, a cross range offset at entry was included in the simulation. The altitude at engine initiation was also maximized to account for the winds during the unguided portion of the trajectory. Therefore, the maximum throttle setting during terminal decent was reduced from 80 to 65%, as well as the system thrust-to-weight from 3.0 to 2.5 g's. In addition to the aeroshell packaging and separation technical challenges, Architecture 7 has SIAD packaging, deployment, inflation and separation technical challenges. In the end, the added complexity of EDL for Architecture 7, in particular the unguided portion of the trajectory on the SIAD, results in a mass savings of only 3 mt of Mars arrival mass compared to Architecture 1.

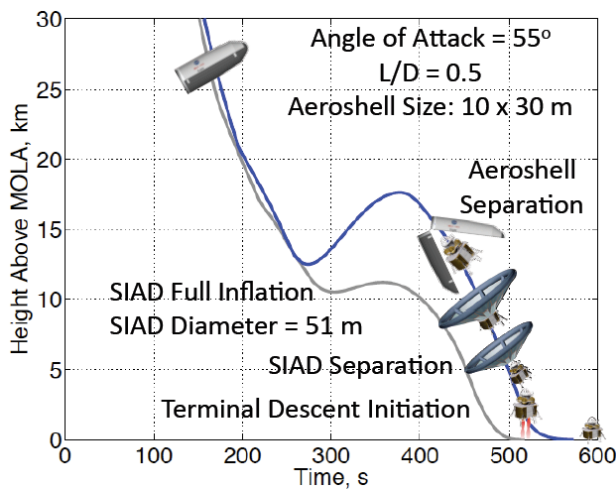
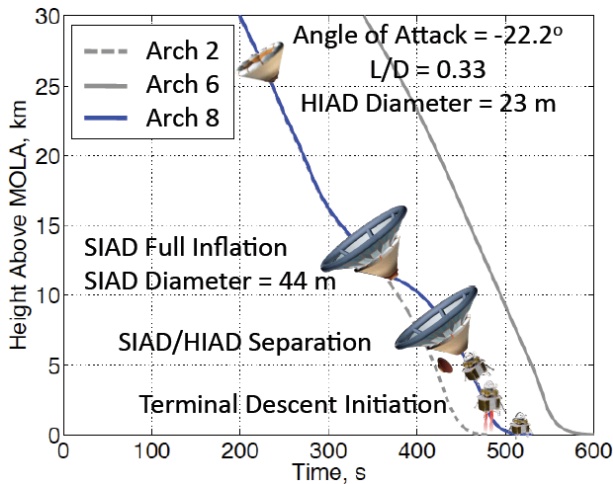


Figure 43. Architecture 7 Altitude vs. Time

Table 18. Architecture 7 Results

	1%	Mean	99%
<b>Aeroshell Separation</b>			
Mach	0.7	0.7	0.8
Dyn. Pres., N/m <sup>2</sup>	115.3	125.3	133.6
Altitude, km	4.3	4.5	4.6
<b>SIAD Full Inflation</b>			
Mach	3.5	3.8	4.1
Dyn. Pres., N/m <sup>2</sup>	983.6	1151.0	1406.1
Altitude, km	12.2	16.0	18.5
<b>SIAD Separation</b>			
Mach	4.4	4.6	4.8
Dyn. Pres., N/m <sup>2</sup>	1096.7	1416.6	2188.1
Altitude, km	12.8	17.5	20.3
<b>Terminal Descent Initiation</b>			
Dyn. Pres., N/m <sup>2</sup>	190.3	209.8	225.4
Altitude, km	2.6	2.7	2.8
Range To Targ, km	0.0	0.5	1.5
Prop Use, t	6.9	7.4	8.2

**Architecture 8** – Architecture 8 considered a HIAD plus SIAD configuration as an alternative to a single large HIAD from Architecture 6 to reduce the vehicle to subsonic speeds prior to engine initiation. The HIAD/SIAD combination included the same 23 m HIAD used in Architecture 2 and 4. The simulation determined the size of the SIAD (44 m), and it was deployed nominally at Mach 2.6, such that the terminal descent engine initiation would occur subsonically. The inflatable designs were based on the MIAS and IRDT studies. The advantage of a SIAD is the lighter mass due to deployment after peak heating, which eliminates the need for TPS, while still providing drag to slow the vehicle to subsonic speeds at engine initiation. To compare the mass savings of a HIAD/SIAD system to a larger HIAD only system, the results of the mass model suggest that using a SIAD can save approximately 40 mt of HIAD mass while costing only approximately 2 mt in SIAD mass for a net savings in Architecture 8 of approximately 38 mt over Architecture 6. See Table 20. However note the caveat of extrapolating HIAD diameter used in Architecture 6. The mass savings in reality may not be as significant. However, comparing use of a HIAD/SIAD combination to using supersonic retro-propulsion in Architecture 2, the use of a SIAD only saves approximately 3 mt of arrival mass. Despite the mass advantages, combinations of inflatables are arguably at a lower TRL than single inflatable structures, and in this particular configuration, also has additional technical challenges associated with the SIAD, increased complexity of EDL and a compressed the EDL timeline. See Figure 44 and Table 19.



**Figure 44. Architecture 8 Altitude vs. Time**

**Table 19. Architecture 8 Results**

	1%	Mean	99%
<b>Aeroshell Separation</b>			
Mach	0.7	0.8	0.8
Dyn. Pres., N/m <sup>2</sup>	131.5	144.1	155.6
Altitude, km	3.7	3.9	4.0
<b>SIAD Full Inflation</b>			
Mach	2.4	2.6	2.7
Dyn. Pres., N/m <sup>2</sup>	654.7	775.7	958.4
Altitude, km	8.4	11.9	14.3
<b>SIAD Separation</b>			
Mach	2.9	3.0	3.2
Dyn. Pres., N/m <sup>2</sup>	804.6	1008.0	1379.0
Altitude, km	8.9	12.5	15.0
<b>Terminal Descent Initiation</b>			
Dyn. Pres., N/m <sup>2</sup>	195.8	222.0	242.6
Altitude, km	2.2	2.3	2.5
Range To Targ, km	1.0	1.1	1.5
Prop Use, t	6.2	6.4	6.7

**Mass** – It is acknowledged that there are many cost functions by which to evaluate the various technologies and Architectures in this study. It is difficult to quantify timeline margin when the details of transitions are only now being investigated. It is difficult to apply error margins on the mass model because there are few data points with which to validate the model. However, mass is the easiest to quantify. For this reason, the primary comparisons between architectures have been component masses that include standard margins and the values are provided for each Architecture in Table 20. The components in the table include a standard 30% mass margin as well as a 15% mass growth allowance. It is also recognized that environmental parameters are of interest for defining and identifying requirements for various technologies. For that reason Table 21 has been included.

**Table 20. Component Dimensions and Masses using Standard Margins**

Architecture	1	2	3	4	5	6	7	8
HIAD Diameter (m) Aerocapture/Entry	--	23.0	--	23.0	67.8	81.9	--	23.0
SIAD Diameter (m)	--	--	--	--	--	--	44.6	44.3
Aerocapture/Entry BN (kg/m <sup>2</sup> )	396.1	154.0	--	134.6	20.6	20.4	412.0	152.5
Descent BN (kg/m <sup>2</sup> )	--	--	--	--	--	--	27.2	40.8
<b>Mass (mt)</b>								
Arrival Mass	110.1	83.6	265.2	109.0	133.5	140.5	107.4	80.6
Deorbit Mass	<b>109.2</b>	<b>82.8</b>	<b>188.1</b>	<b>75.1</b>	<b>98.0</b>	<b>139.4</b>	<b>106.3</b>	<b>79.6</b>
Aeroshell, AS (Total)	28.9	0.0	--	26.0	27.0	0.0	28.8	0.0
AS Structure	18.3	--	--	18.4	19.3	--	18.2	--
AS TPS	10.6	--	--	7.6	7.6	--	10.6	--
Avionics and Separation Structure	2.0	2.1	--	4.3	7.4	8.5	2.0	1.9
Entry RCS (Total)	10.8	7.1	--	9.9	14.7	16.8	11.7	7.4
RCS Dry Mass	5.2	2.7	--	5.8	9.2	9.9	6.1	2.9
RCS Propellant	5.5	4.4		4.1	5.5	6.9	5.6	4.5
HIAD (Total)	--	10.6	--	6.0	25.7	56.0	--	10.6
HIAD Structure	--	6.0	--	3.1	10.7	22.3	--	5.9
HIAD TPS	--	4.7	--	2.9	15.0	33.7	--	4.7
SIAD Mass	--	--	--	--	--	--	6.8	2.1
Descent Stage, DS	28.4	23.8	148.1	22.8	18.7	19.2	18.1	18.6
DS Dry Mass	12.3	11.7	19.2	11.2	9.9	10.5	10.2	10.4
DS Propellant	16.2	12.0	128.9	11.6	8.8	8.7	7.9	8.2
Landed Mass	52.3	51.8	74.7	51.2	49.9	50.5	50.2	50.4
Payload Mass	40.0	40.0	40.0	40.0	40.0	40.0	40.0	40.0

**Table 21. Nominal Environment Conditions**

Architecture→	1	2	3	4	5	6	7	8
<b>Aerocapture</b>								
Peak Stag Heat Rate (W/cm <sup>2</sup> )	122.8	74.6	--	--	--	36.6	--	--
Peak Ames Heat Rate (W/cm <sup>2</sup> )	335.8	88.8	--	--	--	36.7	--	--
Total Stag Heat Load (J/cm <sup>2</sup> )	13563.8	7665.3	--	--	--	3894.9	--	--
Total Ames Heat Load (J/cm <sup>2</sup> )	34499.4	7944.4	--	--	--	3433.4	--	--
Peak Dynamic Pres. (N/m <sup>2</sup> )	10600.9	4072.6	--	--	--	1061.6	--	--
Peak Earth G load	3.0	2.9	--	--	--	3.0	--	--
<b>Entry</b>								
Deorbit ΔV (m/s)	15.3	14.0	1307.7	13.9	12.6	12.6	15.1	14.0
Peak Stag Heat Rate (W/cm <sup>2</sup> )	19.7	27.3	0.7	25.6	9.9	9.9	19.5	27.2
Peak Ames Heat Rate (W/cm <sup>2</sup> )	119.5	27.0	5.0	24.4	6.8	5.2	117.9	26.8
Total Stag Heat Load (J/cm <sup>2</sup> )	2270.7	3070.5	102.6	2875.6	1149.5	1143.8	2363.6	3047.4
Total Ames Heat Load (J/cm <sup>2</sup> )	13297.4	2610.0	661.9	2403.1	723.4	547.7	13833.8	2593.1
Peak Dynamic Pres. (N/m <sup>2</sup> )	10506.5	4240.1	1823.1	3706.2	572.4	569.2	10961.2	4194.5
Peak Earth G load	3.0	3.0	2.0	3.0	3.0	3.0	5.2	3.0
Descent ΔV (m/s)	797.8	601.0	3701.5	585.9	447.1	435.8	438.2	406.4

#### 4.2.4 Sensitivities Study Results

A set of sensitivity analyses were run to understand how the unique capability of each architecture, such as ballistic number, lift and drag performance and guidance, perform against the following: environmental variability, engine characteristics, landing site, aerodynamics and vehicle size. The sensitivities from this study are meant to show how each architecture performs against the Figures of Merit for EDL-SA and are broken down into three categories: Environment, Performance and Design. The sensitivities for Architecture 3, 4, 5 and 9 are not presented because of the all-propulsive design, the duplication of EDL design for Architectures 4 and 5 and the late addition of Architecture 9.

**Environmental Sensitivity** – The Environmental Sensitivity separately varied the nominal trajectory for each architecture with season ( $L_s$ ), dust opacity, landing altitude above MOLA, latitude and time of day at Mars. Table 22 shows the results of the Environmental sensitivity, quantified by total mass variation per architecture. This analysis shows that the exploration class vehicle performance, in terms of mass, is insensitive to environmental effects.

**Table 22. Environmental Sensitivity**

Sensitivity	Nominal Value	Sensitivity Range	Total Mass Variation (kg) (% of total entry mass)				
			1	2	6	7	8
Architecture							
Season (Ls)	~174.5	0:30:360 deg	688 (0.7%)	863 (1.1%)	660 (0.7%)	334 (0.4%)	367 (0.5%)
Dust opacity MarsGRAM dusttau	0.7	0.1:0.2:0.9					
Landing Altitude Above MOLA	0 km	-4:0.2: 2.5 km	3724 (3.6%)	2582 (3.4%)	1860 (2%)	1075 (1.1%)	464 (0.6%)
Latitude	-1.177	-75:15:75 deg	1555 (1.5%)	2053 (2.7%)	2146 (2.3%)	941 (1%)	890 (1.2%)
Time of Day	5:30 am	0:1.5:24 hours	591 (0.6%)	574 (0.8%)	494 (0.5%)	430 (0.4%)	226 (0.3%)
Time of Day	5:30 am	0:1.5:24 hours	591 (0.6%)	574 (0.8%)	494 (0.5%)	430 (0.4%)	226 (0.3%)

**Performance Sensitivity** – The Performance Sensitivity varied engine thrust-to-weight and specific impulse and retro-propulsion aerodynamics of each architecture’s nominal trajectory. Table 23 shows the Performance Sensitivity results for Architectures 1, 2 and 6 through 8. The thrust-to-weight sensitivity showed that, while it is important for powered descent performance, it is insensitive to arrival mass. Specific impulse variation for each of the architectures also showed insensitivity in that the low time-on-engines result in a minimal effect of specific impulse on arrival mass. Historical investigations to supersonic retro-propulsion have indicated engine placement can augment drag performance. However, drag only accounts for 2.5% of powered descent  $\Delta V$ , making the supersonic retro-propulsion aerodynamic augmentation insensitive and providing minimal benefit to arrival mass among all architectures.

**Table 23. Performance Sensitivity**

Sensitivity	Nominal Value	Sensitivity Range	Arrival Mass Change				
			1	2	6	7	8
Architecture							
Engine Thrust to Weight	80 lb <sub>f</sub> /lb <sub>m</sub>	50:5:90	-1.1 MT (-1 %) / 10(lb <sub>f</sub> /lb <sub>m</sub> )	-1 MT (-1.4 %) / 10(lb <sub>f</sub> /lb <sub>m</sub> )	-1.3 MT (-1.4%) / 10(lb <sub>f</sub> /lb <sub>m</sub> )	-0.9 MT (-0.9%) / 10(lb <sub>f</sub> /lb <sub>m</sub> )	-0.91 MT (-1.2%) / 10(lb <sub>f</sub> /lb <sub>m</sub> )
Vehicle Thrust to Weight	3 g’s	2:0.25:4	0.73 MT (0.7%) / g	0.86 MT (1.1%) / g	-0.91 MT (-1.0%) / g	0.63 MT (0.7%) / g	1.1 MT (1.5%) / g
Specific Impulse	369 sec	355:2.5:37 5	-0.61 MT (-0.6 %) / 10 sec	-0.43 MT (-0.6%) / 10 sec	-0.31 MT (-0.3 %) / 10 sec	-0.24 MT (-0.2 %) / 10 sec	-0.25 MT (-0.3 %) / 10 sec
Supersonic Aerodynamic Augmentation	Ca=0	Ca=0:2	-0.1 MT (-0.1 %) / 10% Ca	-0.17 MT (-0.22 %) / 10% Ca	N/A	N/A	N/A

**Design Sensitivity** – The Design Sensitivity focused on the effect of varying the divert maneuver, extra propellant, payload and lift-to-drag (L/D). Table 24 shows the results of the Design Sensitivities for each architecture. The L/D sensitivity looked at increasing L/D while maintaining the same vehicle ballistic number, which by increasing L/D up to 10%, has minimal sensitivity to arrival mass. The divert maneuver is included to reduce the risk of aeroshell far-field recontact after separation and uses only beta control (modified gravity turn) to perform. For architectures with a low engine ignition velocity, the trajectory does not have the necessary energy to make large divers. For large divers, Architectures 6 and 8 are not optimal, but provide the most sensitivity to arrival mass. Architectures 1 and 2 carry more energy at terminal descent ignition allowing for larger divers, making them least sensitive with arrival mass. However, the EDL design of Architecture 7 makes it very difficult for it to perform any kind of divert and was therefore not analyzed. Payload is modeled as landed usable mass on the Mars surface and does not include any of the EDL system mass. The payload sensitivity showed that mass growth is a linear relationship of arrival mass versus payload mass and showed similar linearity between each architecture.

**Table 24. Design Sensitivity**

Sensitivity	Nominal Value	Sensitivity Range	Arrival Mass Change				
Architecture			1	2	6	7	8
Divert Maneuver	0 km	0:0.5:3.0	-0.1 MT (-0.1 %) / 0.5 km	-0.3 MT (-0.4 %) / 0.5 km	-4.1 MT (-4.4 %) / 0.5 km	N/A	-2.5 MT (-3.4 %) / 0.5 km
Extra Propellant	0 MT	0:0.5:5.0	1.9 MT (1.84%) / MT Prop	1.93 MT (2.51 %) / MT Prop	2.72 MT (2.95%) / MT Prop	1.74 MT (1.8 %) / MT Prop	1.74 MT (2.4 %) / MT Prop
Payload	40 MT	10:5:60	1.72 MT (1.67 %) / MT Payload	1.79 MT (2.33 %) / MT Payload	2.29 MT (2.48 %) / / MT Payload	1.54 MT (1.59 %) / / MT Payload	1.71 MT (2.34 %) / / MT Payload
L/D	0.51 Rigid 0.33 Inflat	75%:125 %	-0.782 MT (-0.76 %) / 10% Lift	-0.485 MT (-0.63 %) / 10% Lift	N/A	N/A	N/A

**Summary**

In summary, the impracticality of designing and carrying separate systems for aerocapture and entry has rendered the Architecture 4 and 5 unlikely candidates for further study. Decreasing engine throttle settings and igniting engines at higher altitudes has mitigated the small range-to-targets at subsonic engine initiation in Architectures 6, 7 and 8. The results have been included in the nominal and Monte Carlo analysis; however, the sensitivities studies have not been updated to reflect the performance of the new configuration. The more significant issue is accurate mass modeling of large HIADs (>50 m diameter). The assumptions made in this study, namely to assume constant areal density for diameters larger than 50 m is probably too conservative. Current mass models perhaps unrealistically penalize those architectures, namely 5 and 6, although packaging and inflation issues remain. The compressed EDL timeline that results from using subsonic retro-propulsion makes Architectures 6, 7, and 8 less likely candidates for exploration-class missions but should not be ruled out for robotic missions. Finally, Architecture 1 and 2, with their relatively less complex EDL, indicate that the HIAD, mid L/D aeroshell and supersonic retro-propulsion are technologies to be considered in more detailed study for exploration class missions.

## 5 Packaging

### 5.1 Preliminary Packaging

A preliminary packaging analysis was performed to aid in stage sizing and configuration transition analyses. Engines, deceleration devices, propellant tanks, and major structural elements were packaged for each architecture approach. Figure 45 shows the packaging for Architecture 2, and includes a stowed HIAD on the far right side that would be deployed on-orbit prior to entry. All required elements can easily be accommodated within a 20 m length, rather than the allotted 30 m. The propellant tanks are only a small portion of the required volume, which is dominated by the engines and the habitat and airlock. Significant volume remains for packaging subsystems and cargo (e.g., rovers).

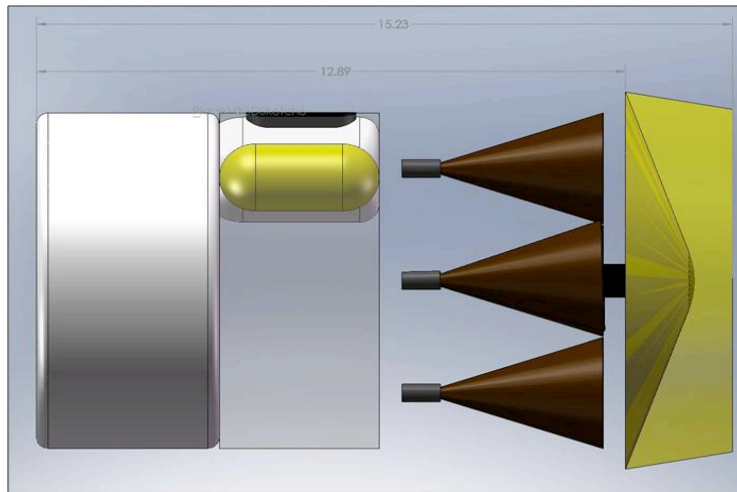


Figure 45. Architecture 2 Packaging

### 5.2 HIAD Packaging

HIAD packaging studies were initiated as a part of EDL-SA's conceptual development of the 23 m HIAD TPS. These studies have been carried forward into the EDL TDP Flexible Ablator TPS activities. At the outset of the packaging study summarized below, discussions were held with personnel at GRC [32], who are conducting preliminary design studies of the Ares V shroud. Inputs from these discussions (presentation packages/references of Titan IV shroud designs [33]) and concepts for the flexible ablator were accounted for in the packaging presented below.

Several packaging assumptions are made. First, the barrel of the Ares V shroud will be a right circular cylinder of 10 m outer diameter and will extend upward from the base toward the nose with an overall shroud length of 30 m. Second, the GRC design allowed an annular zone 1 m thick between the payload and the inner diameter of the shroud for acoustic blankets. It was assumed that the HIAD TPS could be placed between the inner diameter of the shroud and payload other than the HIAD TPS, serving a partial dual-use as the flexible TPS and as an acoustic blanket. Thirdly, based on the FIAT HIAD sizing presented in Section 3.5.1, and early trials of making silicone impregnated silica felt flexible TPS, it was assumed that the TPS thickness would be 3.8 cm thick and could be folded in a radius of 15.2 cm.

Figure 46 depicts the first attempt at the HIAD TPS packaging where the 23 m diameter "Apollo" flexible ablator (shown in grey) was folded 50 times in a uniform, "umbrella" fashion. The central rigid TPS (shown in red) was assumed to be 7.5 m in diameter. For this scheme, the HIAD would be contained

in the annular volume inside the shroud with an inner diameter of 7.5 m and an outer diameter of 9 m. The required length of the annular volume would be 10 m.

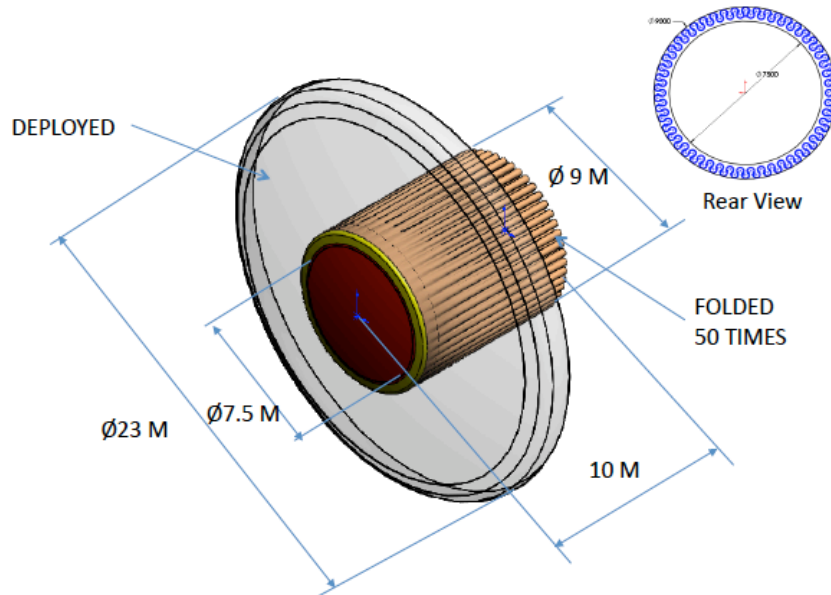


**Figure 46. First Attempt at HIAD TPS Packaging**

Figure 47 depicts an improved packaging scheme, also in an “umbrella” fashion, except there are only six folds. The three views shown depict the packaged HIAD wrapped around the payload volume, covering the payload as a blanket. The sketch in the upper left corner shows the 23 m diameter “Apollo” shape in grey while the star-shaped figure, colored in yellow, depicts the initiation of the folding. Here the cylindrical volume for the HIAD stowage has an inner diameter of 8 m and an outer diameter of 9 m. The difference between the 10 m outer diameter of the Ares V shroud and the 9 m outer diameter of the HIAD stowage volume accounts for shroud structure and additional acoustic blanketing to that of the dual use acoustic shielding provided by the flexible ablator. Again, the red object in the drawing depicts the solid nose TPS for the HIAD. In this scheme, the HIAD TPS is contained in a cylindrical volume of 8 m inner diameter, a 9 m outer diameter and an overall length of 9 m.

Importantly, these studies indicate that the HIAD TPS can serve, to some extent, a dual use for acoustic shielding for launch loads to the payload. They also provide early concepts for HIAD packaging that accounts for the allowable bending radius of the flexible ablator.

It is anticipated that the EDL TPS Flexible Ablator group will be able to more accurately define HIAD TPS ablator thicknesses and folding radii during FY10 and FY11. As this information becomes available, improved packaging will be forthcoming. In the future, study should be extended to increase the understanding of the dual use of HIAD TPS for shielding payload against acoustic loads. Finally, it is important that the possibly detrimental effects of acoustic launch loads on flexible TPS should also be evaluated and accounted for in future designs.

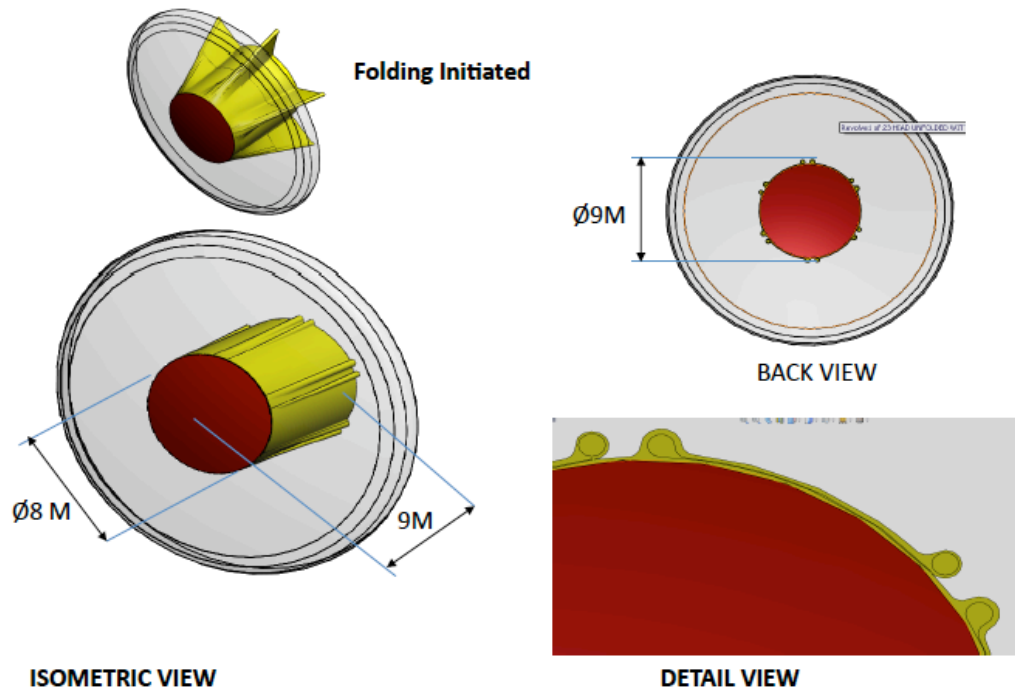


Figure 47. Second Attempt at Packaging the 23 m “Apollo” HIAD

## 6 Figures of Merit

The EDL-SA Figure of Merit (FOM) assessment activity fulfills the requirements of the EDL-SA project to assess technologies using a process that has heritage and utilizes the expertise of the EDL community. The outcome from this process gives decision-makers a systematic perspective of the trade-offs for each of the candidate technologies needed to enable an exploration class Mars mission which can be used to form a defensible technology development roadmap. An overview of the FOM assessment process and the results of the assessment are presented in this section.

The assessment of the eight EDL architectures and technologies that are identified within the architectures was based on evaluation and relative scoring of FOMs. Thirteen FOMs were used from five FOM categories: Safety and Mission Success, Performance and Effectiveness, Programmatic Risk, Affordability and Life Cycle Cost and Applicability to Other Missions. Each FOM score was derived from proxy parameters and discriminating factors based on three classes of data source: Expert opinion, simulation and analysis and past studies. Figure 48 shows all of the FOM categories, FOMs and the data sources for each category. Detailed definitions of the FOMs and their proxy parameters are given in Appendix A.

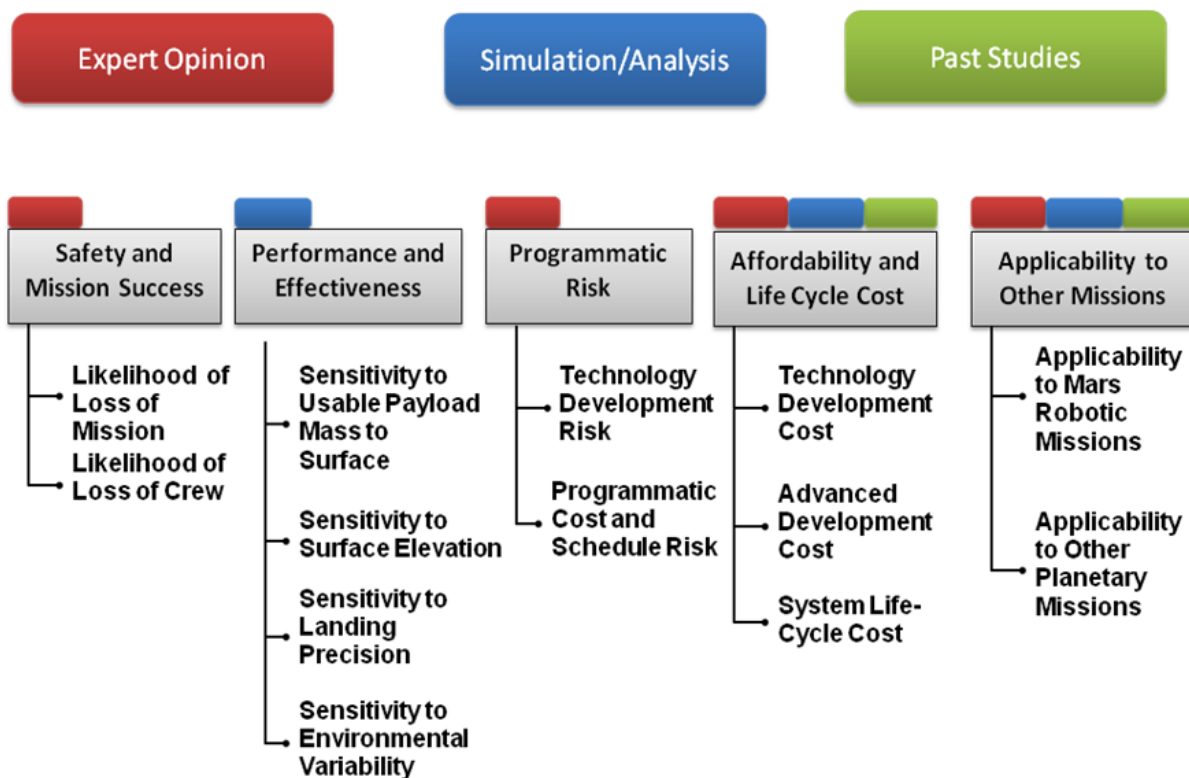


Figure 48 FOMs, Sub-FOMs and Sources Used to Evaluate

### 6.1 Assessment Process

The first step in the process includes defining the FOMs, and proxy parameters to be used. An external review of these metrics was conducted with solicited input from technology program managers. The EDL-SA analysis team developed reference architectures that would be used to assess the performance of the technologies integrated into an EDL system. In parallel to the simulation and analysis

tasks, a separate team held a series of TIMs to address non-performance related areas such as risk and cost. The data was then used to build a detailed FOM analysis worksheet that was designed to integrate the technical and programmatic factors specific to each technology in the assessment. After the worksheet based tool was developed, programmatic weights were collected from a variety of project managers and decision makers. The results of the survey were used as part of a sensitivity analysis. The EDL-SA FOM assessment process is illustrated in Figure 49.

The Technology Managers Meeting was held in May 2009 with the managers of the relevant technology programs: James L. Pittman (ARMD Fundamental Aeronautics Program/Hypersonics Project), Frank Peri (ESMD/Exploration Technology Development Program), Samad Hayati (SMD/Mars Technology Program) and David Anderson (SMD/In-Space Propulsion Program). A series of FOM Technical Interchange Meetings (TIMs) were held to collect data from subject matter experts. Table 25 lists the particular TIMs and their participants. Results from the July 2009 Transition Mechanisms TIMs are summarized in Appendix B.

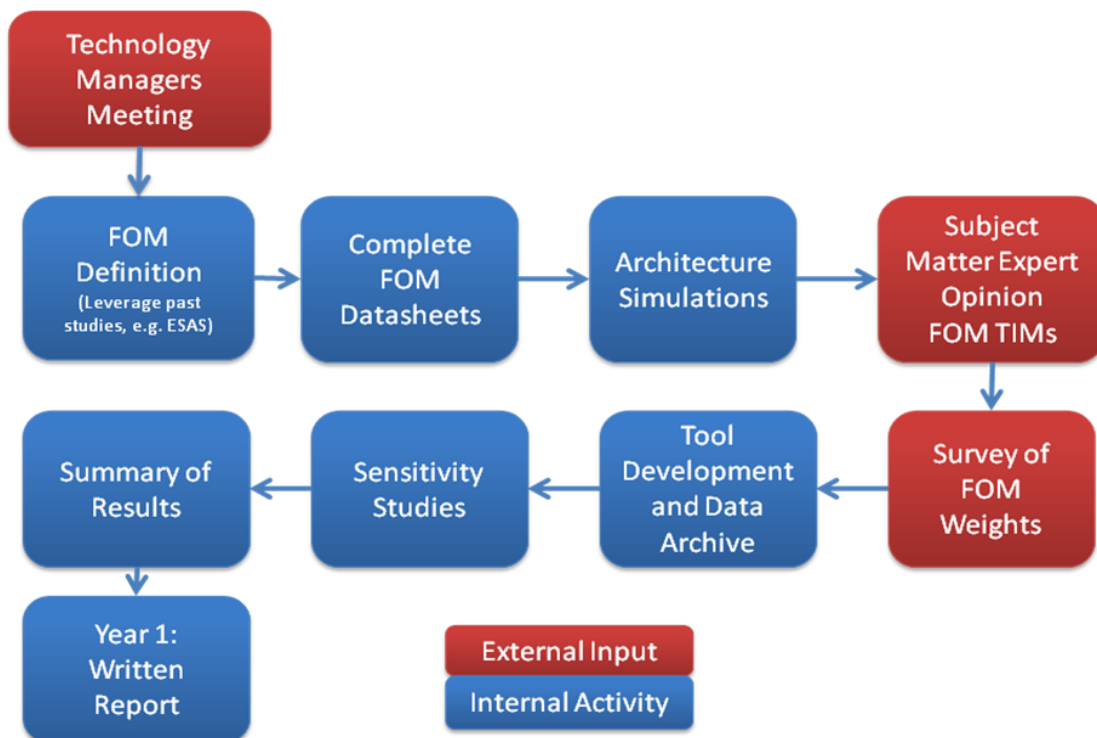


Figure 49. FOM Assessment Process

Table 25. Contributors to the FOM Assessment

Technology Program Managers Mtg. (May 2009)			
Dave Anderson	Samad Hayati	Frank Peri	Jim Pittman
Transition Mechanisms TIMs (July 2009)			
Doug Adams	Allen Chen	Ian Clark	Karl Edquist
Richard French	John Gallon	Carl Guernsey	Christian de Jong
Devin Kipp	Ashley Korzun	Chris Madsen	Tom Rivellini
Miguel San Martin	Steve Sell	Adam Steltzner	Aron Wolf
Chuck Campbell	Chirold Epp	Steve Hoffman	Don Pettit
Mike Tigges			

Programmatic Cost & Risk TIM (Nov. 2009)			
Robin Beck	Anthony Calomino	Chuck Campbell	Neil Cheatwood
Karl Edquist	Stephen Hughes	Charles Player	
Applicability to Other Missions TIM (Nov. 2009)			
Dave Anderson	John Dankanich	Samad Hayati	Tom Rivellini
Adam Steltzner	Mike Wright		
FOM Weighters (Dec. 2009–Jan. 2010)			
Neil Cheatwood	Doug Craig	Robert Dillman	Bret Drake
Dana Gould	Samad Hayati	James Reuther	Dale Thomas
Ethiraj Venkatapathy	Henry Wright	Thomas Zang	

Figure 50 shows an example of the process used to evaluate of the Programmatic Risk FOM category. The Programmatic Risk FOM category is made up of two FOMs, a) Technology Development Risk and b) Programmatic Cost and Schedule Risk. The proxy parameters for the Technology risk FOMs are: number of technologies required; TRL's of each technology and RD3 scores of each technology. The proxy parameter for the Programmatic Cost and schedule FOMs is: Level of EDL system design maturity/uncertainty for a given technology approach.

In order to quantify and justify the evaluation of each proxy parameter, the Risk TIM panelists were asked to rate the areas on the far right of Figure 50. This information was used to evaluate the proxy parameters and establish a relative score for each of the FOMs. The information from the FOMs was used to evaluate the FOM categories. A tool was developed to store the information from the TIMs and to roll up values from the proxy parameters into relative values for the FOMs.

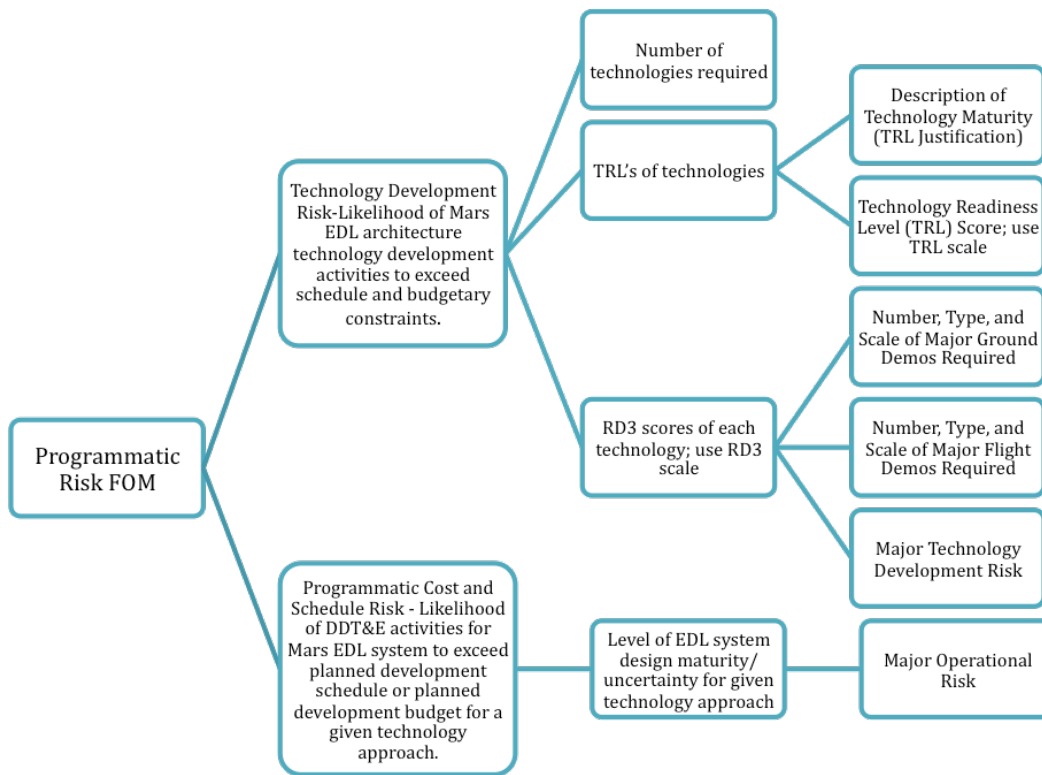


Figure 50. Programmatic Risk FOM Process Flow with Supporting Information from Program Risk TIM

## 6.2 Figure of Merit Weighting

In the last phase of the assessment process, input from programmatic experts was used to assign weights to each FOM and FOM category. A survey was sent to 11 managers, EDL subject matter experts and systems engineers that used the Analytical Hierarchy Process (AHP) to do a pairwise comparison of each FOM and FOM category. Figure 51 shows the results of the average FOM category weights based on the inputs from the surveys.

Safety and Mission Success, Affordability and Performance Effectiveness are the top three FOM categories based on the programmatic inputs collected and each of the three categories had the highest weight in at least one survey. The Applicability to other Missions FOM category was assigned the lowest weight in all but one survey (where it was ranked second to last). Programmatic risk was consistently ranked neither highest nor lowest priority.

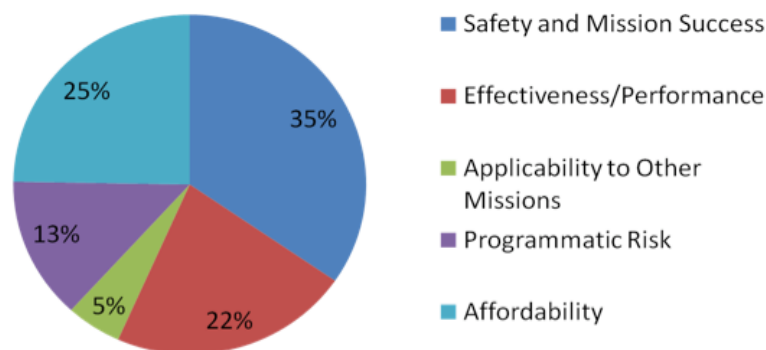


Figure 51. Average FOM Category Weights

## 6.3 Assessment Results

An assessment of both architectures and EDL technologies was performed based on the process described above. Both the architecture and technology-based approaches were designed to inform the relative benefits of EDL technologies as well as configurations of those technologies. The observations and conclusions from each assessment are included below.

### 6.3.1 Architecture Assessment Results

The following is a list of observations and conclusion based on the results of the architecture assessment:

- The architectures that utilize Dual Pulse Rigid TPS (Architecture 1 and 7) ranked high overall due to high scores in the safety, performance, and programmatic risk categories.
- The all propulsion architecture (Architecture 3) was very sensitive to the weights on all of the FOM categories. This architecture had very high scores in the safety, performance, and programmatic risk category but had a very low score for affordability due to the considerably higher mass compared to the other architectures.
- The architectures that utilize dual pulse ablative inflatable heat shields (Architecture 2, 6 and 8) scored relatively low on average. However Architecture 2 and 8 had high scores in affordability and applicability to other missions and therefore the overall score of these architectures was very sensitive to the weights placed on these two FOM categories. During the sensitivity study

Architecture 2 and 8 ranked highest overall when either affordability or applicability to other missions was valued significantly more than the other FOM categories.

- The architectures that utilize single pulse heat shields (Architecture 4 and 5) were consistently ranked low due to low scores in safety (due to the complexity of integrating two heat shields), performance, programmatic risk and affordability.
- The architectures that utilize supersonic retro propulsion (Architecture 1, 2 and 4) scored high in safety (due to lower complexity compared to inflatables) but low in affordability (due to higher mass) compared supersonic aerodynamic decelerators.
- The architectures that utilize supersonic inflatable decelerators (Architecture 7 and 8) scored high in affordability (due to lower mass) but low in safety (due to dynamic deployment and integration complexity) compared to supersonic retro propulsion.

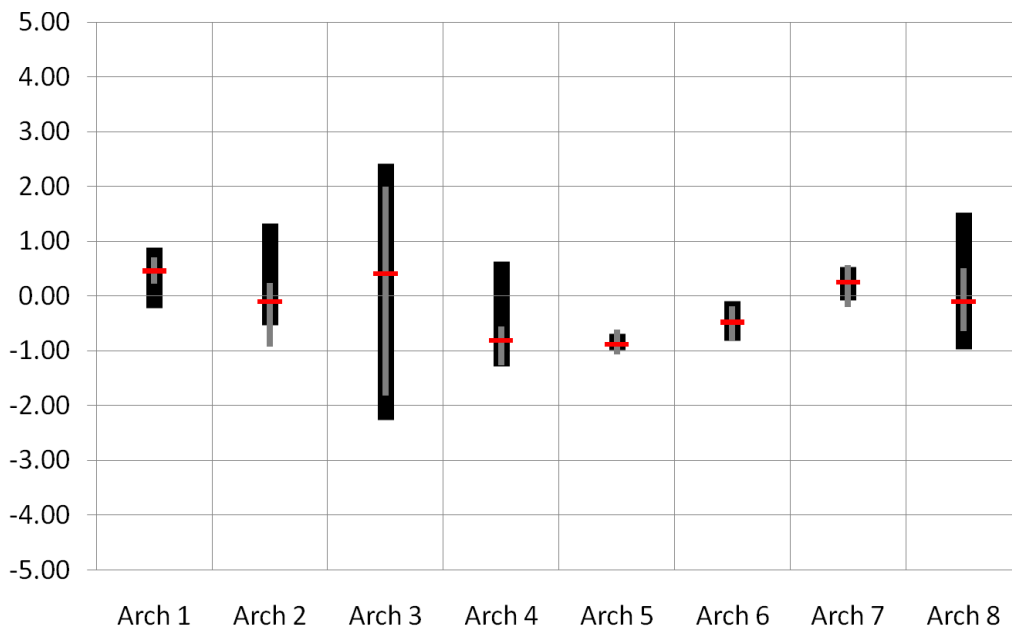


**Figure 52. Architecture Score from FOM Weight Surveys and Sensitivity Studies**

Figure 52 illustrates the range of total FOM assessment scores for each of the first 8 architectures considered as part of the study. The overall FOM score is on the vertical axis. The black bars show the range of scores encountered during the sensitivity study (where a high weight was assigned to one FOM category and low weights assigned to the other four categories). The gray bars represent the range of scores encountered based on the results of the FOM weight surveys and therefore represent results based on actual decision makers value systems. The middle tick represents the total score based on the average FOM weights. The architectures that have larger vertical bars are more sensitive to the FOM weights. Based on the mean FOM weights, Architecture 1 (rigid dual pulse TPS, and SRP) ranked highest overall. However, no specific configuration scored higher than all other architectures in either the sensitivity study or the FOM weight survey study and therefore no architecture was identified as a clear choice based on the information available at the time of the study.

### 6.3.2 Technology Assessment Results

For direct assessment of technologies, the same data collected as part of the architecture assessment could be applied directly, with the exception of the Performance and Effectiveness Category. For that category, technology-based performance metrics were needed. Since the performance data was available for all of the architectures an approach was defined such that the technology performance was based on a comparison between two similar architectures. Performance metrics for technology evaluation were assessed based on comparing reference architectures and their relative performance scores.

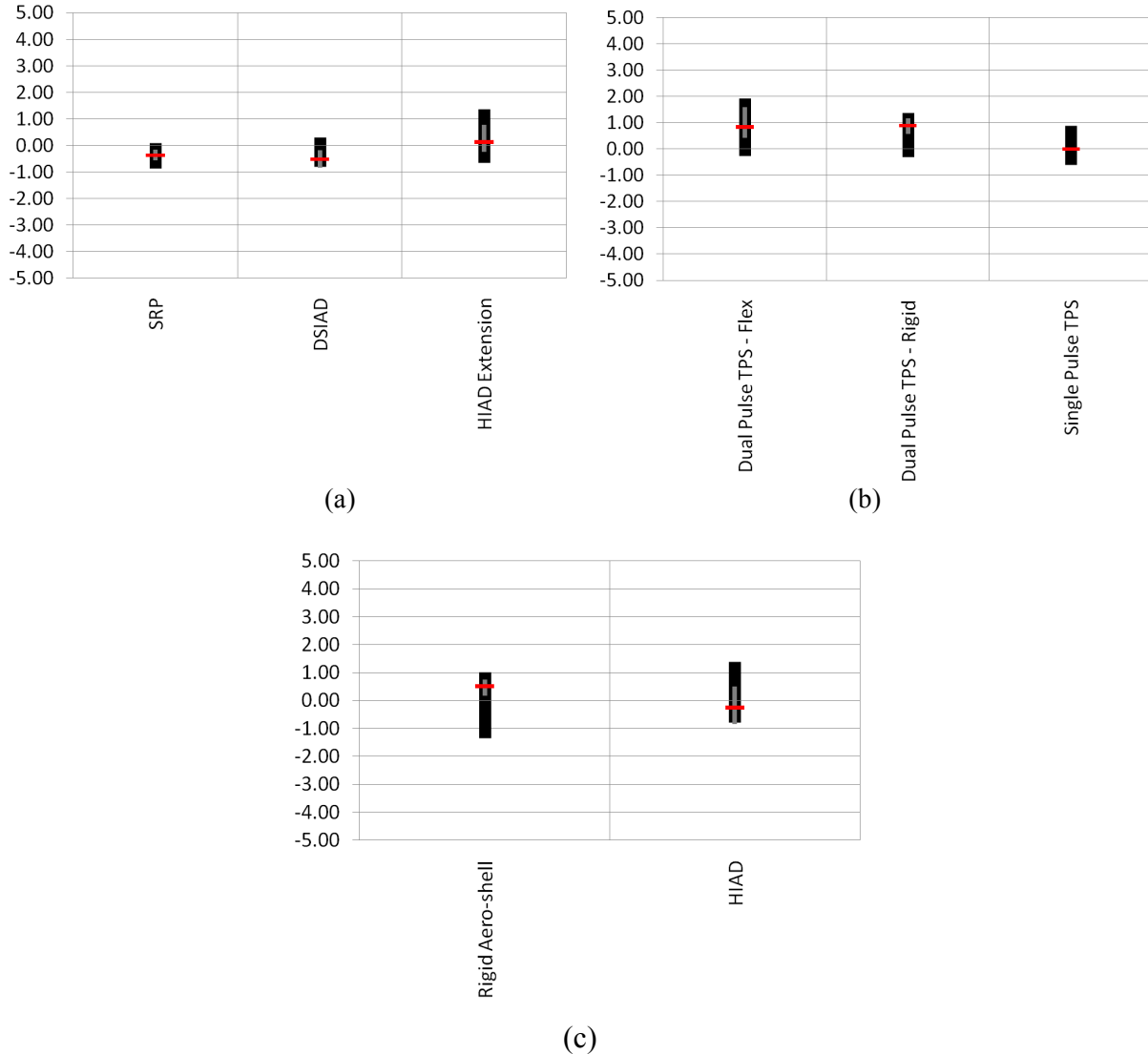


**Figure 53. Technology Score Ranges from FOM Weight Surveys and Sensitivity Study (a) Supersonic technologies, (b) TPS technologies (c) Hypersonic technologies**

Figure 53(a-c) summarize the results of the technology based assessment. The vertical axis is the total integrated score for each technology. The black bars show the range of scores encountered during the sensitivity study (where a high weight was assigned to one FOM category and low weights assigned to the other four categories). The gray bars represent the range of scores encountered based on the results of the FOM weight surveys and therefore represent results based on actual decision makers value systems. The middle tick represents the total score based on the average FOM weights.

SRP scored slightly higher on average than the SIAD configuration integrated with a rigid aeroshell. However the SIAD integrated with a deployable heat shield showed an advantage over the SRP alternative. The dual pulse TPS options scored higher on average than the single pulse alternatives primarily due to reduced mass and complexity. The rigid aeroshell scored higher on average than the deployable ablative aeroshell due to safety performance and programmatic risk. However, in none of the technology areas did a single technology rank consistently highest in either the sensitivity study or the FOM weight survey study and therefore no clear set of preferred technologies was identified as part of this assessment based on the information available at the time of the study.

The conclusions of the technology based assessment are the same as the conclusions of the architecture based assessment summarized above.

## **6.4 Summary**

Figure of Merit assessment was performed on eight exploration-class Mars EDL architectures along with assessment of the technologies used in the architectures. Based on relative values of the proxy parameters and programmatic weighting of the FOMs, Architectures 1 and 7 consistently ranked high. Architecture 3 varied greatly between worst and best architecture due to high sensitivity to FOM weights. The score for Architectures 2 and 8 were sensitive to the weights on affordability and applicability to other mission FOM categories.

The technologies required for the highest scoring architectures include: Dual pulse rigid TPS, SRP, drag SIAD, lifting SIADs, and lifting HIADs. The same technologies scored high in the technology assessment. Due to the sensitivity to decision maker values and the uncertainty in the proxy parameter inputs, no specific technologies are recommended for elimination from further consideration as a result of this assessment.

## 7 Viability Assessments

### 7.1 Dual-Layer TPS

**Dual heat pulse Proof of Concept or Validation Testing** - The objective of this viability testing was to demonstrate that a PICA atop LI-900 dual-layer TPS concept could be manufactured in a very large, 10 x 29 m configuration, and could endure heating rates of more than factor of ten greater than those seen by the Shuttle during Earth entries from the Space Station. The Orion TPS ADP developed an approach [34] to use large (~ 5 cm) honeycomb attached to the substructure and filled with blocks of TPS material. The composition of these TPS material blocks could be changed to address the local heating environments, which vary widely across the heat shield. This approach for manufacturing of the dual-layer TPS for the 10 x 29 m mid-L/D vehicle was adopted because previous arc jet testing sponsored by the Orion TPS ADP [27] showed it to be viable for heating rates at levels appropriate for both pulses, aerocapture and EDL, predicted for Architecture 1.

Figure 54 (a) illustrates the large honeycomb TPS manufacturing concept and post arc jet test articles where the material filling the honeycomb was PICA only. The PICA is bonded into the honeycomb with RTV, a bonding and gap-filling method use on the Shuttle and MSL. The test conditions for Figure 54 (b) clearly indicate that the thermal performance of PICA in honeycomb is viable at entry environments slightly exceeding the peak heating rate values predicted for the aerocapture portion of the mid-L/D vehicle shown in Figure 22 above. The same conclusion can be made from Figure 54 (c) for the lower, second, entry heating pulse also shown in Figure 22 above. At both the aerocapture and entry peak heating conditions, the honeycomb and PICA recede at approximately the same rate, and “fencing” of the honeycomb does not seem to be an issue.

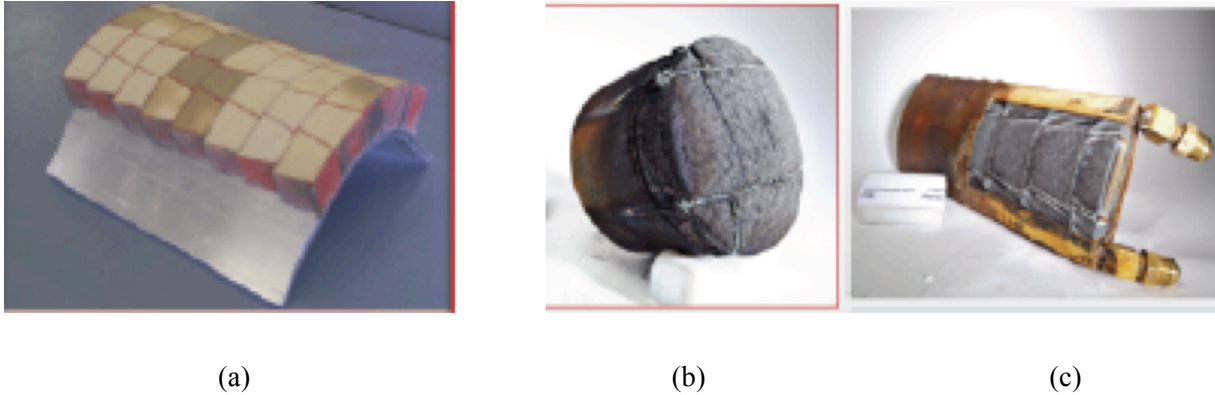


**Figure 54. (a) curved panel covered with ~5cm honeycomb filled with PICA blocks; (b) post tested stagnation iso-q model after exposure to 620 W/cm<sup>2</sup> for 30 seconds; and (c) post tested swept cylinder model after exposure at 140 W/cm<sup>2</sup> for 25 seconds**

Viability testing of the dual-heat-pulse, dual-layer concept was performed by simulating the aerocapture, on-orbit cool-off, and subsequent entry in the ARC arc jet complex. First, the aerocapture is simulated in the ARC Interactive Heating Facility (IHF) at 438 W/cm<sup>2</sup> (hot wall) and 28 kPa pressure for 75 seconds. The charred model was then stored for several months at room temperature to simulate cool down in Mars orbit. Lastly, the model is exposed to 153 W/cm<sup>2</sup> (hot wall) and 5 kPa for 109 seconds in the ARC Aerodynamic Heating Facility (AHF) to simulate the out-of-orbit entry heat pulse and understand any failure modes at burn-through into the LI-900. Figure 55 below depicts the iso-q dual-layer test article design. The model was designed with an outside ablator layer 1.9 cm thick atop a 1.9 cm

thick layer of LI-900. Five models were made; two had **no** bonding between the iso-q faces of the PICA and the LI-900 and three had a very thin layer of RTV at the boundary of the ablator and the insulator. Each model had the LI-900 press fitted against the inner face of the PICA to ensure thermal contact.

Figure 56 specifies the test thermal cycle sequence that is the best approach currently available to simulate the dual-heat-pulse maneuver. The flow in the arc jet test impinges on curved surface of the test article (left to right) and the shape of the model tends to make the surface heating constant (iso-q). Two IHF tests were run. The first was run for 75 seconds duration to correspond directly to the first pulse. It was predicted that the test would leave 0.63 cm of charred PICA by the ablative analysis tool FIAT [25]. The actual measured value was 0.61 cm. The second test allowed the model to remain in the stream until the PICA receded to the LI-900. Burn-through was predicted by FIAT to occur at 108 seconds while the actual burn through was measured at 107 seconds. Figure 57 shows the first post-tested model with 0.61 cm of charred PICA remaining.

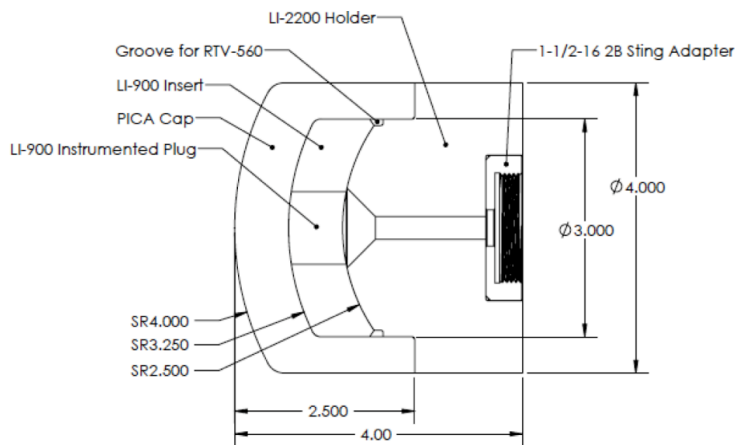


Figure 55. Iso-Q Model Design of PICA atop LI-900. Dimensions in inches.

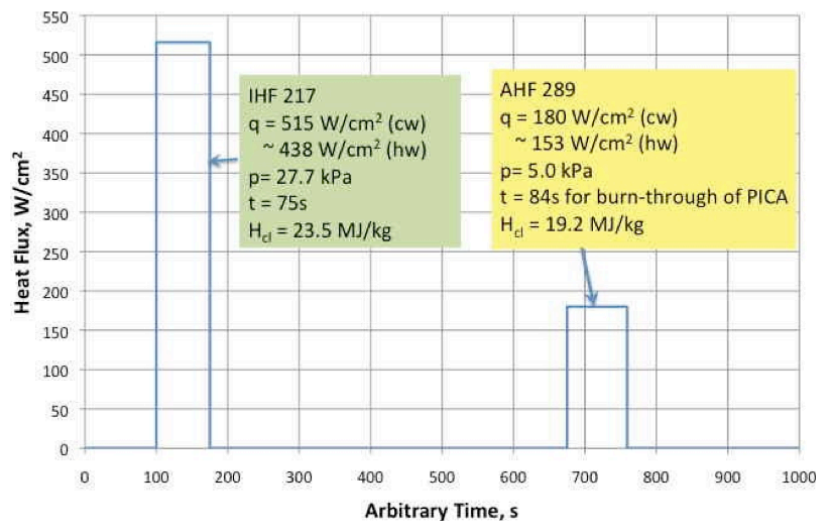


Figure 56. Test Thermal Cycle to Simulate Dual Heat Pulse

Figure 58 shows the burned-through model that was removed from the stream after 107 seconds. As can be seen, the LI-900 slumped. This is considered to be a failure mode and shows that for the flight design, there must be sufficient PICA remaining after the first pulse to prevent burn-through of the PICA during entry from orbit as discussed in the analysis section above.

A dual-layer model tested at the first pulse IHF condition with RTV bonding between the PICA and the LI-900 was stored for several months and then tested for a second heating pulse in the AHF arc jet. The second heat pulse level was  $153 \text{ W/cm}^2$  (hot wall) and 5 KPa. FIAT predicted that it would take 84 seconds for the PICA to burn-through to the LI-900. The actual time to burn-through was observed to be 83 seconds. After burn-through the test run continued for an additional 25 seconds, during which time the LI-900 slumped. The slumping was gradual, indicating that this failure mode occurs “gracefully.”

Figure 59 shows clips taken from the movie made during the AHF run at 10, 50, 82, 83, 84 and 93 seconds, respectively. These views are taken with a mirror at an oblique angle so the glowing model face appears elliptical in the figure. The front face of the model undergoes uniform recession from insertion until 82 seconds later. At 83 seconds, a brighter glowing is seen at the center of the model, and a second later, the PICA has been penetrated. At 84 seconds, one can “see” into the LI-900 region. As time progresses, the LI-900 slumps as shown in the clip taken at 93 seconds. Again the, failure is “graceful” and even the spherical dome of PICA did not break off during the completion of the run.

The data clearly shows the viability of building TPS for a  $10 \times 29 \text{ m}$  mid-L/D aeroshell for a future human Mars mission: It has been demonstrated that PICA in a large honeycomb is manufacturable, and that thermal performance for the dual pulse environment is predictable. The pre-test simulations of the arc jet tests demonstrate that the FIAT model [25] predicts the thermal performance of the PICA atop LI-900 amazingly well for the dual, constant, heat pulse arc jet conditions that simulate the real dual-heat-pulse flight case. Predictions of recession and time for burn-through for both the first and second heat pulses are accurate to within a second of those observed. Importantly, charred PICA from the first pulse, performed beautifully, as predicted for the second, out-of-orbit heat pulse. Four-point positive and negative flexural tests of PICA atop LI-900 in  $\sim 5 \text{ cm}$  honeycomb showed encouraging results [27] for test articles fabricated on an aluminum substrate.

Two caveats are made here: (1) As shown in work by the Orion TPS ADP, PICA recession at heat rates below  $50 \text{ W/cm}^2$  is not well predicted by FIAT as explained above. As with Orion, the low heating conditions will be experienced at the “tails” of the two flight heat pulses and (2) Fencing of the honeycomb at low heat fluxes may be an issue, requiring testing and refinement of the phenolic impregnated fiberglass honeycomb. The technology for this test series represents the first formulation of the new honeycomb technology [27].



**Figure 57. Post tested model at the IHF run condition - Post tested model after 75 second entry in the IHF**

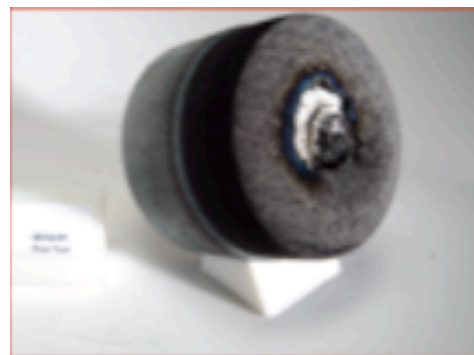


**Figure 58. Post tested model at the IHF run condition - Burned-through model after and overtest of 107 seconds at the IHF condition showing a failure mode of the dual layer PICA atop LI-900 TPS concept**

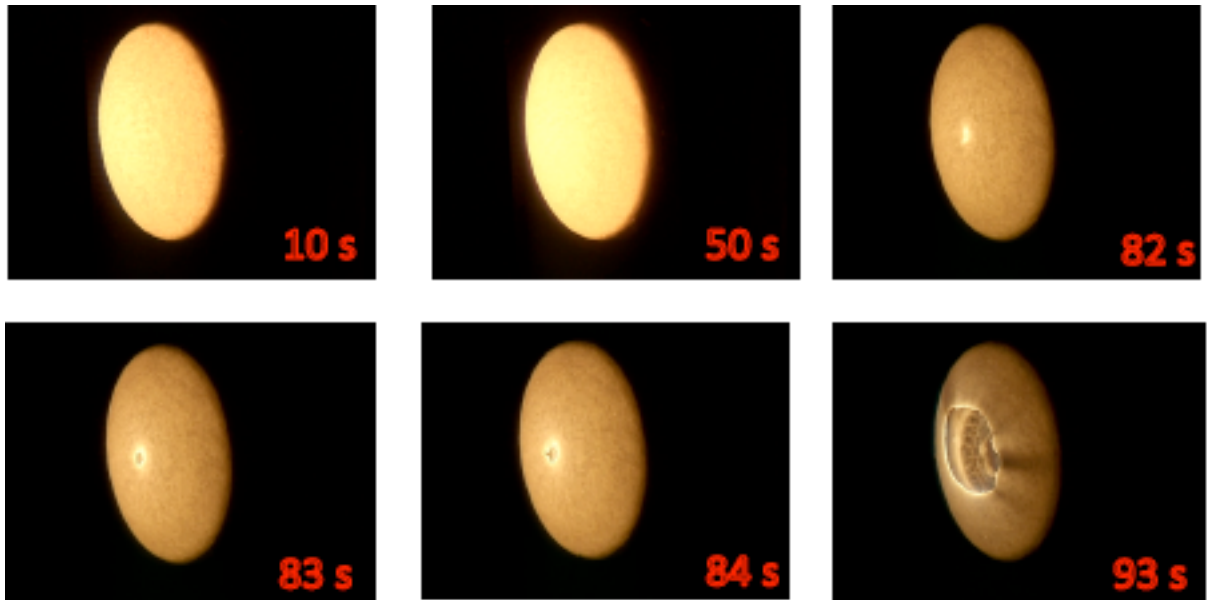


Figure 59. : Clips from a movie taken during the second heat pulse simulating entry from out-of-Mars orbit after aerocapture

## 7.2 IAD Controllability

HIAD structural mass models were developed for zero angle of attack and zero bank angle rates. In order to assess the HIAD concepts, the EDL-SA project initiated a contract with the Computational Fluid Dynamic Research Corporation (CFDRC) [47] to perform high-fidelity analysis of several HIAD configurations at nominal bank angle maneuver rate of  $5 \text{ deg/s}^2$ . The primary objective was to perform computational aero-structural simulations to support the EDL-SA assessments of IAD controllability and structural integrity during EDL. Analyses were performed with various design parameters, and the initial results indicate that the Von Mises stress levels on the gores and toroids remained below the material yield stresses with a comfortable margin.

## 8 Technology Investment Recommendations

The purpose of the first year of the EDL-SA task was to identify the Entry, Descent and Landing (EDL) technology investments that NASA needs to make in order to successfully land large payloads at Mars for both robotic and human-scale missions. The primary effort was focused on improving models of those missions, including mass, TPS, structural, guidance, and propulsion. The models were incorporated into aerocapture and EDL simulations to assess the overall effects on performance. Following are some key recommendations are made based on the results. A list of the TDP recommendations is provided in Table 26.

The lowest arrival mass is associated with use of deployable/inflatable decelerators. Rigid aeroshells offer a more traditional solution, despite a 35% arrival mass penalty compared with an inflatable decelerator. Supersonic retro-propulsion reduces the sensitivity to environmental variability compared with supersonic/subsonic aerodynamic decelerators. However, both inflatables and supersonic retro-propulsion need significant development before concerns about their controllability can be allayed. Precision landing requirements have never been demonstrated. Aerocapture is enabling (in the absence of NTR) and has never been demonstrated. The all-propulsive architecture warrants further investigation despite its 200%+ arrival mass penalty because of its high ratings on the Safety and Mission Success and Programmatic Risk FOMs. Moreover, significant engineering work will be needed to ensure reliable mechanisms are developed for transitioning between the system configurations during EDL.

An initial study for robotic-class missions showed that landing 1.5 mt at 0 km MOLA on Mars requires extension of current aerodynamic decelerator technology. Within the scope of parachute technology, a reefed, supersonic Ringsail parachute is the recommended option. However, a flight qualification program is required.

**Table 26. TDP Recommendations**

Technology Area	TDP Content
Rigid Aeroshells	Tools and processes for generating aero/aerothermal databases & mass models; rigid, dual heat-pulse capable TPS; structures; rigid aeroshell shapes for aerodynamic performance and controllability
Supersonic Retro-Propulsion	Aero-propulsion interaction propulsion for supersonic deceleration—tools, controls, and configurations. Works for high supersonic initiation through touchdown.
Deployable/Inflatable Decelerators	Tools & processes for generating aero/aerothermal databases & mass models for flexible entry/aerocapture vehicles; flexible HIAD materials, including flexible ablators and insulators, flexible aeroshell shapes for aerodynamic performance, structural strength and controllability
Precision Landing	Sensors, navigation and controls and their integration for precision landings with hazard avoidance in atmospheres
All-propulsive Aerocapture Development	System studies of open issues for hypersonic phase and staging
Supersonic Retro-Propulsion Flight Test Program	Requirements for an Aerocapture Technology Validation Flight Test Flight demonstration (TRL=6) of controllability from initiation to simulated touchdown of supersonic retro-propulsion descent system.
Deployable/Inflatable Decelerator Flight Test Program	Flight demonstration (TRL=6), including controllability of Deployable, Inflatable Aerodynamic Decelerator
Aerocapture Flight Test	Flight demonstration (TRL=6–7) in upper Earth atmosphere
Parachute Flight Test Program	Flight testing of a supersonic Ringsail parachute, including reefing and deployment of a large (>21.5 m diameter) parachute at Mach >2.0

## 9 Exploration-Class Study Open Issues

There is no shortage of additional work that could be done on the Exploration-class study. These can be placed in three broad categories—increased fidelity of the models and simulations, additional trade studies, and alternative Figures of Merit.

Clearly, greater fidelity in the component models would reduce the uncertainty in the simulation output, but a systematic uncertainty analysis should first be applied to determine which component models are responsible for the greatest uncertainty in the results. Even though substantial refinements were made in the mass models post-EPR, this is probably the one model whose further refinement would most increase the credibility of the results. At the simulation level, the biggest gap is the development of realistic flight system configurations, especially for the transition events.

Of the various additional work that might provide further discrimination between technologies, the following were recommended by the EPR:

- Compare the development costs of a packaging and inflation of a very large HIAD with low heating and no thermal protection technology development to a small one with a flexible ablative TPS development.
- Determine the areal density at which the HIAD no longer useful.
- Develop and document breakpoints for each of the technologies and the associated TRL/development risk at each breakpoint, as a means to help discriminate between options and architectural paths.
- Investigate on-orbit assembly of a rigid aeroshell and rigid deployable concepts to compare to the HIAD and slender-body aeroshells.
- Define L/D breakpoints for hypersonic system. Determine the minimum L/D required for the flight systems. Identify advantages of L/D's in the range of  $\sim 0.8$  to 1.
- Consider the use of control surfaces on both the rigid and non-rigid systems.
- Consider approaches in which the 80 mt are placed on the surface by more than 2 EDL systems. Assess how this trade affects technology development risk. Consider options in which a single EDL system is developed to land 80/x mt (where x is the # of landings) and options in which multiple systems are developed (perhaps one 40 mt lander and either two 20 mt landers or four 10 mt landers).
- The proposed 3-g limit may provide information sufficient for a relative comparison of selected architectures; however, in future studies consider include higher g-load sensitivity analyses in order to assess a more realistic benefit of each decelerator technology.
- Consider a more detailed failure mode based assessment for each technology to inform programmatic risk, development cost, and the reliability metrics used in the FOM assessment including considerations of margins, performance overlap at staging interfaces and lack of sensitivity to component performance uncertainties and increases in payload
- Consider performance metrics specifically tailored to the function of each technology (i.e.  $\Delta V$  normalized by component mass for decelerators)
- Develop detailed models of the separation of each drag device from the descent stage.
- Perform a detailed packing analysis and a subsequent update to the mass models used for each technology and subsystem and to consider deorbit from a 500 km circular orbit.

## 10 Large Robotic-Class Study

Future robotic missions to Mars are expected to require payload masses on the order of one to two metric tons. Thus far, robotic missions to Mars have used heritage from the deceleration technologies developed during the Viking era in the 1960s. The payload mass on the Viking landers was 590 kg. Every Mars mission after Viking has implemented incremental performance enhancements in aeroshell and parachute designs to obtain modest increases in landed mass. However, the Mars Science Laboratory (MSL), a mission using an Atlas V to deliver payload of 950 kg pushes the limits of the Viking decelerator technology (a 21.5 m parachute deployed at Mach ~2.3). Therefore, future robotic missions attempting to land payloads larger than 1 mt on Mars must extrapolate the current decelerator technology beyond the tested and validated flight regime and invest in a new, costly technology development program.

The robotic-class system analysis performed in this document focused on delivering 1500 kg to the surface of Mars using various parachute designs on an MSL-like entry vehicle. The parachute type, size, and number were varied to achieve the desired payload performance. To minimize the parachute design modifications from current technology, the MSL entry capsule's lift-to-drag ratio was increased from 0.24 to 0.3 by increasing the angle of attack during the entry phase to taking advantage of the high heat tolerant properties of the PICA heatshield. Single-stage, two-stage, and unreefed and reefed parachutes were explored for two different parachute types, the Disk Gap Band (DGB) and Ringsail. In addition, a systems engineering analysis was performed to assess the ability of the current 4.5 m MSL aeroshell to adequately package a 1500 kg payload. A complete overview of the ground rules and assumptions for the study can be found in Appendix A.

A survey of past test flights was performed to determine the aerodynamic modeling for each parachute design. The current MSL parachute is a 21.5 m diameter DGB but a Ringsail design is known to exceed DGB performance in the subsonic flight regime. Although popular for subsonic applications, a Ringsail parachute had only a few supersonic flight tests, making the determination of its supersonic aerodynamic characteristics difficult. Ultimately, a Ringsail model was adopted for use in this study. A reefed parachute is a parachute or cluster of parachutes that opens in stages to improve the probability of a successful deployment especially with large diameter designs. Since it was expected that parachutes significantly larger than 21.5 m would be required to land a 1500 kg payload, a reefed chute design option was selected.

### 10.1 Packaging Feasibility

Mass scaling equations were used to scale the structural elements of the MSL-type configuration for each point design. An additional 30% contingency was applied based on JPL design principles. It was determined that the packing density resulting from integrating the 1500 kg payload into the MSL 4.5 m aeroshell was exceedingly large. The only recourse was to increase the aeroshell diameter to 4.7 m, which still complied with ground and launch vehicle restrictions. In addition, the number of engines on the MSL descent stage would have to increase from 8 to 12 in order to maintain control authority similar to that of MSL during the powered descent phase. Finally, an additional 300 kg of propellant (700 kg total) was required to land the larger payload mass. The Apollo entry guidance [23] was used to steer the vehicle to the landing site.

### 10.2 Parachutes

The parachute type, size, and number were varied to achieve the desired payload performance. Figure 60 shows each parachute configuration considered for this study: single-stage, two-stage, and reefed

parachutes. Each parachute arrangement was studied for two different parachute types: Disk-Gap-Band (DGB) and Ringsail. Models derived from flight test data for the DGB parachute were used for this study[37].

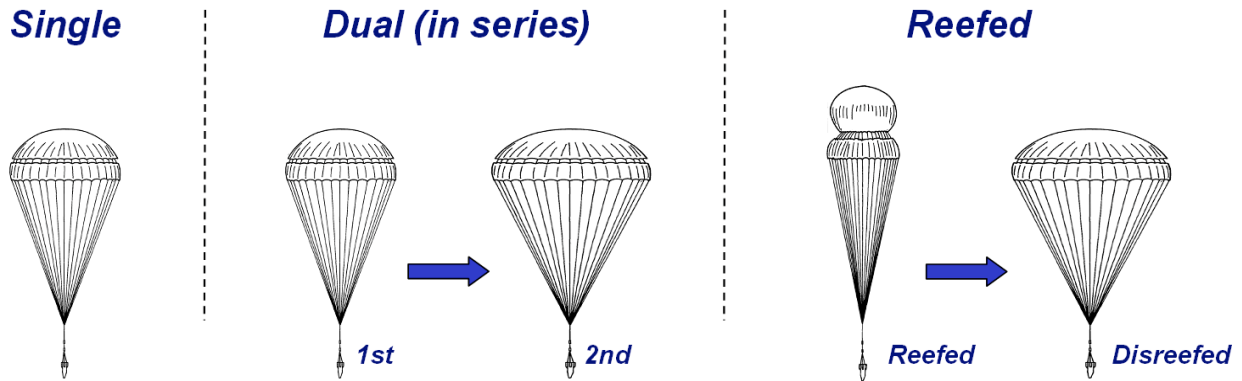


**Figure 60. Parachute systems considered. The systems were implemented using DGB or ringsail parachutes (adapted from Ref. NASA TN D-6469).**

### 10.2.1 Modeling Overview

This section provides a description of the parachute performance models used for the robotic-class mission analysis of the EDL-SA study. The Disk-Gap-Band parachute and a Ringsail parachute were evaluated for use in three different implementation strategies.

**Single-stage parachute system** - A single, large parachute is deployed at supersonic conditions and used to decelerate the entry vehicle to subsonic conditions. This is the parachute concept used by previous Mars missions with the exception that larger parachutes ( $D_0 > 21.5$  m) are deployed at higher Mach numbers (Mach  $> 2.1$ ) than have previously been employed at Mars.

**Two-stage parachute system** - A large ( $\sim 21.5$  m) parachute is deployed at supersonic conditions ( $\sim$  Mach 2.3) and used to decelerate the vehicle to lower supersonic conditions ( $\sim$  Mach 1.5). At that point, a second, larger parachute of the same type (i.e. DGB or Ringsail) is deployed by the first parachute and used to decelerate the vehicle to subsonic conditions. This approach essentially uses the first parachute as a very large pilot parachute.

**Reefed parachute** - A single, large parachute is deployed in a reefed state at supersonic conditions ( $\sim$  Mach 2.3). The parachute is disreefed at a lower Mach number and used to decelerate the vehicle to subsonic conditions.

Each of the parachute arrangements described above utilize a set of performance models to simulate their behavior during deployment and descent. The performance models are of two types: those that simulate deployment and those that simulate drag performance. The equations and inputs used for each model type are described in subsequent sections.

### 10.2.2 Deployment Modeling

**Time to inflation initiation** - The deployment sequence is considered as two separate events: deployment initiation ( $t_0$ ) to inflation initiation ( $t_{SI}$ ) and inflation initiation to full inflation ( $t_{FI}$ ). For the case of the single-stage parachute, the reefed parachute, and the first stage of the two-stage parachute, deployment initiation corresponds to the moment of mortar fire. For the second stage of the two-stage parachute, deployment initiation corresponds to the moment when the first stage parachute begins to extract the second parachute.

The time duration between deployment initiation and inflation initiation is estimated as being the time required for the parachute bag to travel a given distance  $d$ . With the exception of the second stage parachute, this time is calculated from an assumed mortar velocity  $v_m$  as follows:

$$t_{SI} - t_0 = \frac{d}{v_m}$$

The distance  $d$  was selected to be 10 times the diameter of the entry vehicle, or 47 m. The mortar velocity was assumed to be 35 m/sec. These values yield a time from mortar fire to inflation initiation of 1.343 seconds.

In the case of the second stage parachute, an estimate of the parachute extraction time is calculated by considering the difference in ballistic coefficients between the entry vehicle and the first stage parachute as follows:

$$t_{SI} - t_0 = \sqrt{\frac{2d}{g_z \left[ \left( \frac{C_D A}{m} \right)_{EV} - \frac{(C_{D_0} S_0)_{P_1}}{m_{P_1} + m_{P_2}} \right]}}$$

Using the equation above and data from an initial set of Monte Carlo trajectories, estimates of the  $t_{SI} - t_0$  values were calculated and were seen to fall between approximately 0.6 and 0.85 seconds. The final set of trajectories utilized a more conservative value of 1.0 second.

**Time to full inflation** - Following inflation initiation the parachute undergoes a growth in area until reaching its maximum value of  $S_0$ . The time required for this to occur,  $t_{inf}$ , is estimated using the following relation:

$$t_{inf} = t_{FI} - t_{SI} = K_{inf} D_0 \quad 7$$

For DGB parachutes, a value of the inflation factor  $K_{inf}$  of 0.02 sec/m was used. An estimate for the  $K_{inf}$  value for a supersonic Ringsail parachute was developed based on flight data from three separate tests. Those data are summarized below.

**Table 27. Summary of supersonic ringsail parachute inflation times**

$D_0$ (m)	$t_{inf}^*$ (sec)	$K_{inf}$ (sec/m)	Reference
9.51	0.36	0.03785	[38]
16.6	0.63	0.03795	[39]
12.2	0.75	0.06148	[40]

\* $t_{inf}$  is measured from line stretch to peak load

Averaging the three calculated values of  $K_{inf}$  shown in Table 27 yields a value of 0.04576 sec/m, which was subsequently used during analysis.

**Parachute Area Growth** - During the inflation process the parachute is undergoing a rapid growth in size. The growth in parachute diameter is modeled as occurring linearly with time, in a manner similar to Equation 7. This yields the following relation for the ratio of parachute area to nominal area as a function of time.

$$\frac{S}{S_0} = \frac{1}{D_0} \left( \frac{t - t_{SI}}{K_{inf}} \right)^2 \quad 8$$

During initial deployment of a single stage, or first stage parachute the parachute area,  $S$ , grows from a value of 0 to a value of  $S_0$  within time  $t_{inf}$ . During initial deployment of a reefed parachute, the parachute is considered to inflate to its targeted value of canopy area,  $S_R$ . Disreefing is set to occur at a fixed time,  $t_{dr}$ , after mortar deployment. Based on early Monte Carlo runs, a value of 9.55 seconds for  $t_{dr}$ , was used. Area growth during disreefing is modeled as before, using Equation 8.

**Parachute Peak Loads** - The peak loads occurring during parachute inflation are calculated using a one-equation method provided in [41]. The equation is as follows:

$$F_p = C_{D_0} S_0 q_\infty C_x \quad 9$$

Where  $q_\infty$  is the dynamic pressure at the start of inflation or disreefing, and  $C_x$  is the opening force coefficient. For the DGB parachute, a  $C_x$  value of 1.456 was used based on models used for the Mars Science Laboratory simulations. For the Ringsail parachute, a  $C_x$  value of 1.1 was used based on examination of the available supersonic flight data and data provided in [41]. In particular, deriving a value of  $C_x$  from the available supersonic flight data yielded values of 1.0619, 1.0725, and 2.1610 while [41] suggested a value of 1.1 based on subsonic flight data. The large  $C_x$  value of 2.1610 was discounted due to the difficulty in extracting a  $C_x$  value from the published data set.

### 10.2.3 Parachute Drag Performance

Modeling of the parachute drag performance was done using two different  $C_{D0}$  vs. Mach performance curves for each parachute type, a low drag curve and a high drag curve. The low drag curve was used to size the parachute while the high drag curve was used during calculation of the peak opening loads.

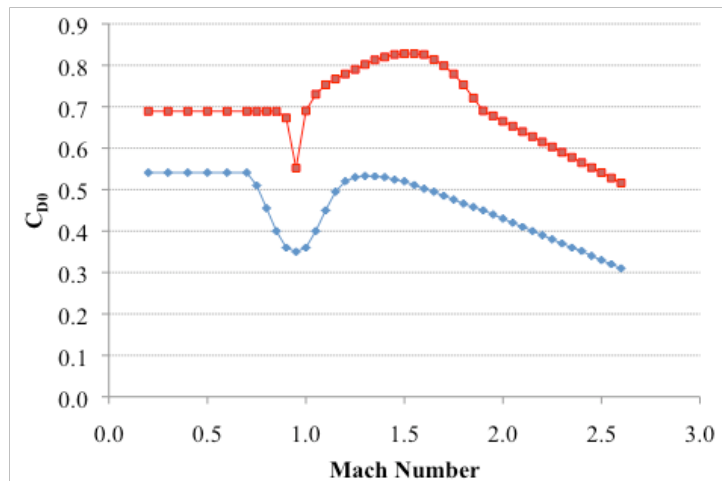


Figure 61. High and Low Drag Coefficient Curves Used for DGB Modeling

**DGB Nominal Drag Performance** - Disk-Gap-Band parachutes have been successfully deployed on several Mars missions. A relative extensive database of drag versus Mach performance has been acquired through several Earth-based flight tests and wind tunnel tests [37] [42]. Thus, there is a strong precedent for modeling the performance of a supersonic DGB parachute that was drawn on for the present study. In particular, the drag coefficient vs. Mach models used for modeling Mars Science Laboratory trajectories was used. The high and low drag performance curves are shown in Figure 61.

**Ringsail Nominal Drag Performance** - Modeling of the performance of a supersonic Ringsail parachute was considerably more difficult than for the DGB due to the lack of historical data. Specifically, only four successful supersonic flight tests (out of five attempts) of a Ringsail parachute

have taken place and those are over a limited range in Mach numbers. A summary of the deployment conditions for the flight tests is provided in Table 28. A summary of the available flight test data is shown in Figure 62. Also provided in Figure 62 are explanations of many of the phenomena observed in the data, as they are described in the references. From this data, high and low drag performance curves were established. These curves are shown in Figure 63. The shape of the curves was designed to roughly mimic that of the DGB curves in Figure 61. Specifically, the inclusion of a decrease in the drag performance around a Mach number of 1.0 was based on a similar trend for DGB parachutes. For the low drag curve, the supersonic performance was based on the data from [40]. It is worth noting that the Ringsail configuration used during all 5 supersonic tests is somewhat different than that typically used for subsonic applications, and as a result the subsonic performance was quite low [43]. Therefore, it was assumed that a modern day application of a supersonic Ringsail parachute would employ considerable modifications to the design used in prior testing. Thus, the supersonic performance seen in [40] was considered to be a lower bound. The subsonic performance seen in the four successful flight tests was discounted and the lower drag model instead used a more typical Ringsail subsonic drag coefficient of 0.85. The higher drag model assumed an approximately two times increase in drag coefficient at higher Mach numbers.

**Table 28. Summary of Supersonic Ringsail Test Conditions**

$D_0$ (m)	Deploy Mach	Deploy $q_\infty$ (Pa)	Comments	Reference
26.0	1.15	280	Deployed in reefed state with large fluctuations, disreefed at ~Mach 0.8, initially inflated behind blunt body	[44] [45]
9.51	1.39	527	Slight flutter in skirt after opening, minor damage during deployment	[38] [45]
12.2	1.64	436	Full inflation never achieved, failure attributed to excessive geometric porosity of crown	[46] [45]
16.6	1.61	555	Minor damage due to drogue bag recontact, initially inflated behind blunt body	[39] [45]
12.2	2.95	440	Large areal oscillations until ~Mach 1.5, minor canopy damage due to parachute bag and mortar lid recontact	[40]

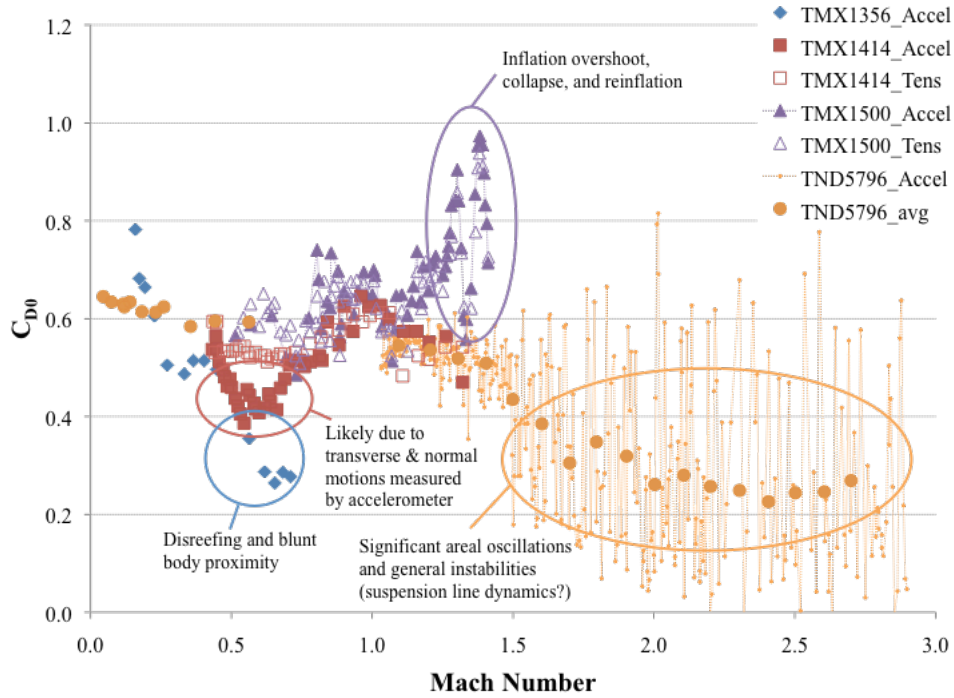


**Figure 62. Summary of supersonic ringsail flight test drag data. Note: Caption refers to NASA technical document references and whether the data was derived from accelerometer or tensiometer measurements.**

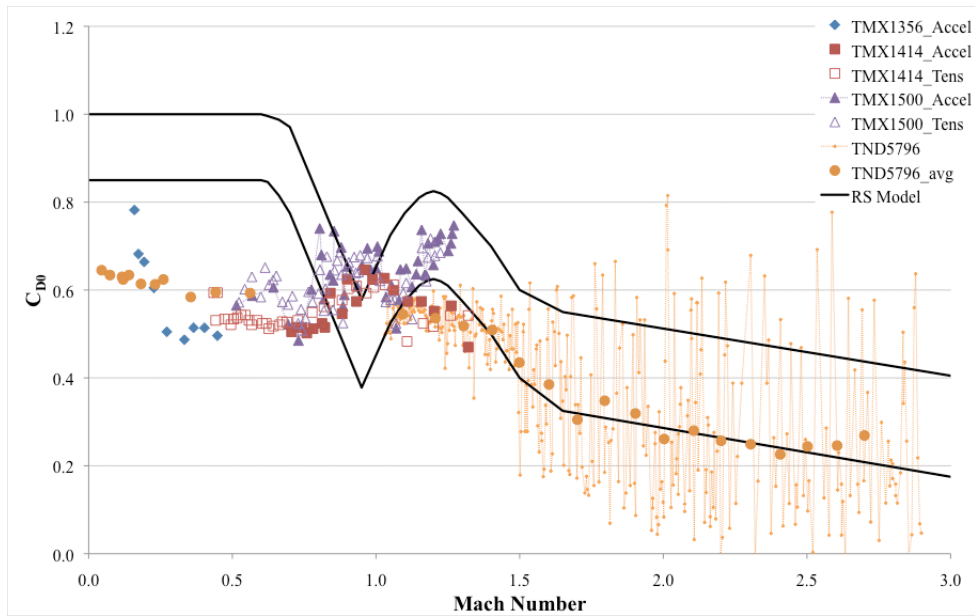


**Figure 63. Summary of supersonic ringsail flight test data along with high and low drag performance models. Note: Label text refers to NASA technical document numbers from which the data originated.**

**Reefed Parachute Performance** - Performance of reefed parachutes used the same drag curves as the unreefed parachutes. However, the DGB parachute was scaled by a factor of 0.42, while the Ringsail used a scale factor of 0.784.

### 10.3 Monte Carlo Simulation Results

The parachute solutions in Table 29 were computed using 8000 Monte Carlo simulations. Dispersions in aerodynamics, atmospheric density, winds as well as attitude error and off-nominal entry conditions were introduced in the 8000 simulations. A description of the dispersions can be found in Appendix A. The configuration in Table 29 is considered feasible if the timeline margin is greater than 15 s. The timeline margin is the time between radar acquisition and descent stage ignition at two km above ground level (10s of radar operation to guarantee altitude solution plus 5 s for engine priming). The diameters shown in Table 29 are the minimum diameters required to obtain feasible solutions (i.e., solutions with timeline margin >15s) in the Monte Carlo simulations. Figure 64 shows data from a Monte Carlo simulation using the reefed parachute configuration. Note how the  $3\sigma$  high for parachute deploy Mach is less than 2.5.

**Table 29. Supersonic parachute performance results.**  
Parachute deploy Mach numbers correspond to  $3\sigma$  high values

Parachute		DGB		Ringsail	
<b>Single Parachute</b>					
Diameter (m)		32.5		31.5	
Deploy Mach		2.5		2.5	
<b>Two-stage Parachute</b>					
1 <sup>st</sup> Diameter (m)	2 <sup>nd</sup> Diameter (m)	21.5	41.5	21.5	41.0
1 <sup>st</sup> Deploy Mach	2 <sup>nd</sup> Deploy Mach	2.5	1.5	2.5	1.5
<b>Reefed Parachute</b>					
Reefed Diameter (m)	Disreefed Diameter (m)	21.5	>34.0	21.5	34.0
Reefed Deploy Mach	Disreefed Deploy Mach	2.5	2.0	2.5	2.0

In Table 29, the single and two-stage parachute solutions have lower probability of success due to the large loads. The single parachute configuration is deployed at  $\text{Mach} \leq 2.5$ , and the diameters needed to land 1500 kg are 32.5 m and 31.5 m for the DGB and Ringsail parachute types respectively. The diameter of the first parachute in the two-stage parachute configuration is held constant to 21.5 m (i.e., to maintain MSL heritage) and is deployed at  $\text{Mach} \leq 2.5$ . The second chute in the two-stage parachute configuration is deployed at  $\text{Mach} \leq 1.5$  and the diameters of the second chutes are 41.5 m and 41 m for DGB and Ringsail respectively. As seen in Table 29, the diameter for a reefed Ringsail parachute configuration is 34 m. The DGB reefed parachute diameter will be larger than 34 m since the aerodynamic performance of a reefed DGB parachute is worse than that of a reefed Ringsail parachute.

All parachute solutions in Table 29 are capable of landing 1500 to the surface of Mars using a scaled MSL-type vehicle. Given the certain investment in a flight test, the recommended technology that shows the most promise for success and ultimate capability is a single 34 m reefed supersonic Ringsail. Reefing adds an element of stability, which enables larger diameters over an unreefed parachute. Other notable advantages of using the reefed Ringsail parachute include reduced mass and complexity while increasing flexibility to tailor the drag deceleration as needed. Also the 34 m reefed supersonic ringsail is considered to be at TRL-4 today.

Specific parameters for the recommended reefed parachute configuration are shown in Table 30 below. Also, Table 31 compares this reefed chute configuration with MSL.

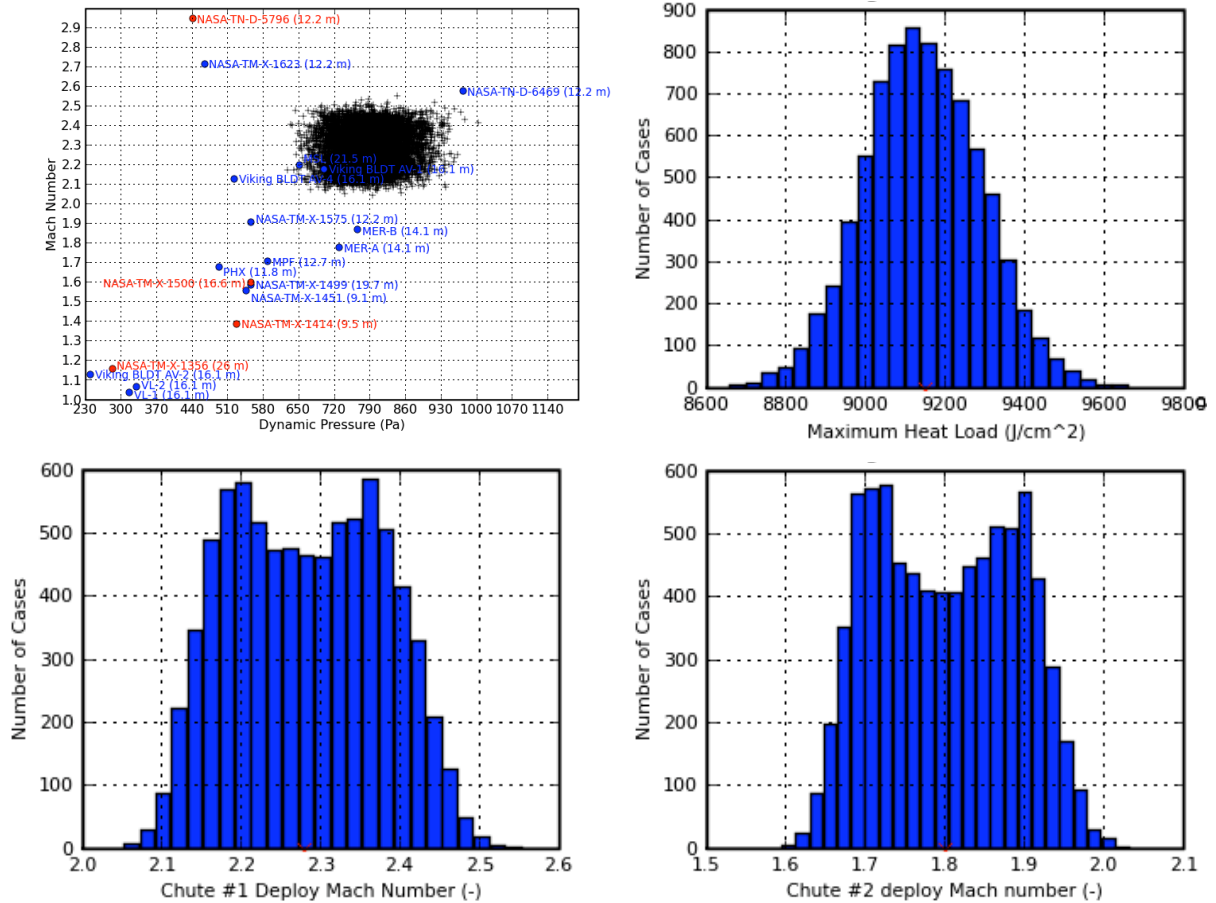


Figure 64. Monte Carlo simulation results using 8000 dispersed cases for the reefed parachute configuration.

Table 30. Supersonic reefed parachute performance results.  
Chute deploy Mach numbers correspond to 3σ high values.

Parameter	Value	Comments
Entry Mass	5604 kg	~2 mt heavier than MSL
Entry Lift-to-Drag Ratio	0.3	Heating, stability and packaging issues still need to be analyzed
Peak g-load	13 g's	MSL typically ≤ 15g's
Peak Heat Load	9600 J/cm <sup>2</sup>	MSL typically ≤ 6200 J/cm <sup>2</sup>
Parachute Deployment Mach # (nominal; 3-sigma high = ~2.5)	2.28	No new technology but flight test required
Reefed Diameter	21.5 m	No new technology but flight test required
Disreef Mach #	1.8 (2.0)	No new technology but flight test required

nominal (3-sigma high)		
Disreefed Diameter	34 m	No new technology but flight test required
Number of Descent Engines	12	4 additional engines over MSL. More engines required for $2 \leq T/W \leq 3$
Engine Characteristics	3046.9 N/eng 220s Isp	MSL engine characteristics
Time Between Radar Acquisition and Ignition	15.6 s	Meets 15s minimum requirement
Total Propellant Load	624.0 kg	225 kg additional propellant over MSL

**Table 31. Comparison of MSL and the scaled reefed ringsail configuration.**

Sub-System	MSL*	Scaled Reefed Ringsail Configuration**
Entry Mass	3350 kg	5600 kg
Aeroshell Diameter	4.5 m	4.7 m
Parachute	DGB 21.5 m	Reefed Ringsail 21.5 m / 34 m
Parachute Deploy Mach	$\leq 2.3$	$\leq 2.5$
Lift-to-drag ratio	0.24	0.30
Number of MLEs	8	12
Propellant	400 kg	625 kg
Time on Radar	>20 s	>15 s
Rover Mass	900 kg	1500 kg
Launch Vehicle	Atlas V (541)	Delta IV-Heavy

\* Masses of MSL obtained from MEL 08/15/2008

\*\*Applied a post-scaling factor of 30% to all sub-systems since design is appreciably different from MSL

#### 10.4 Robotic Class Summary

Single, two-stage and reefed parachutes capable of landing 1.5 mt at 0 km MOLA were explored in this study. All parachute solutions require supersonic high altitude BLDT (Balloon Launched Decelerator Test). The Monte Carlo results in this document indicate that a single 34 m reefed supersonic Ringsail is the most promising configuration.

## 11 Bibliography

1. "NASA Entry, Descent and Landing Competencies, Program Decision Memorandum," s.l. : AMO OCE Issue #3, Aug. 19, 2008 (Unpublished).
2. "Entry, Descent and Landing Long Term Capability Requirements Evaluation Terms of Reference (TOR)," s.l. : Office of the Chief Engineer Memorandum, Oct, 2008 (Unpublished).
3. Drake, B. G., editor., "Human Exploration of Mars Design Reference Architecture 5.0," s.l. : NASA-SP-2009-566, July 2009.
4. Eldred, L. B., "HSLoad - Input Deck Documentation," NASA LaRC SAMS Contract No. NAS1-00135 03RAA, Swales Aerospace Corporation. 5/28/2003.
5. MIAS Design Reference Report, Astrium GmbH, MIAS-RIBPRE-RP-0002, Dec. 4, 2002 (Unpublished).
6. Structural Design and Test Factors of Safety for Spaceflight Hardware, NASA-STD-5001A, August 5, 2008.
7. Brown, G. J., "Inflatable Structures for Deployable Aerocapture Decelerators," Proceedings of JANNAF Conference, 2005.
8. Brown, C. D., "Elements of Spacecraft Design," American Institute of Aeronautics & Astronautics, April 2003.
9. Komar, D.R., Hoffman, J., and Olds, A., "Framework for the Parametric System Modeling of Space Exploration Architectures," AIAA-2008-7845, 2008.
10. Heinemann, W., "Design Mass Properties II: Mass Estimating and Forecasting for Aerospace Vehicles Based on Historical Data," JSC-26098, November 1994.
11. Kinney, D.J., "Aero-Thermodynamics for Conceptual Design", AIAA-2004-13382, January 2004.
12. Wright, M., Loomis, M., and Papadopoulos, P., "Aerothermal Analysis of the Project Fire II Afterbody Flow," Journal of Thermophysics and Heat Transfer, Vol. 17, No. 2, 2003, pp. 240-249.
13. Wright, M., Candler, G., and Bose, D., "Data-Parallel Line Relaxation Method for the Navier-Stokes Equations," AIAA Journal, Vol. 36, No. 9, 1998, pp. 1603-1609.
14. Gnoffo, P. A., Gupta, R. N., and Shinn, J., "Conservation Equations and Physical Models for Hypersonic Air Flows in Thermal and Chemical Nonequilibrium," NASA TP 2867, 1989.
15. Gnoffo, P. A., "An Upwind-Biased, Point-Implicit Relaxation Algorithm for Viscous, Compressible Perfect-Gas Flows," NASA TP 2953, 1990.
16. Whiting, E.E., Yen, L., Arnold, J. O., and Paterson, J.A., "NEQAIR96", Nonequilibrium and Equilibrium Radiative Transport and Spectra Program: User's Manual," NASA RP-1389, Dec. 1996.
17. Aftosmis, M., "3D Applications of Cartesian Grid Euler Method." AIAA 95-0853
18. Cerimele, C., Gamble, J., "A Simplified Guidance Algorithm for Lifting Aeroassist Orbital Transfer Vehicles," AIAA-85-0348, AIAA 23rd Aerospace Sciences Meeting, 1985.
19. Bryant, L., Tigges, M., and Ives, D., "Analytic Drag Control for Precision Landing and Aerocapture," AIAA-98-4572, 1998.
20. Rousseau, S., Perot, E., Graves, C., Masciarelli, J., and Queen, E., "Aerocapture Guidance Algorithm

- Comparison Campaign,” AIAA-2002-4822, 2002.
21. Masciarelli, J., Rousseau, S., Fraysse, H., and Perot, E. “An Analytic Aerocapture Guidance Algorithm for the Mars Sample Return Orbiter,” AIAA-2000-4116, 2000.
  22. Powell, Richard W., “Numerical Roll Reversal Predictor Corrector Aerocapture and Precision Landing Guidance Algorithms for the Mars Surveyor Program 2001 Missions,” AIAA 1998.
  23. Moseley, P. E., “The Apollo Entry Guidance: A Review of the Mathematical Development and Its Operational Characteristics,” TRW Note No. 69-FMT-791, TRW, December 1, 1969.
  24. Sostaric, R. R. and Rea, J. R., “Powered Descent Guidance Methods For The Moon and Mars,” AIAA 2005-6287, 2005.
  25. Chen, Y. K. and Milos, F. S., “Ablation and Thermal Response Program for Spacecraft Heatshield Analysis,” Journal of Spacecraft and Rockets, Vol. 36, No. 3, 1999, Pp. 475-483.
  26. Wright, M. J., “Mars EDL/SA Thermal Protection System (TPS) Margin Management Plan, Rev V2,” June 09, 2009, NASA Ames Research Center (Unpublished).
  27. Congdon, W. M., “Development of Design and Production Processes for a Block-Ablator Heatshield with Preliminary Test Results,” International Planetary Probe Workshop, Barcelona Spain, June 12-18, 2010.
  28. Powell, R. W., Striepe, S. A., Desai, P. N., Queen, E. M., Tartabini, P. V., Brauer, G.L., Cornick, D. E., Olson, D. W., Petersen, F. M., Stevenson, R., Engle, M. C., and Marsh, S. M., “Program to Optimize Simulated Trajectories (POST2), Vol. II Utilization Manual.” Version 1.1.1G, May 2000.
  29. Justus, C. G. and Johnson, D. L., “Mars Global Reference Atmospheric Model 2001 Version (MarsGRAM 2001): Users Guide” NASA TM 2001-210961 April 2001
  30. Kumar, "Issues on Human Acceleration Tolerance After Long-Duration Space Flights" NASA Technical Memo 104753, Oct 1992.
  31. Finley, P. J., "The Flow of a Jet from Body Opposing a Supersonic Free Stream," Journal of Fluid Mechanics, Vol. 26, No. 2, 1966, pp. 337-368.
  32. Kirvanek, T. and Lepsch, R., GRC Ares V Shroud Studies, September 22, 2009. (Unpublished)
  33. Hughes, W.O., and McNelis, “Acoustic Testing of the Cassini Spacecraft and Titan IV Payload Faring”, NASA TM 107474, 67<sup>th</sup> Shock and Vibration Conference, Monterey, CA. November, 18-22, 1996.
  34. Zell, P. T., “The Block-Ablator in a Honeycomb Heatshield Architecture,” International Planetary Probe Workshop, Barcelona Spain, June 12-18, 2010.
  35. Personal communication, M. Blosser and C. Poteet, LaRC. (Unpublished)
  36. Mendeck, G. F. and Carman, G. L., “Guidance Design for Mars Smart Landers Using The Entry Terminal Point Controller,” AIAA 2002-4502 Atmospheric Flight Mechanics Conference and Exhibit, Monterey, CA, August 2002.
  37. Bendura et al., “Flight Tests of Viking Parachute System in Three Mach Number Regimes II: Parachute Test Results,” NASA Technical Note TN D-7734, 1974.
  38. Preisser et al., “Flight Test of a 31.2-Foot-Diameter Modified Ringsail Parachute Deployed at a Mach Number of 1.39 and a Dynamic Pressure of 11.0 Pounds Per Square Foot,” NASA Technical Memorandum TM X-1414, 1967.

39. Whitlock et al. "Performance of a 16.6-Meter-Diameter Modified Ringsail Parachute in a Simulated Martian Environment," NASA Technical Memorandum TM X-1500, 1968.
40. Eckstrom, C. V., "High-Altitude Flight Test of a 40-Foot-Diameter (12.2-Meter) Ringsail Parachute at a Deployment Mach Number of 2.95," NASA Technical Note TN D-5796, 1970.
41. Knacke, T. W., "Parachute Recovery Systems Design Manual," Naval Weapons Center Technical Publication NWC TP 6575, 1991.
42. Steinberg et al., "Development of the Viking Parachute Configuration by Wind Tunnel Test," AIAA Paper 1973-454, 1973.
43. Ewing, E. G., "Ringsail Parachute Design," Air Force Flight Dynamics Laboratory Technical Report AFFDL-TR-72-3, 1972.
44. Whitlock et al., "Performance of a 26-Meter-Diameter Ringsail Parachute in a Simulated Martian Environment," NASA Technical Memorandum TM X-1356, 1967.
45. Whitlock, C. H. and Bendura, R. J., "Inflation and Performance of Three Parachute Configurations From Supersonic Flight Tests in a Low-Density Environment," NASA Technical Note TN D-5296, 1969.
46. Eckstrom et al., "Flight Test of a 40-Foot-Nominal-Diameter Modified Ringsail Parachute Deployed at a Mach Number of 1.64 and a Dynamic Pressure of 9.1 Pounds Per Square Foot," NASA Technical Memorandum TM X-1484, 1967.
47. Sheta, E., Venugopalan, V., Tan, XG, Liever, P. and Habchi, S., "Aero-Structural Assessment of an Inflatable Aerodynamic Decelerator," CFDRC Report: 8927/6, April 2010 (CFD Research Corporation, Huntsville, AL)

## A Appendix A. DRMs, GR&As and FOMs

### A.1 Design Reference Missions

A Design Reference Mission (DRM) describes the objectives and top-level requirements for a representative future mission for the purposes of facilitating choices of architectures and technologies for a class of missions. The EDL-SA Study encompasses two such classes—Exploration Class missions and Large-Robotic Class missions. This section provides a summary of the respective DRMs for these two mission classes that will be used in the EDL-SA Study.

#### A.1.1 Exploration-Class Design Reference Mission

Figure A-1 illustrates the Exploration-class DRM used in the 2007 Mars Design Reference Architecture 5 study (“Human Exploration of Mars Design Reference Architecture 5.0”). For this architecture, pre-deployed assets are used—two large cargo vehicles arrive first, and are placed in orbit using propulsion or aerocapture. The vehicle carrying the Mars ascent vehicle undergoes EDL shortly thereafter, while the vehicle carrying the habitat lander remains in orbit. A crewed system arrives 2 years later, is propulsively captured into orbit, from which it rendezvous with the orbiting habitat lander. The habitat lander with the crew then undergoes EDL. This not only reduces the single EDL mass size, but also reduces the mission risk.

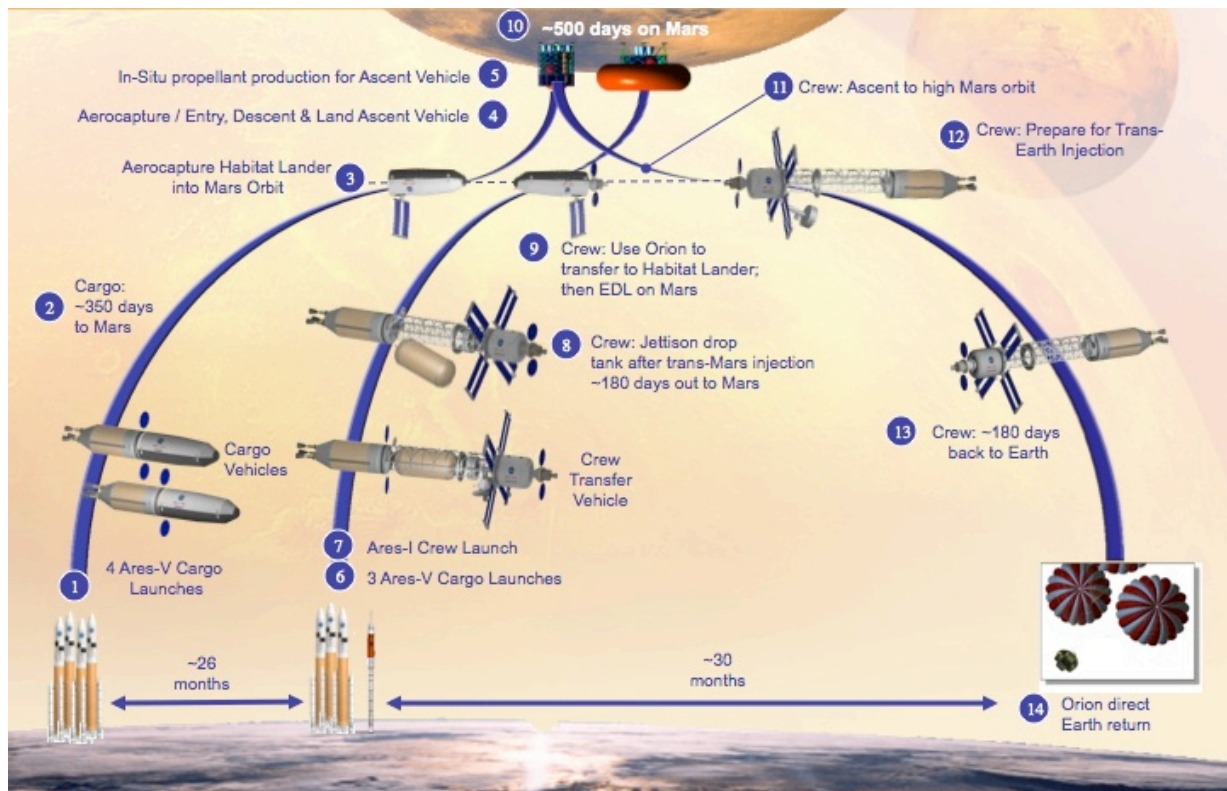


Figure A-1. Exploration-Class Design Reference Missions

Some of the key parameters of the systems for the overall architecture are provided in Table A-1 for both nuclear thermal rocket (NTR) and chemical propulsion options.

**Table A-1.Key Parameters for the Exploration-Class DRM**

<b>Parameter</b>	<b>NTR Reference</b>	<b>Chemical Option</b>
<b>Total Crew Flight Duration (approx. days) *</b>	<b>~900</b>	<b>~900</b>
Crew Transit time LEO-Mars (approx. days)	~180	~180
Crew Mars Stay Time (approx. days)	~540	~540
Crew Transit time Mars-Earth (approx. days)	~180	~180
<b>Total Initial MTV Mass in LEO (IMLEO) (t) **</b>	<b>825</b>	<b>1252</b>
Crew Vehicle Mass	333	534
Inter-Planetary Transportation (t)	282	483
Crew Transit Payload (t)	51	51
Cargo Vehicle Mass (mt each)	246	359
Inter-Planetary Transportation (t)	144	257
Mars Surface Payload (t)	36	36
Propulsive Lander (wet, t)	23	23
Aeroshell Mass (t)	43	43
<b>Launch Data †</b>		
Ares-I Launches (crew)	1	1
Ares-V Launches (cargo)	7-9	10-12
Launch Campaign Duration (days)	300	390

\* Trip times are average durations across the synodic cycle

\*\* All mass data exclusive of Project and Program reserves

† Number of launches dependent on launch vehicle selected

Figure A-2 illustrates the 3 Mars Transfer Vehicles (MTVs) needed for the NTR option. The two cargo landers embarking in the first landing cycle require two Ares V launches each. The crewed lander embarks on the second cycle; it requires three Ares V launches and one Ares I launch. For purposes of the EDL-SA Study, the Exploration-class DRM is the EDL portion (including the aerocapture phases) of that DRM (modified, as discussed below).

The aeroshell concept used in DRA5 for the Mars landers was a dual-use Ares V shroud, referred to as an ellipsoid. This is illustrated in Figure A-3. Further details on this DRM are available in the DRA 5 report (“Human Exploration of Mars Design Reference Architecture 5.0 Executive Summary”).

The particular DRM employed in the EDL-SA study is similar. The primary difference is the use of a more conservative margin policy. The details are given in Section A.2.4.

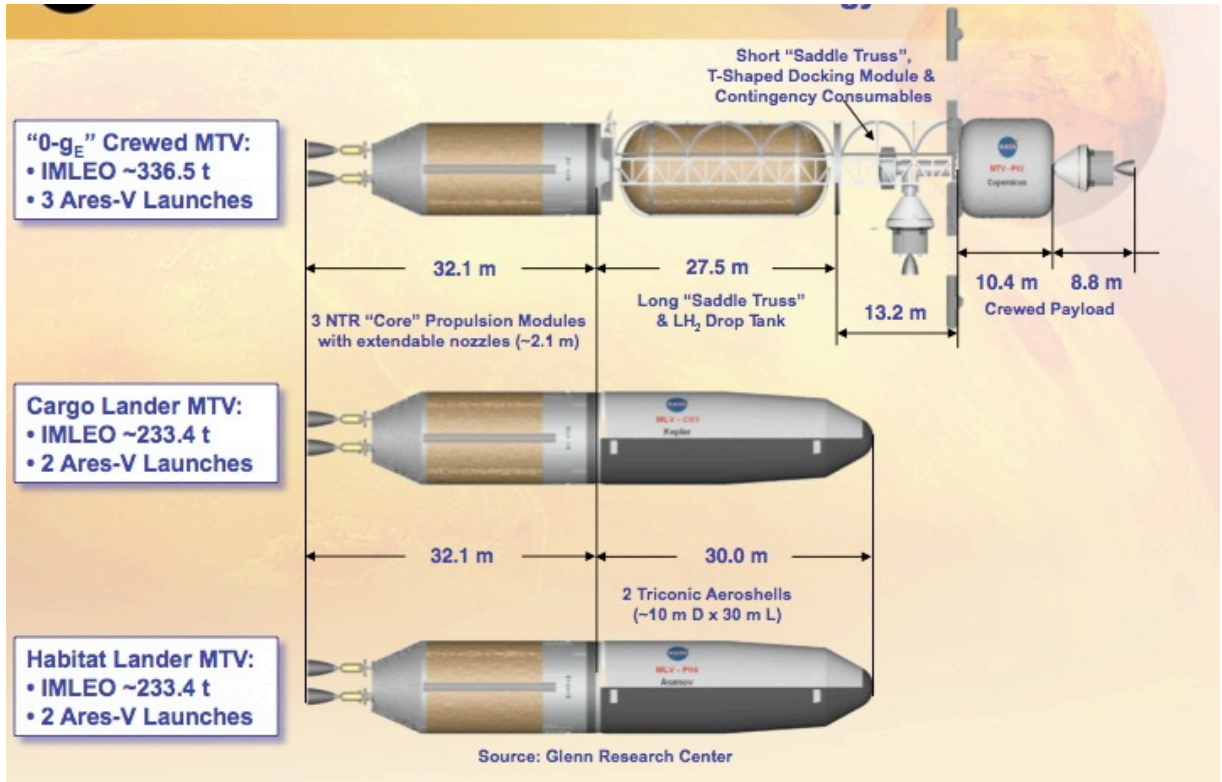


Figure A-2. Mars Transfer Vehicles

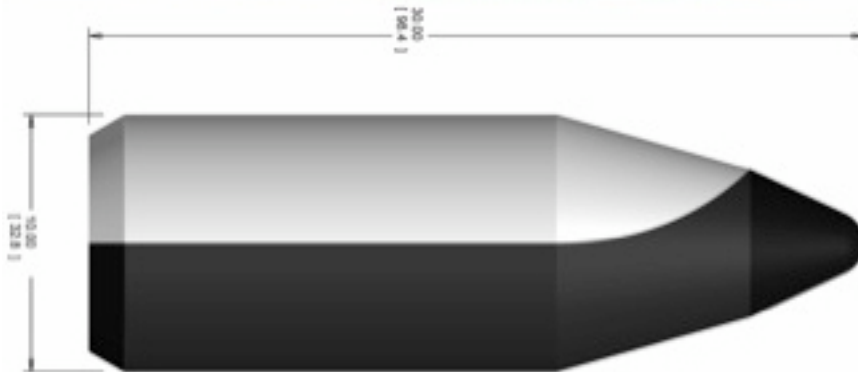


Figure A-3. Outer Mold Line of a Mars Lander Aeroshell

### A.1.2 A.1.2 Large-Robotic Class Reference Mission

The Large-Robotic-Class DRM to be used for the FY 09 robotic study has been designed to land an equivalent 1.5 metric ton payload on the surface of Mars using a scaled Mars Science Laboratory (MSL) configuration (see Figure A-4). A 1.5 metric ton payload configuration accommodates all the currently planned robotic missions to Mars within the next 20 years as well as utilizes technology that could be applied to future manned missions to Mars. This feed forward technology is embedded in the performance enhancements to the MSL design that enable more deceleration forces to be applied to the vehicle at lower mach numbers. This would include, but not be limited to, Inflatable Aerodynamic Decelerators

(IAD) and supersonic retro-propulsion, both of which are scalable to much larger configurations.

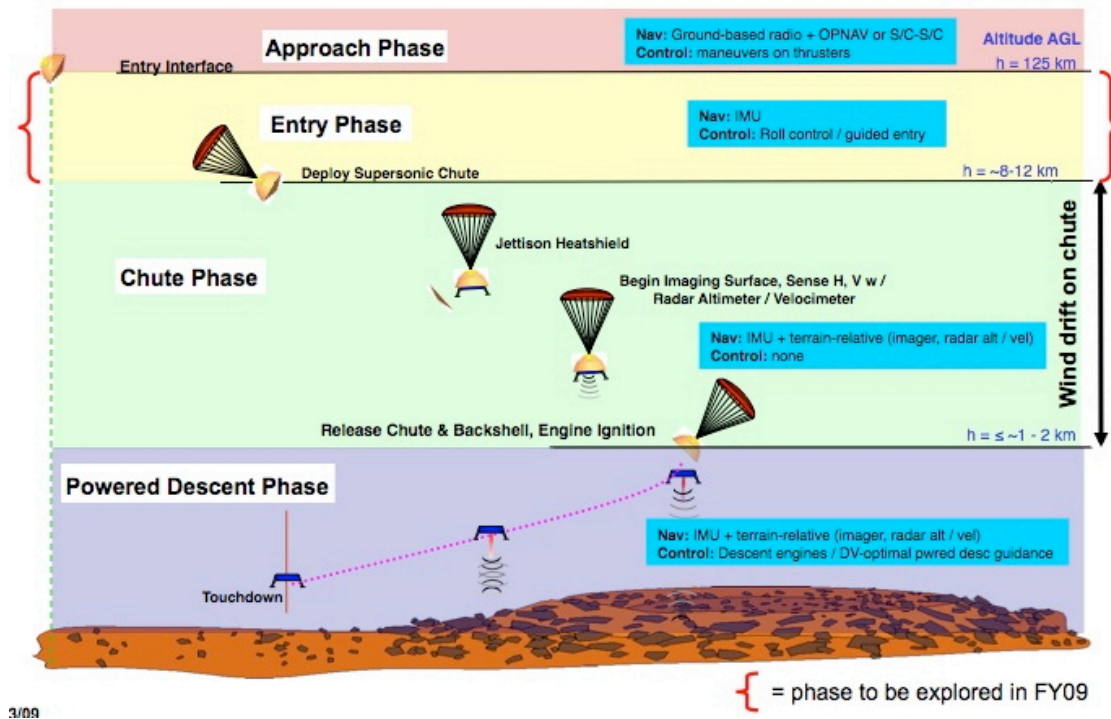


Figure A-4. Large-Robotic-Class Design Reference Mission.

It is of high interest for near term robotic missions to have the ability to deliver the payload to the surface with very high landing accuracy: within 100 m of the intended target. Pin-Point Landing (PPL) during powered descent is employed as the next logical state-of-the-art step to achieve this level accuracy, amongst other navigational enhancements (see Figure A-5). Note that PPL will be studied in FY10 and beyond in favor of a simple gravity turn in FY09 for ease of establishing an integrated analysis process across multiple centers.

The landed accuracy of the Large-Robotic-Class DRM is compared with that of MSL in Figure A-5. It is expected that an additional 400 kg of propellant will be required to “fly-out” typical delivery errors at ignition of the powered descent stage. This extra propellant combined with the 1.1 metric ton of landed mass achieves the desired 1.5 metric ton equivalent capability. Note for FY09, a landed mass of 1.5 metric ton will be delivered to the surface using a gravity turn only.

Note for FY09, a landed mass of 1.5 metric ton will be delivered to the surface using a gravity turn only. To further challenge the system, the DRM will assume a landing at a relative high altitude of 0 km MOLA during an arrival opportunity with unfavorably low atmospheric density. Unfavorable atmospheres are seasonally related and it has been determined that an Earth departure date in 2022 would provide sufficiently stressful Mars arrival atmospheric conditions. In addition, 2022 demands much higher Earth departure energy, or C3, that will also put a challenge on the assigned launch vehicle. Table 1 provides a summary of the general assumptions that will be utilized for the robotic DRM.

The similarities of this DRM to MSL include (1) a 4.7 m, 70 deg cone angle aeroshell, (2) the Apollo entry guidance, (3) the Sky Crane architecture, and (4) a Descent stage propulsion system. Some of the differences are (1) a pin-point landing strategy, (2) a three-axis stabilized cruise stage for improved attitude uncertainty (cruise balance mass removed), (3) a velocity trigger chute deploy strategy, (4) TPS thickness scaled up to account for increased heating, (5) propellant mass and tanks scaled for increased

propellant, (6) more engines added to the Skycrane configuration, and (7) remaining structure scaled as a function of acceleration loads and increased payload mass.

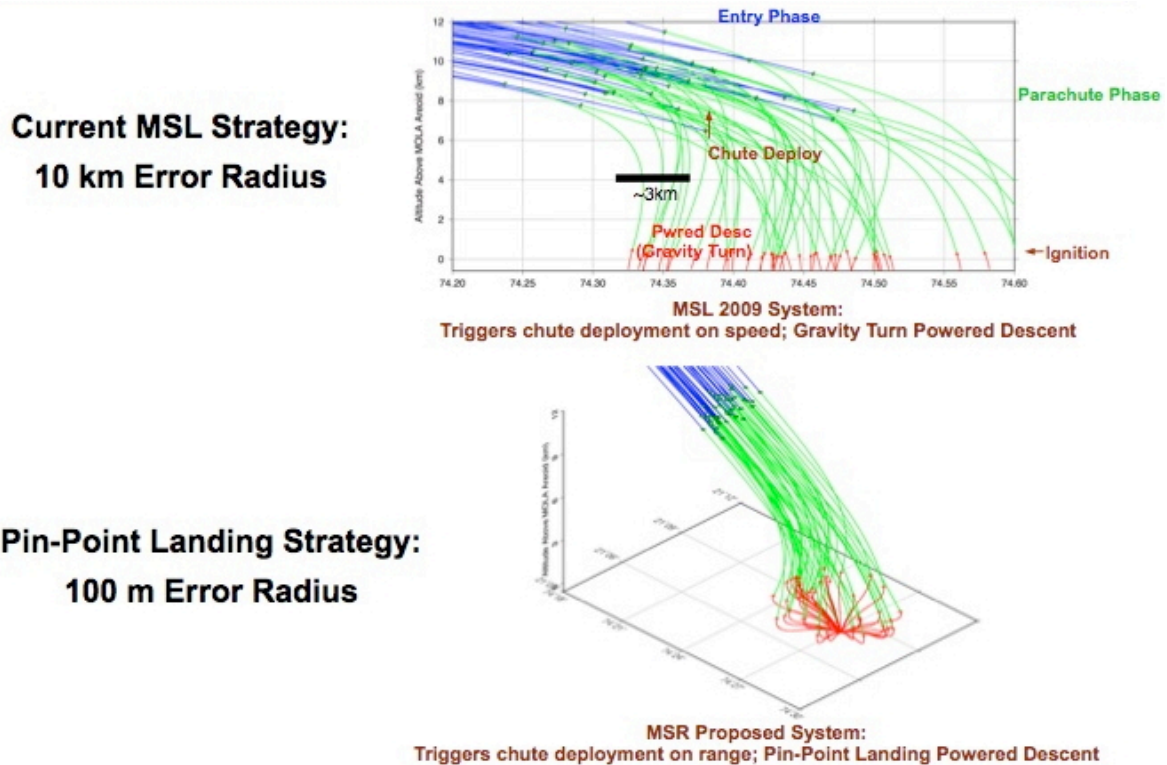


Figure A-5. MSL and Large-Robotic-Class Mission Landing Strategies

Table A-2. Key parameters of the large-robotic-class DRM.

Assumption	Value	Comments
Configuration	4.7 m aeroshell 12 MLE's 700 kg prop load	Scaled MSL design: 4.7 m, 70 deg cone aeroshell, more MLE's deduced to maintain T/W, more propellant needed to all a direct consequence of 1.5 t payload
Entry Mass	5400 - 5600 kg	Dependent on scaled configuration.
Entry Altitude	125 km	
Entry Speed	5.6 km/s	Dependant on arrival trajectory (direct descent assumed).
Entry Flight Path Angle	-15.5 deg	Defined to maximize altitude at heat shield jettison. Optimal is defined as optimal balance between system impacts (e.g. heat shield thickness) and altitude at heat shield jettison.
Entry Guidance	Apollo	MSL Apollo guidance. No pin-point landing; MSL gravity turn strategy
Opportunity	2022	Most challenging Earth departure C3 & Martian Atmosphere (Type I/II transfer assumed).
Site Latitude	0 deg	Near equatorial
Site Altitude	0 km MOLA	
Launch Vehicle	Delta IV - Heavy	Atlas V 551 most likely not capable.

## A.2 EDL-SA Study Ground Rules and Assumptions

This section lists the Ground Rules and Assumptions (GR&As) employed in the EDL-SA Study.

### A.2.1 General Ground Rules and Assumptions

- \* Margins will be applied to all technologies and systems as described in Section A.2.4.
- \* Subsystem performance parameters, e.g., engine Isp, engine T/W, vehicle inert mass fraction, will be based upon historical data and trends.
- \* The atmosphere model used for this study will be MarsGRAM 2005.
- \* Turbulent flow onset will be estimated using the  $Re_{\theta} = 200$  criterion.
- \* Representative guidance algorithms will be developed. Representative guidance algorithms will be used for final FOM evaluations.
- \* POST2 will be used for simulations.
- \* The nominal landing site altitude will be 0 km MOLA.
- \* The global landing precision will be within 50 m of the desired touchdown point.
- \* Landing site altitude sensitivities will be evaluated for -1 km. MOLA to 2.5 km. MOLA.
- \* Peak heating and total heat load will be determined using methods provided by the TPS designers.
- \* Hazard avoidance technology will be provided by the ALHAT project. Hazards could be pre-deployed assets or natural hazards.
- \* The thermal protection system is uncompromised at Mars arrival.

### A.2.2 Exploration Mission Ground Rules and Assumptions

- \* The shed drag device must never pass any closer than 2 km. to the target at any point in its trajectory (“keep-out zone” criterion).
- \* The Ares V shroud will be capable of launching a 10 m diameter by 33 m length Mars entry aeroshell
- \* Separation events will be modeled as a 10-sec. interval with no deceleration.
- \* Simulations will include a method (e.g., divert maneuver, fly away) to ensure the “keep out zone” criterion is met.
- \* Crewed and Cargo entries will be made from Mars orbit.
- \* Aerocapture will be used to insert the cargo vehicles in the desired parking orbit. One sol and 500 km. circular orbits will be used to provide sensitivities.
- \* Deceleration limits for crewed entry will use the relevant Entry limits from CxP 70024, “Human Systems Integration Requirements.”
- \* The nominal landed payload mass will be 40 mT.
- \* Payload mass sensitivities will be evaluated for 20–50 mT.
- \* First human landing will be no later than 2033.
- \* Only those technologies capable of being at or above TRL 6 by 2025 will be considered.
- \* First human landing will be no later than 2033. Technology Development Roadmaps will establish TRL 6 capability by 2025.

### A.2.3 Robotic Mission Ground Rules and Assumptions

- \* The nominal landed payload mass will be 1.5 mT.
- \* Mars opportunity will be 2022.
- \* Interplanetary mission design will be direct to entry (e.g. no aero/propulsion capture into a Mars parking orbit).
- \* Entry vehicle will be an MSL, 4.7 m entry vehicle with scaled elements as necessary for g-load, heat load, chute inflation loads, payload mass, etc.

- \* Entry phase will utilize Apollo guidance through a velocity trigger chute deploy.
- \* Descent & landing phase mission design will be an MSL descent stage with sky crane.
- \* Landing accuracy: Simple Gravity Turn: <=10 km from the target landing site.
- \* Landing accuracy: Pin-Point Landing: <= 100 m from the target landing site.
- \* Capability will be assessed to a 0 km MOLA altitude landing site at 0 deg latitude.
- \* Launch vehicle will be a Delta-IV heavy class or smaller.

#### **A.2.4 Margin Policy**

The design margins utilized in most previous Mars architecture/EDL studies have been quite optimistic. Indeed, some studies have carried no margin at all, and others have applied margins only to mass. The EDL-SA Study will use an integrated margin approach that is derived from current practice in the early phases of flight projects, e.g., development projects in the Constellation Program and robotic missions in the Mars Program. This margin approach will provide an appropriate level of realism to the study results.

Margin is composed of both consumable margin and design margin. Consumable margin is margin that exists in excess of the current estimate. Design margins provide design requirements that increase the robustness of the design; it is tied to subsystem requirements, generally performance parameters—structural integrity, thermal limits, TPS thickness, etc. This type of margin is not consumed during the course of the project.

In this study, the consumable margin is defined by

$$\text{Margin} = \text{Allocation} - \text{Current Best Estimate.}$$

This is sometimes given in percentage terms:

$$\% \text{Margin} = \frac{\text{Allocation} - \text{CBE}}{\text{Allocation}} \times 100\%$$

Allocation is the amount of a resource that has been allotted to a subsystem, and Current Best Estimate is the amount of a resource that is available or needed without any additional contingency. Targets for consumable margin are based on the life-cycle stage of the design and the maturity of the subsystem. This type of margin is released through the life of the project. Table A-3 defines the subsystem quantities to which margin is applied and the amount of margin that is utilized in the EDL-SA Study.

**Table A-3. EDL-SA Subsystem Margins**

<b>Parameter</b>	<b>Description</b>	<b>Value</b>
Dry Mass	Each configuration will have a minimum Dry Mass Margin. The minimum dry mass margin is applied across the complete operational scenario of each configuration. Note that technologies with a TRL <6 will have a Dry Mass Margin increment added - listed elsewhere.	30%
Propellant Mass	Propellant mass margin is used to account for the margin in Delta V and overall margin in propellant mass. The propellant mass margin value is derived assuming a 20% DV margin (equates to about a 15% propellant margin) plus a direct 20% propellant mass margin. All tankage will be sized based on the fully margined propellant mass, with the fully margined dry mass. Propellant mass margin does not include any ullage or unusable volume assumptions.	35%
Thrust	All integrated thrust modules will have a minimum thrust margin applied after initial sizing. Note that the thrust shall be sized based on the fully margined mass.	25%
Skipout	The entry flight path angle will maintain a minimum margin from skipout.	≥1 degree
Structural Integrity	Using appropriate structural factors of safety (defined elsewhere), each element will maintain a positive margin greater than the specified value.	≥ 0.2
TPS Thickness	All TPS (ablative or insulative) will have a minimum thickness margin applied. Note that the thickness margin is in addition to the Dry Mass margin.	30%
Inflation Mass	Where an inflatable decelerator is used, and an on-board gas supply or gas generator is used, then the mass available for inflation will have a minimum gas supply mass margin applied. If the system uses a continuous monitoring and fill system, then the margin is applied for the complete gas mass consumed. Does not apply to parachutes.	30%

For TPS the margin policy mirrors that used for Orion TPS development. See “Mars EDL/SA Thermal Protection System (TPS) Margin Management Plan” for the details.

Since this study assesses the potential benefits of technologies for landing large payloads on the surface of Mars, the lack of maturity of newer technologies needs to be reflected in the analysis. Hence, this study will report the simulation results both with and without a “TRL Increment”—the lower the TRL, the higher the increment—to guard against over-optimism in the forecasts of immature technologies. The TRL-based biasing of the margins is a penalty that is added to the baseline margin value given in Table A-4. In addition to this additional mass margin for low TRL technologies, Monte Carlo simulation variables (section 4.5) will be assessed and on a case-by-case basis, a wider variability (indicative of performance uncertainty) will be applied to some parameters. An example would be increased aerodynamic uncertainties for systems that do not have established aerodynamic databases. These penalties will be documented in the Peer Review charts and Final Report, and the results will manifest themselves in the proxy variables for the Figures of Merit.

**Table A-4. TRL Margin Increments**

TRL No.	Mass Margin Increment
9	0
8	0
7	0
6	0
5	20%
4	25%
3	30%
2	40%
1	50%

### A.2.5 Exploration Mission Monte Carlo Parameters

The simulations underlying the system analyses performed in this study utilize Monte Carlo procedures to account for various uncertainties in the system and its environment. The uncertainties include both aleatory (variability) and epistemic (lack of knowledge) ones. We adopt the customary approach of describing the uncertainties by probability density functions (PDFs). The PDFs represent the degree of belief about the distribution of the uncertain quantities—not only the nominal (most likely) values, but also their distribution between their plausible upper and lower limits. Of course, these subjective choices are informed by the statistical data that does exist and the team’s experience with Monte Carlo simulations of previous Mars missions (MER, Phoenix, MSL). Conservative adjustments were made because of lack of detailed information (experimental data, high-fidelity analyses) on current concepts.

Table A-5 and Table A-6 list the parameters that are treated probabilistically in the ellipsled and inflatable (MIAS) simulations, respectively. For each uncertain parameter, the rationale for the choice of distribution is included. The aerodynamic databases used in the simulations are based upon engineering-level tools. The uncertainties in these data are modeled by multipliers on the aerodynamic coefficients. The model for the uncertainty in the Mars atmosphere is the model contained in MARSGRAM; the range for the random number seed is provided in the tables. Atmospheric density perturbations are applied to all cases except the nominal, and winds are applied to all cases except nominal. For now, the de-orbit DV considers only maneuver execution errors. As the EDL-SA Study matures, more variables will be treated probabilistically in the simulations. For example, once more accurate entry states are obtained; perturbations to them will be included.

**Table A-5. Mid-L/D Rigid Monte Carlo Parameters**

Parameter	Nominal	Perturbation	Distribution	Rationale
Mass Variation (kg)	0	±10	Normal	Not currently used. Sensitivity to ballistic coefficient needs to be quantified as the study matures – i.e. those technologies with less sensitivity would be favored over those with a high sensitivity. (also this sensitivity will be nonlinear in many instances). To minimize the number of Monte Carlo scripts that must be certified, this capability has already been added – but will not be exercised until later in the study.

Lift Coefficient Multiplier	1	±10 %	Normal	Larger than would be expected to provide sensitivity analysis. The sensitivity characteristics of the technology are important considerations. Also the aerodynamics are uncorrelated, to further magnify the sensitivities. Many technologies will look good at their design point – one major discriminator will be sensitivity.
Drag Coefficient multiplier	1	±10 %	Normal	See Lift Coefficient Multiplier discussion.
Angle of Attack (deg)	55	±5	Normal	Angle of attack will vary the ballistic coefficient, and will amplify the ratio of Mass/CL to Mass/CD, to provide sensitivity analysis
Engine Isp (sec)	369	±2.5 %	Normal	This was an estimate for LOX/CH4 engines which have not been built. This parameter is expected to be a secondary sensitivity parameter for most of the technologies to be considered. If it becomes a primary driver, this will be reevaluated.
Deorbit ΔV (m/s)	14.978167	±0.279*	Normal	In lieu of having initial states generated for this study (time and resources that would not be a driver in selecting technologies), this parameter is used as an analog to provide the entry g's and heat pulse variation that would be expected from this type of mission.
Atm Random #	1	1-29999	Integer Uniform	In lieu of having initial states generated for this study (time and resources that would not be a driver in selecting technologies), this parameter is used as an analog to provide the entry g's and heat pulse variation that would be expected from this type of mission.
Dusttau	0.7	0.1:0.9	Uniform	This determines the dust loading and thus the density and wind profiles that the vehicle will experience. This range provides large variability, but would not include dust storms.
Notes				
* ΔV perturbation selected to produce a +/- 0.25 deg variation in entry Flight Path Angle				

Preliminary Lift and Drag Coefficient multipliers act on aerodynamic tables provided by Dr. Alan Wilhite for the ellipsled shape. The tables were generated using a program called APAS. For the high supersonic to hypersonic region, a modified Newtonian technique is used to calculate the pressure distribution on surfaces as a function of the incident angle to the flow. The pressures are integrated to get the aerodynamic coefficients. However, it cannot accurately predict trim angles (generally errors are on

order of 4 to 5 deg), but the approximations are sufficient for analysis of the current fidelity. Note that this method will not work once packaging requirements are imposed. Aerodynamic data provided in the MIAS reports is used for the inflatable configuration.

**Table A-6. Low-L/D Inflatable Monte Carlo Parameters**

Parameter	Nominal	Perturbation	Distribution	Rationale
Mass Variation (kg)	0	+/- 10	Normal	Not currently used – Sensitivity to ballistic coefficient needs to be quantified as the study matures – i.e. those technologies with less sensitivity would be favored over those with a high sensitivity. (also this sensitivity will be nonlinear in many instances). To minimize the number of Monte Carlo scripts that must be certified, this capability has already been added – but will not be exercised until later in the study.
Lift Coefficient Multiplier	-1**	+/- 10 %	Normal	Larger than would be expected to provide sensitivity analysis. The sensitivity characteristics of the technology are important considerations. Also the aerodynamics are uncorrelated, to further magnify the sensitivities. Many technologies will look good at their design point – one major discriminator will be sensitivity.
Drag Coefficient multiplier	1	+/- 10 %	Normal	See Lift Coefficient Multiplier discussion.
Angle of Attack (deg)	27.5	+/- 2	Normal	Angle of attack will vary the ballistic coefficient, and will amplify the ratio of Mass/CL to Mass/CD, to provide sensitivity analysis.
Engine Isp (sec)	369	+/- 2.5 %	Normal	This was an estimate for LOX/CH4 engines which have not been built. This parameter is expected to be a secondary sensitivity parameter for most of the technologies to be considered. If it becomes a primary driver, this will be reevaluated.
Deorbit ΔV (m/s)	14.0	+/- 0.279*	Normal	In lieu of having initial states generated for this study (time and resources that would not be a driver in selecting technologies), this parameter is used as an analog to provide the entry g's and heat pulse variation that would be expected from this type of mission.
Atm Random #	1	1-29999	Integer Uniform	This is used by the atmosphere program to determine the variability in the density and wind profiles. The range is that allowed by the

				Mars atmosphere program used in the simulation. Also, other atmospheric parameters have been set, based on MSL experience, that would further stress the system.
Dusttau	0.7	0.1:0.9	Uniform	This determines the dust loading and thus the density and wind profiles that the vehicle will experience. This range provides large variability, but would not include dust storms.
Notes				
* DV perturbation selected to produce a +/- 0.25 deg variation in entry Flight Path Angle				
** Sign of lift changed so that 0 deg bank angle is lift up – MSL convention as compared to AFE convention				

Lift and Drag Coefficient multipliers act on MIAS aerodynamic tables (MIAS Final Presentation, March 2002).

MarsGRAM density and wind perturbations are applied to all cases except the nominal

Monte Carlo analysis is not planned for the all-propulsive configuration at this time.

#### A.2.6 Robotic Mission Monte Carlo Parameters

As with the Exploration mission, the simulations underlying the system analyses performed in the robotic study utilize Monte Carlo procedures to account for various uncertainties in the system and its environment. Table A-7 lists the parameters that are treated probabilistically in the robotic simulations. For each uncertain parameter, the rationale for the choice of distribution is included. The model for the uncertainty in the Martian atmospheric density is the dust tau model contained in MARSGRAM. Atmospheric density perturbations are applied to all cases except the nominal, and winds are applied to all cases except nominal.

**Table A-7. Robotic Monte Carlo Parameters**

Parameter	Nominal	Perturbation	Distribution	Rationale
Entry State Delivery and Knowledge Error	Position, Velocity as necessary to impact desired landing site.	Per Entry States File	Normal	Entry states file generated assuming a MSL dsn only attitude control system. Nominal entry state determined to be consistent with the Earth/Mars transfer trajectory and desired landing location for the date and time assumed.
Attitude Knowledge Error	Angle of Attack = 30deg. Bank = 70 deg.	0.25 deg about a varying rotation axis.	Direction of rotation axis computed uniformly in all directions (i.e. spherical distribution).	Again, a dsn only attitude control system is assumed.
Lift/Drag	0.3	+/- 0.04	Normal	Accounts for uncertainty in trim angle due to c.g. location uncertainty directly from detailed MSL analysis.
Angle of Attack (deg)	-19.5	+/- 2	Normal	The nominal angle of attack will vary to achieve the desired nominal lift/drag ratio. Perturbation value is

				typical variation from the ideal due to stability oscillations about the nominal trim angle.
Winds (m/s)	0 (horizontal); 0 (vertical)	Horizontal: 25 m/s Vertical: 20 m/s	Horizontal: constant magnitude with direction uniform from 0 to 360 deg. Vertical: normal distribution in direction and magnitude.	Represents constructed engineering winds that encompass most wind conditions on Mars as compared to global circulation models contained in MarsGRAM.
Dusttau	0.33	0.1:0.75	Uniform	This determines the dust loading and thus the density and wind profiles that the vehicle will experience. This range provides large variability, but would not include dust storms.

### A.3 EDL-SA Study Figures of Merit

The technology recommendations from the EDL-SA Study will be based on Figures of Merit (FOMs) that assess the impact of the technologies upon key performance, cost and risk metrics for the missions.

#### A.3.1 Description of Figures of Merit

In general, desired attributes of FOMs are that they be

- \* as mutually independent as possible (or allow modeling of dependencies),
- \* as non-redundant as possible (no double bookkeeping),
- \* as complete as possible (include all potentially discriminating attributes between alternatives),
- \* as few as possible (not include non-discriminating attributes),
- \* as quantifiable as possible (or have proxy variables that are quantifiable),
- \* as well-defined as possible (allow common understanding for evaluation),
- \* grouped in a hierarchy (enable ease of evaluation/scoring roll-up). Need to define categories.
- \*

The following two subsections define the categories and definitions of the figures of merit. In many cases, direct assessment of the particular FOMs is not possible due to the lack of a detailed system definition in early-phase design or because there is no definitive measure for the FOM. In these cases proxy variables are evaluated instead. The proxy variables are ones that are believed to have a strong correlation with the desired FOM.

#### A.3.2 Categories for Figures of Merit

The categories chosen for the FOMS are the following:

**Performance and Effectiveness** - Provide Figures of Merit associated with performance and effectiveness, determining the degree to which a technology option effectively meets mission needs and improves mission performance

**Affordability and Life-Cycle Cost** – Provide Figures of Merit associated with system life-cycle costs, determining the degree to which a mission concept or technology option reduces technology and

system development and recurring costs

**Programmatic Risk** – Provide Figures of Merit associated with technology and programmatic risk, determining the degree to which a technology option affects these risks.

**Applicability to Other Missions**– Provide Figures of Merit associated with extensibility, determining the degree to which a mission concept or technology option could be used for other missions or customers.

**Safety and Mission Success** - Provide Figures of Merit associated with safety and mission success, determining the degree to which a technology option ensures safety and reliability for all mission phases

### A.3.3 Definitions of Figures of Merit

Table A-8 provides the definitions for the FOMs Exploration-class missions. The proxy variables for the FOMs used in the EDL-SA Study for Exploration-class missions are provided in Appendix B.

FOMs for large-robotic-class missions are expected to differ from these to a minor extent.

**Table A-8. Definitions of Figures of Merit**

Category	Figure of Merit	Definition
Safety and Mission Success	Likelihood of Loss of Mission	Likelihood of a critical failure occurring during the MOI and EDL phases resulting in loss of one or more mission objectives
	Likelihood of Loss of Crew	Likelihood of a critical failure occurring during the MOI and EDL phases resulting in loss of one or more crew members
Performance and Effectiveness	Sensitivity to Usable Payload Mass to Surface	Ability of the technology approach to successfully land usable hardware, cargo, fluids, and crew beyond that required for the mission.
	Sensitivity to Surface Elevation	Ability of the technology approach to provide the capability to land at sites above the required surface elevation.
	Sensitivity to Landing Precision	Ability of the technology to land closer to the desired landing site than required for the mission
	Sensitivity to Environmental Variability	Range of atmospheric density, dust and wind profiles that can be tolerated.
Programmatic Risk	Technology Development Risk	Likelihood of Mars EDL architecture technology development activities to exceed schedule and budgetary constraints.
	Programmatic Cost and Schedule Risk	Likelihood of DDT&E activities for Mars EDL system to exceed planned development schedule or planned development budget for a given technology approach.
Affordability and Life-Cycle Cost	Technology Development Cost	Cost to develop required technologies to TRL 6.
	Advanced Development Cost	Cost to develop required technologies from TRL 6 to TRL 8.
	System Life-Cycle Cost	EDL-related system life-cycle cost (e.g., DDT&E, production, processing, launch, mission operations).
Applicability to Other Missions	Applicability to Mars Robotic Missions	Applicability of technologies, systems, and operations to Mars robotic missions.
	Applicability to Other Planetary Missions	Applicability of technologies, systems, and operations to other planetary entry missions.

### A.3.4 Scoring for Figures of Merit

There are many alternatives for scoring and rolling-up (weighting) the figures of merit. Particular choices for these have not yet been made. Study results will include sensitivities to weighting choices.

A.3.5 FOM Proxy Parameters

Table A-9. Safety and Mission Success Proxy Parameters

Category	Figure of Merit	Definition	Proxy Parameters
Safety and Mission Success	Likelihood of Loss of Mission	Likelihood of a critical failure occurring during the MOI and EDL phases resulting in loss of one or more mission objectives	System/subsystem functional redundancy (e.g. engine-out capability).
			Number and complexity of major EDL architecture elements/systems.
			Number and complexity of interfaces between major EDL architecture elements/systems.
			Number and complexity of in-space assembly operations.
			Number of Mars configuration transitions required.
			Number and type of system risks and mission hazards.
			Number and type of abort/safe haven options per mission phase.
	Likelihood of Loss of Crew	Likelihood of a critical failure occurring during the MOI and EDL phases resulting in loss of one or more crew members	System/subsystem functional redundancy (e.g. engine-out capability).
			Number and complexity of major EDL architecture elements/systems.
			Number of interfaces between major EDL architecture elements/systems.
			Number and complexity of in-space assembly operations.
			Number of Mars configuration transitions required.
			Number and type of system risks and mission hazards.
			Number and type of system risks and mission hazards.

**Table A-10. Performance and Effectiveness Proxy Parameters**

Category	Figure of Merit	Definition	Proxy Parameters
Performance and Effectiveness	Sensitivity to Usable Payload Mass to Surface	Ability of the technology approach to successfully land usable hardware, cargo, fluids, and crew beyond that required for the mission.	Sensitivity of Mars arrival system mass to increases in usable surface payload mass.
	Sensitivity to Surface Elevation	Ability of the technology approach to provide the capability to land at sites above the required surface elevation.	Sensitivity of Mars arrival system mass to increases in the landing site surface elevation.
	Sensitivity to Landing Precision	Ability of the technology to land closer to the desired landing site than required for the mission.	Sensitivity of Mars arrival system mass to decreases in the distance between the final landing site and the specified landing site.
	Sensitivity to Environmental Variability	Range of atmospheric density, dust and wind profiles that can be tolerated.	Based on Monte-Carlo analyses, the 3-sigma ranges of density, dust and wind profiles that can be tolerated and meet the specified landing requirements.

**Table A-11. Programmatic Risk Proxy Parameters**

Category	Figure of Merit	Definition	Proxy Parameters
Programmatic Risk	Technology Development Risk	Likelihood of Mars EDL architecture technology development activities to exceed schedule and budgetary constraints.	Number of technologies required.
			TRLs of technologies.
			RD3 scores of technologies (e.g., number and type of large-scale integrated ground demonstrations required, number and type of required flight tests, including scale of Earth and Mars atmosphere tests).
	Programmatic Cost and Schedule Risk	Likelihood of DDT&E activities for Mars EDL system to exceed planned development schedule or planned development budget for a given technology approach.	Level of EDL system design maturity/uncertainty for given technology approach
			Number and level of complexity of Mars EDL architecture systems
			Number of interfaces between major Mars EDL architecture elements/systems
		Number of configuration transitions required	

**Table A-12. Affordability and Life Cycle Cost Proxy Parameters**

Category	Figure of Merit	Definition	Proxy Parameters
Affordability and Life Cycle Cost	Technology Development Cost	Cost to develop required technologies to TRL 6.	Number of technologies required.
			TRLs of technologies.
			RD3 scores of technologies (e.g., number and type of large-scale integrated ground demonstrations required, number and type of required flight tests, including scale of Earth and Mars atmosphere tests).
	Advanced Development Cost	Cost to mature required technologies from TRL 6 to TRL 8.	Total gross mass of Mars arrival systems.
			Number of technologies required.
			TRLs of technologies.
			RD3 scores of technologies (e.g., number and type of large-scale integrated ground demonstrations required, number and type of required flight tests, including scale of Earth and Mars atmosphere tests).
	System Life-Cycle Cost	EDL-related system life-cycle cost (e.g., DDT&E, production, processing, launch, mission operations).	Total gross mass of Mars arrival systems.
			Total (length + diameter) of Mars arrival systems (stowed).
			Total dry mass of Mars arrival systems.
			Number and level of complexity of Mars EDL architecture systems.
			Number of interfaces between major Mars EDL architecture elements/systems.

**Table A-13. Applicability to Other Mission Proxy Parameters**

Category	Figure of Merit	Definition	Proxy Parameters
Applicability to Other Missions	Applicability to Mars Robotic Missions	Applicability of technologies, systems, and operations to Mars robotic missions.	Level of hardware commonality and traceability between Mars Exploration-class mission and Mars Large-Robotic-class mission EDL technologies, systems, operations, infrastructure, and approaches.
	Applicability to Other Planetary Missions	Applicability of technologies, systems, and operations to other planetary entry missions.	Level of hardware commonality and traceability between Mars EDL and other planetary mission technologies, systems, operations, infrastructure, and approaches.

## **B Appendix B: EDL Transition Events**

### **B.1 Background**

During the FOM assessment both integrated architectures and individual technologies were considered. For the architectures assessment, the events that involved transitioning from one decelerator technology to another were identified as drivers for technical and programmatic risk as well as performance. Because of the perceived importance of these events to the architecture FOM assessment and the relative immaturity of the design concepts, a series of working meetings were organized with NASA EDL experts to develop design concepts and an understanding of the risk/performance trade-offs for key transition scenarios in the reference exploration class EDL architectures. The following is a summary of the results of the working meetings that were integrated into the FOM assessment.

### **B.2 Methodology**

To collect the information needed to assess the relative benefits and challenges associated with each transition event, a list of key experts in the fields relevant to EDL were asked to participate in two meetings. The first meeting was focused on the design of the EDL transitions and the technical mission risks, and the second meeting was focused on the human roles and human safety considerations for each transition concept developed during the first meeting.

The first meeting was held at JPL and technical experts were invited that had flight mission experience from various past Mars missions as well as MSL. The objectives of the JPL meeting are listed below:

The EDL system transitions are defined, including the approaches to, and the subsystems for, accomplishing those transitions

The EDL sequences of (non-transition) events are defined, including the approaches to, and the subsystems for, accomplishing those events

The major ground and flight tests required for EDL system technology development and advanced development are defined at the top level

The second meeting was held at JSC and technical experts were invited that had worked on Shuttle, ISS, and Orion. The objectives of the JSC meeting are listed below:

The EDL system transitions developed at JPL are critiqued and refined from the perspective of crewed missions

Critical EDL sequences of (non-transition) events for crewed missions are identified, along with the key constraints from the crew perspective

The major ground and flight tests required for EDL system technology development and advanced development, particularly for abort modes, are defined at the top level

### **B.3 Summary of Results**

The transitions in the reference were categorized by major transition and a total of 4 transition types were discussed:

Rigid Aeroshell to SRP

Rigid Aeroshell to Drag SIAD

Inflatable Aeroshell to SRP

Inflatable Aeroshell to Lifting SIAD

For each transition type, a family of transition options was developed. The following figures give an overview of the different strategies developed for each type of transition and the color codes indicate the preference based on risk and performance. Green indicates the baseline option and orange indicates the second choice.

### B.3.1 Rigid Aeroshell to SRP

Figure B-1 summarizes the family of options for the rigid aeroshell to SRP transition.

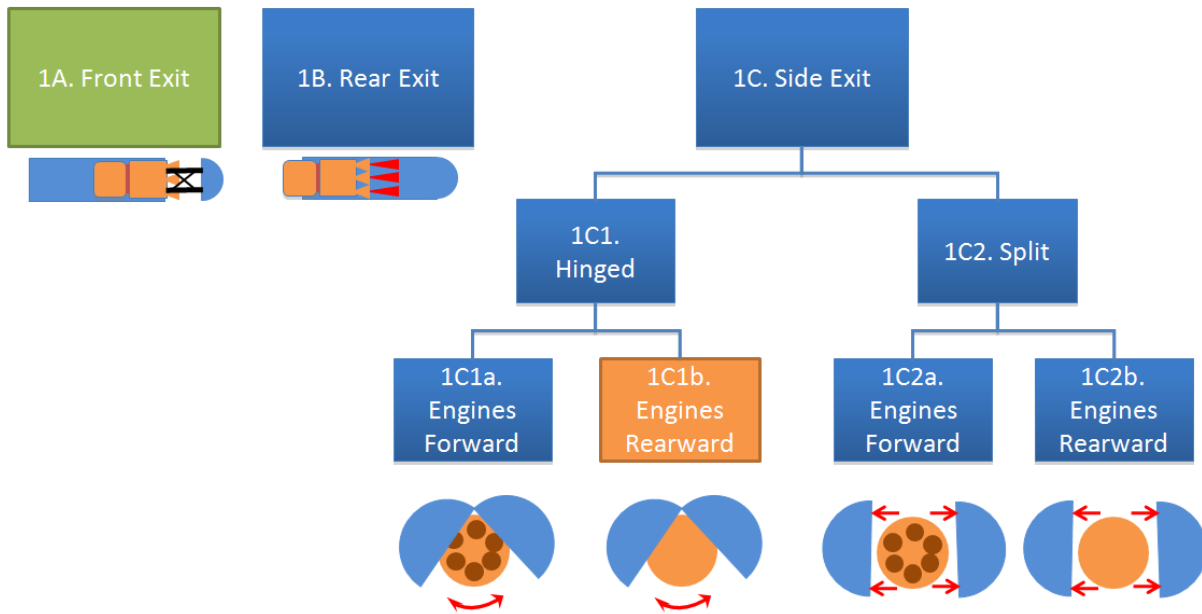


Figure B-1. Rigid Aeroshell to SRP Transition Options

All of these have the nose “into the wind” at transition except for option 1C2b which has a variant in which the aeroshell first rotates to put the tail “into the wind”. The major transition strategies include:

**1A. Front Exit:** The rigid aeroshell would pitch nose first into the velocity field and then the nose would be ejected allowing the descent stage to exit out of the front of the aeroshell. Additional drag augmentation such as retrorockets and small parachutes could be used to help insure a clean separation between the descent stage and the aeroshell. Another concept discussed included having the RCS maneuver the disposed aeroshell after separation to insure that the aeroshell did not re-contact the descent vehicle or any sensitive ground assets.

**1B. Rear Exit:** The rigid aeroshell would pitch nose first into the velocity field and then the descent stage would then slide out of the rear of the aeroshell with engines firing. The firing of the descent engines would help ensure the separation of the two bodies and in addition the RCS on the aeroshell may be used to help ensure proper disposal of the aeroshell after separation.

**1C. Side Exit:** This family of options includes several configurations of the descent stage within the aeroshell and for each option the descent stage would exit through the side of split pieces of the aeroshell. Charges would separate split the aeroshell into at least two pieces and those pieces would either be hinged or completely separate. Drag devices or retrorockets could be used to aid in the

separation.

The preferred option defined for this transition event is described in more detail in Figure B-2.

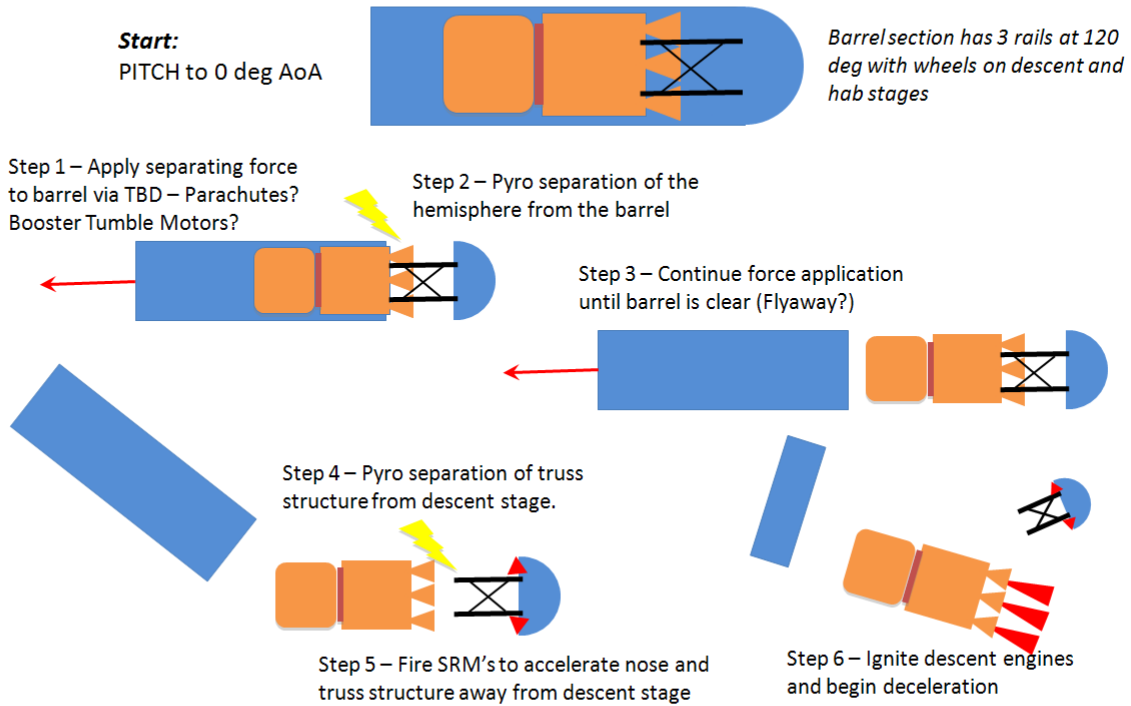


**Figure B-2. Baseline Rigid Aeroshell to SRP Transition Option**

### B.3.2 Inflatable Aeroshell to SRP

Figure B-3 summarizes the options developed for the inflatable aeroshell to SRP transition.

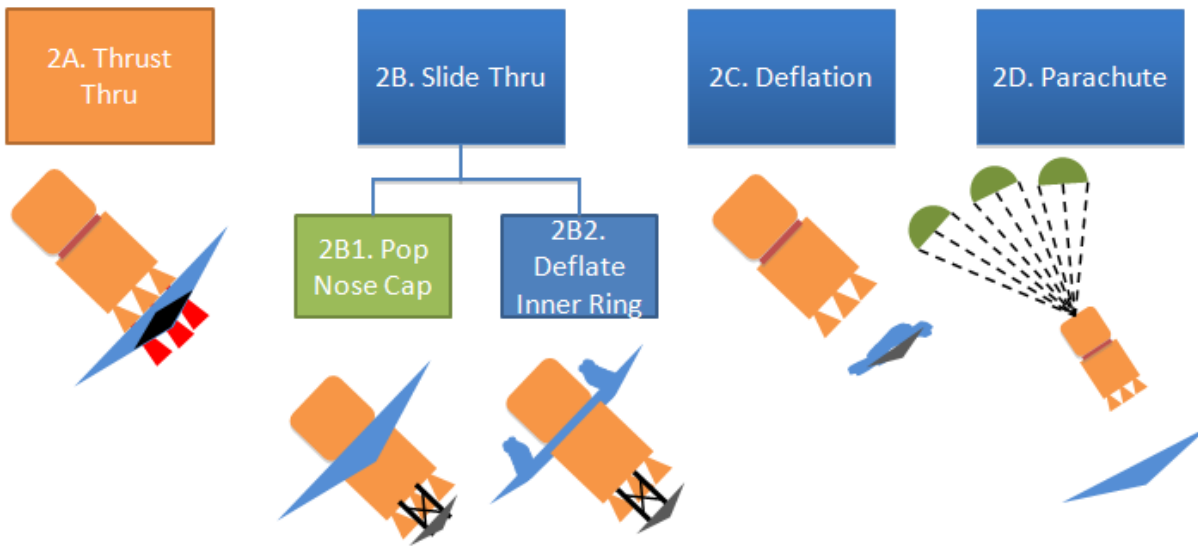


**Figure B-3. Inflatable Aeroshell to SRP Transition Options**

The major transition strategies for this transition include (see Figure B-3):

**2A. Thrust Thru:** This option would include holding on to the flexible aeroshell until touch down or very near to touch down. The aeroshell may have to be dropped to avoid interactions between the descent engines and the ground.

**2B. Slide Thru:** These options include the descent stage sliding through the center of the inflatable aeroshell and then dropping off the nose cap in front of the vehicle before the descent stage engines are started.

**2C. Deflation:** This option would include deflating the aeroshell and repackaging it such that the ballistic coefficient is high enough so the released material would fall in front of the descent stage.

**2D. Parachute:** This option would include using a larger deployable decelerator in the rear of the descent stage to give enough separation force to ensure a clean separation. However, the size of the parachutes would need to be very large in order to reduce the ballistic coefficient of the descent stage enough to ensure a clean separation.

The preferred option is described in more detail in Figure B-4.

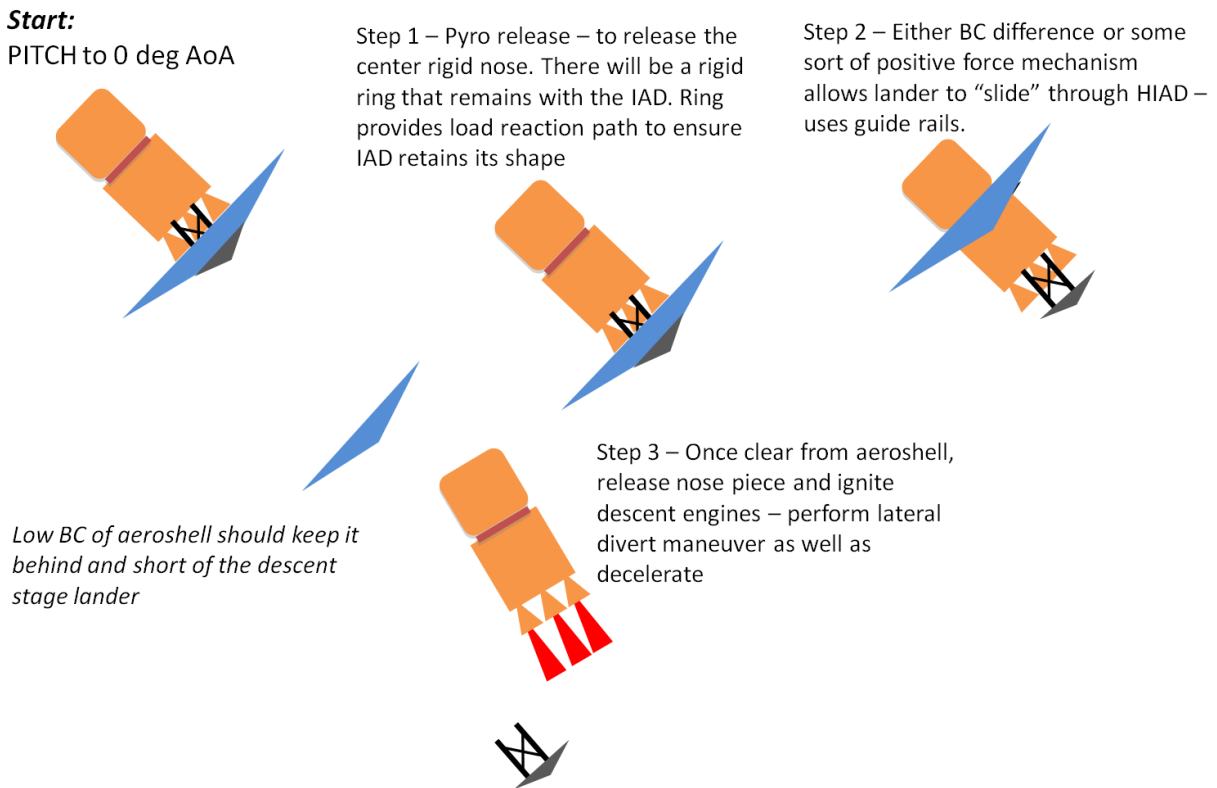


**Figure B-4. Baseline Inflatable Decelerator to SRP Option**

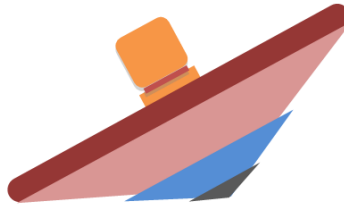
**Hypersonic Inflatable Aeroshell to Supersonic Inflatable Decelerator** - Figure B-5 summarizes the family of options for the hypersonic inflatable aeroshell to larger inflatable lifting supersonic decelerator transition.

**Start:**

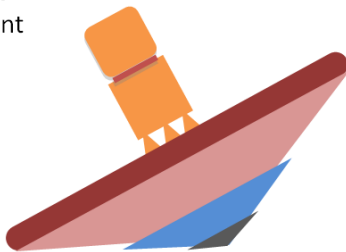
Initiate extension deployment at about Mach 2-5



Step 1 – At Mach 2-5 – inflate ring of outer torus to extend IAD



Step 4 – At Mach 0.7 – separate lander & descent stage from IAD and ignite descent engines



Step 5 – Continue to thrust while performing lateral divert maneuver as well as decelerate

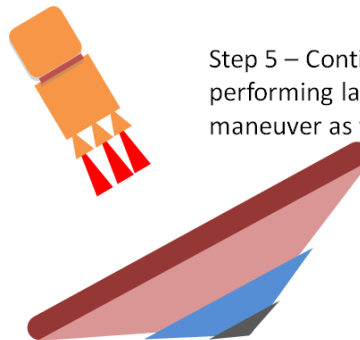


**Figure B-5. Inflatable Hypersonic Aeroshell to Supersonic Inflatable Transition Options**

The transition strategies include the following:

**5A. Staged Rings:** This includes a staged IAD deployment starting at Mach number of 6-10 with the final rings deployed at Mach 2-3.

**5B. Single Ring /Flexible Cone:** This includes a single IAD deployment event. The inflatable outer torus would be attached to the Hypersonic IAD by a flexible fabric that would provide the aerodynamic surface used for deceleration.

The preferred option is described in more detail in Figure B-6.

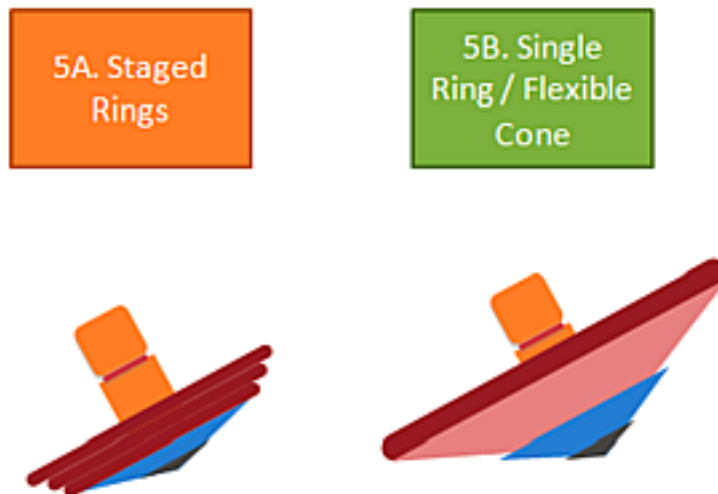


**Figure B-6. Baseline Hypersonic Inflatable Decelerator to Supersonic Inflatable Decelerator Option**

**Rigid Aeroshell to Supersonic Inflatable Decelerator** - Figure B-7 summarizes the options developed for the rigid aeroshell to inflatable decelerator transition.

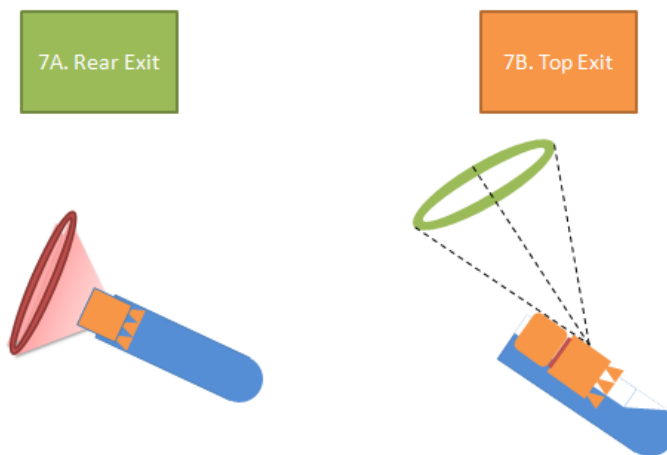


**Figure B-7. Rigid Aeroshell to Inflatable Aerodynamic Decelerator Options**

The transition strategies include the following:

**7A. Rear Exit:** This would include inflation of the aerodynamic decelerator out the back of the aeroshell and using the drag force to pull the descent stage away from the aeroshell. Rockets and the Aeroshell RCS may also insure a clean separation.

**7B. Top Exit:** This would include ejecting the back of the aeroshell (or in the case of an entry without a backshell TPS no ejection would be required) and then inflating the aerodynamic decelerator. The drag force would then pull the descent stage up out of the top of the aeroshell as shown in the figure.

The preferred option is described in more detail in Figure B-8.

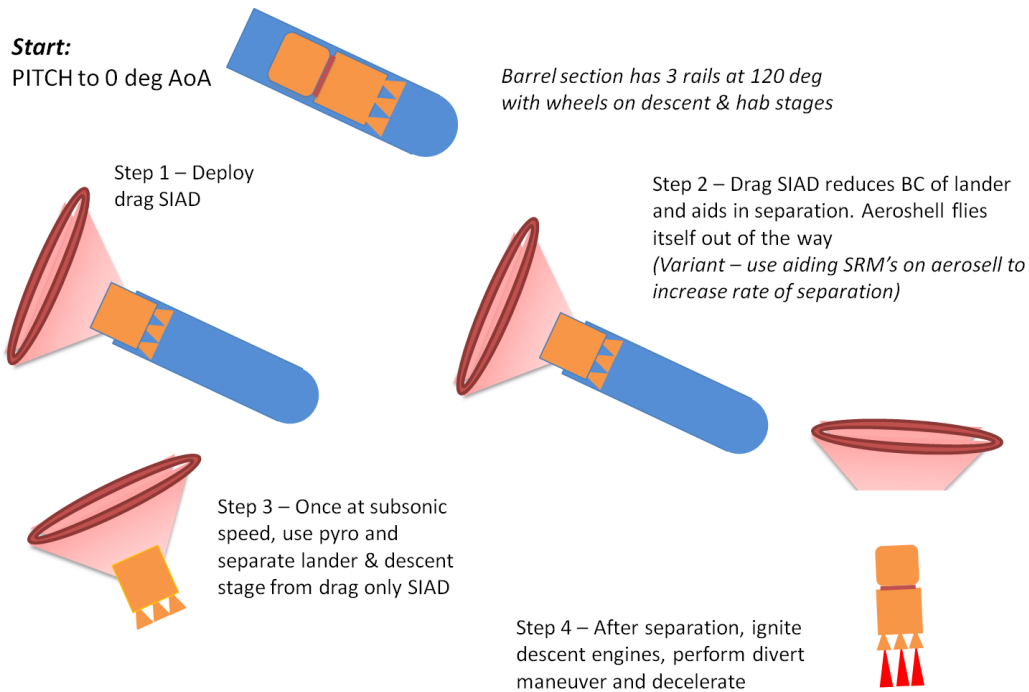


**Figure B-8. Baseline Rigid Aeroshell to Inflatable Aerodynamic Decelerator**

**Initial Failure Modes Assessment** - During the Transitions meeting an initial set of generic EDL failure modes was developed. The following table describes the failure modes, description and notional mitigation strategy

**Table B-1. EDL Failure Modes**

ID	Phase Fault Occurs	Phase Failure Occurs	Failure Mode Title	Failure Mode Description	Notional Mitigation Strategy
FM.1	Aerocapture/Entry	Aerocapture/Entry	Local heating augmentation due to surface features/roughness	Bondline over-temperature condition exceeded due to heating augmentation caused by a surface protuberance/cavity	Design Margins
FM.2	Aerocapture/Entry	Aerocapture/Entry	Hypersonic flow impingement on descent stage	Uncertainty in predicting afterbody flow behind a "convertible" rigid entry vehicle or the HIAD configuration result in exceeding allowable temperatures of payload and/or descent stage systems	Design Margins
FM.3	Descent	Descent	Propulsion flow impingement on descent stage	Uncertainty in predicting propulsion exhaust flow impingement on descent stage results in exceeding allowable temperatures of payload and/or descent stage systems	Design margins
FM.4	Cruise	Aerocapture/Entry	Loss of aeroshell/TPS structural integrity due to combined loads	Thermal-Structural loading and/or load cycling during mission results in cracking/ripping of structural hardware	Design margins
FM.5	Cruise	Aerocapture/Entry	Natural (in-space) environment degrades	In-space ionizing radiation, solar flare events, long duration vacuum exposure,	Abort, flight Test

			inflatable structure strength properties	etc. degrades the strength properties of deployable structures	
FM.6	Cruise	Aerocapture/Entry		In-space ionizing radiation, solar flare events, long duration vacuum exposure, etc. degrades the strength properties of deployable structures	Abort, flight Test
FM.7	Aerocapture/Entry	Aerocapture/Entry	Local heating augmentation due to control surfaces/thrusters	Bondline over-temperature condition exceeded due to heating augmentation caused by control surface or thruster	Design Margins
FM.8	Aerocapture/Entry	Aerocapture/Entry	Unexpected aerothermal environment	Uncertainty in predicting the aerothermal environment during entry results in bondline over-temperature condition	Design Margins
FM.9	Aerocapture/Entry	Aerocapture/Entry	Unexpected thermal response to aerothermal environment	Uncertainty in predicting the TPS material response during entry results in bondline over-temperature condition	Design Margins
FM.10	Unknown	Aerocapture/Entry	Deployable TPS/carrier structure damaged during assembly/storage/deployment	Deployable TPS/support structure physically damaged due to natural environment, packing loads, storage loads, launch loads or deployment event	Inspection/R repair
FM.11	Cruise	Aerocapture/Entry	In-space hypervelocity impact damage to payload, and/or support systems	MMOD damage punctures storage tanks, deflates inflatable structures, damages TPS, etc.	Inspection/R repair/Abort
FM.12	Aerocapture/Entry	Landing	Unexpected aerodynamic coefficients of entry vehicle	Uncertainty in prediction of aerodynamic performance of entry vehicle results in unexpected trajectory	Design Margins
FM.13	Reconfiguration	Descent	Re-contact with jettisoned elements	Hardware jettisoned during re-configuration events impacts and damages payload or support systems	Flight Test
FM.14	Descent	Landing	Descent engine does not start	Main descent engines fail to start up as expected due to mechanical system failure	Redundancy
FM.15	Descent	Landing	Payload unstable after touchdown due to engine transient shut down	Engine does not shut down as expected after descent stage contact with surface resulting in payload instability	Crew Controls
FM.16	Descent	Landing	Descent stage instability during descent	Forward jettisoned hardware disrupts free stream flow seen by the descent stage resulting in unexpected aerodynamic moments acting on the descent stage	Design Margins
FM.17	Descent	Landing	Unexpected propulsion performance	Uncertainty in main engine performance results in unexpected trajectory (e.g. caused by forward jettisoned hardware or unexpected supersonic shock interaction)	Design Margins
FM.18	Descent	Landing	Unexpected aerodynamic coefficients of drag device	Uncertainty in aerodynamic performance of deployed drag devices results in unexpected trajectory	Design Margins
FM.19	Descent	Landing	Aerodynamic drag devices not deployed	Aerodynamic drag devices not properly inflated or deployed	Redundancy
FM.20	Descent	Landing	Descent stage instability close to surface features	Main propulsion plume interaction with distributed surface features creates non-symmetric pressure distribution on descent stage which results in loss of vehicle stability	Crew Controls
FM.21	Reconfiguration	Descent	Loss of vehicle structural integrity due to pyro shock	Vibro-acoustic shock from pyro devices used during reconfiguration events result in structural damage to the payload or support systems	Design Margins

FM.22	Cruise/Aerocapture/Entry	Aerocapture/Entry	TPS gap/seam thermal or mechanical failure	Thermal or mechanical failure in or around a gap/seam in TPS (e.g. crack in seam due to combined loads, bondline under seam exceeds temperature limit)	Design Margins
FM.23	Landing	Landing	Unstable landed configuration due to unexpected surface features	Descent stage touch down on unstable or non-flat surface feature resulting in loss of vehicle stability on the surface	Crew Controls
FM.24	Landing	Landing	Unstable landed configuration due to trenching caused by main engines	Descent stage touch down on unstable or non-flat surface features caused by main engine trenching resulting in loss of vehicle stability on the surface	Surface Prep
FM.25	Descent	Landing	Debris damage during terminal descent	Debris kicked up by main engines damages the payload, support systems or other landed assets	Design Margins
FM.26	Aerocapture/Entry/Descent	Aerocapture/Entry/Landing	Gas bladder overpressure	Entry heating or inflation management system failure result in ripping/tearing of inflatable structures	Design Margins
FM.27	Descent	Descent	Loss of descent stage structural integrity due to propulsion induced vibro-acoustic loads	Uncertainty in the vibration and acoustic environment during powered descent result in structural damage to the payload or support systems	Design Margins
FM.28	Descent	Descent	Snap loads from Aerodynamic decelerator deployment damage descent stage and/or decelerator itself	Unexpected impulse forces during aerodynamic decelerator deployment results in damage to payload or support systems	Design Margins
FM.29	Descent	Descent	Loss of control surface/thruster functionality	Loss of commanded control capability during aerocapture, entry or descent results in unexpected trajectory	Redundancy
FM.30	Descent	Landing	Dynamic instability of descent stage caused by aerodynamic decelerator deployment	Non-symmetric deployment of aerodynamic decelerator results in dynamic instability of the descent stage	Design Margins
FM.31	Descent	Landing	Loss of flight computer functionality during AEDL	Flight computer fails to function during descent	Redundancy

**REPORT DOCUMENTATION PAGE**

*Form Approved  
OMB No. 0704-0188*

The public reporting burden for this collection of information is estimated to average 1 hour per response, including the time for reviewing instructions, searching existing data sources, gathering and maintaining the data needed, and completing and reviewing the collection of information. Send comments regarding this burden estimate or any other aspect of this collection of information, including suggestions for reducing this burden, to Department of Defense, Washington Headquarters Services, Directorate for Information Operations and Reports (0704-0188), 1215 Jefferson Davis Highway, Suite 1204, Arlington, VA 22202-4302. Respondents should be aware that notwithstanding any other provision of law, no person shall be subject to any penalty for failing to comply with a collection of information if it does not display a currently valid OMB control number.  
**PLEASE DO NOT RETURN YOUR FORM TO THE ABOVE ADDRESS.**

<b>1. REPORT DATE (DD-MM-YYYY)</b> 01-07-2010		<b>2. REPORT TYPE</b> Technical Memorandum		<b>3. DATES COVERED (From - To)</b>	
<b>4. TITLE AND SUBTITLE</b> Entry, Descent and Landing Systems Analysis Study: Phase 1 Report				<b>5a. CONTRACT NUMBER</b>	
				<b>5b. GRANT NUMBER</b>	
				<b>5c. PROGRAM ELEMENT NUMBER</b>	
<b>6. AUTHOR(S)</b> Dwyer Cianciolo, Alicia M.; Davis, Jody L.; Komar, David R.; Munk, Michelle M.; Samareh, Jamshid A.; Williams-Byrd, Julie A.; Zang, Thomas A.; Powell, Richard W.; Shidler, Jeremy D.; Stanley, Douglas O.; Wilhite, Alan W.; Kinney, David J.; McGuire, M. Kathleen; Arnold, James O.; Howard, Austin R.; Sostaric, Ronald R.; Studak, Joseph W.; Zumwalt, Carlie H.; Llana, Eduardo G.; Casoliva, Jordi; Ivanov, Mark C.; Clark, Ian; Sengupta, Anita				<b>5d. PROJECT NUMBER</b>	
				<b>5e. TASK NUMBER</b>	
				<b>5f. WORK UNIT NUMBER</b> 811450.16.08.07	
<b>7. PERFORMING ORGANIZATION NAME(S) AND ADDRESS(ES)</b> NASA Langley Research Center Hampton, VA 23681-2199				<b>8. PERFORMING ORGANIZATION REPORT NUMBER</b>  L-19869	
<b>9. SPONSORING/MONITORING AGENCY NAME(S) AND ADDRESS(ES)</b> National Aeronautics and Space Administration Washington, DC 20546-0001				<b>10. SPONSOR/MONITOR'S ACRONYM(S)</b>  NASA	
				<b>11. SPONSOR/MONITOR'S REPORT NUMBER(S)</b>  NASA/TM-2010-216720	
<b>12. DISTRIBUTION/AVAILABILITY STATEMENT</b> Unclassified - Unlimited Subject Category 66 Availability: NASA CASI (443) 757-5802					
<b>13. SUPPLEMENTARY NOTES</b>					
<b>14. ABSTRACT</b> NASA senior management commissioned the Entry, Descent and Landing Systems Analysis (EDL-SA) Study in 2008 to identify and roadmap the Entry, Descent and Landing (EDL) technology investments that the agency needed to make in order to successfully land large payloads at Mars for both robotic and human-scale missions. This paper summarizes the motivation, approach and top-level results from Year 1 of the study, which focused on landing 10-50 mt on Mars, but also included a trade study of the best advanced parachute design for increasing the landed payloads within the EDL architecture of the Mars Science Laboratory (MSL) mission.					
<b>15. SUBJECT TERMS</b> Systems analysis; Mars landing; Payloads; Parachutes; Decelerators; Entry; Descent; Landing; Aerocapture; Technology Assessment					
<b>16. SECURITY CLASSIFICATION OF:</b>			<b>17. LIMITATION OF ABSTRACT</b>	<b>18. NUMBER OF PAGES</b>	<b>19a. NAME OF RESPONSIBLE PERSON</b>
<b>a. REPORT</b>	<b>b. ABSTRACT</b>	<b>c. THIS PAGE</b>			STI Help Desk (email: help@sti.nasa.gov)
U	U	U	UU	126	<b>19b. TELEPHONE NUMBER (Include area code)</b> (443) 757-5802